Edward Jackson

Magdalen College

Supervisors

Constantin-C. Coussios and Robin O. Cleveland

Modelling and Monitoring Nonlinear Acoustic Phenomena in High-Intensity Focused Ultrasound Therapy

A thesis submitted for the degree of Doctor of Philosophy

Hilary 2015

A thesis submitted for the degree of Doctor of Philosophy

Modelling and Monitoring Nonlinear Acoustic Phenomena in HIFU Therapy

By Edward Jackson, Magdalen College
Submitted Hilary 2015

Abstract

High intensity focused ultrasound (HIFU) provides a wide range of noninvasive therapies ranging from drug delivery to the destruction of kidney stones. In particular, thermal ablation by HIFU presents an effective noninvasive method for the treatment of deep seated solid tumours. HIFU's further uptake is limited by a need for improved treatment planning and monitoring. Two nonlinear acoustic phenomena that play key roles in HIFU treatment: finite amplitude effects that lead to the generation of harmonics and steepening of wavefronts, and acoustic cavitation. The former must be taken into careful consideration for treatment planning purposes, while the latter has the potential to provide fast, real-time, cost effective treatment monitoring. The first half of this thesis provides new measurements for the nonlinear acoustic properties of tissue, assesses the validity of two common modelling techniques for simulating HIFU fields. The second half develops a new method for combining passive acoustic mapping- an ultrasound monitoring technique- with MR thermometry, to assess estimates of cavitation enhanced heating derived from passive acoustic maps.

In the first results chapter B/A was measured in ex-vivo bovine liver, over a heating/cooling cycle replicating temperatures reached during HIFU ablation, adapting a finite amplitude insertion technique (FAIS), which also allowed for measurement of sound-speed and attenuation. The method measures the nonlinear progression of a plane-wave through liver and B/A was chosen so that numerical simulations matched measured waveforms. Results showed that attenuation initially decreased with heating then increased after denaturation, sound-speed initially increased with temperature and then decreased, and B/A showed an increase with temperature but no significant post-heating change. These data disagree with other reports that show a significant change and suggest that any nonlinear enhancement

in the received ultrasound signal post-treatment is likely due to acoustic cavitation rather than changes in tissue nonlinearity.

In the second results chapter two common methods of modelling HIFU fields were compared with hydrophone measurements of nonlinear HIFU fields at a range of frequencies and pressures. The two methods used were the KZK equation and the commercial package PZFlex. The KZK equation has become the standard method for modelling focused fields, while the validity of PZFlex for modelling these types of transducers is unclear. The results show that the KZK equation is able to match hydrophone measurements, but that PZFlex underestimates the magnitude of the harmonics. Higher order harmonics in PZFlex are not the correct shape, and do not peak around the focus. PZFlex performs worse at higher pressures and frequencies, and should be used with caution.

In the final two chapters a system for estimating cavitation-enhanced heating from acoustic maps is developed and benchmarked against magnetic resonance thermometry methods. The first chapter shows that the ultrasound and MR monitoring systems are compatible, and registers the two imaging systems. The HIFU focus is clearly visible in passive maps acquired in the absence of cavitation and these coincide with the centre of heating in MR temperature images. When cavitation occurs, it coincides spatially and temporally with the appearance of a clear spike in temperature, especially when the passive maps are processed using the Robust Capon Beamformer algorithm. The final chapter shows how passive maps can be converted into thermal heating inputs, and used to estimate cavitation-enhanced temperature increases. These estimates have the potential to closely match maximum temperature rise, and estimated thermal dose after the estimated temperature rise is spatially averaged. However, the method is not always successful. This is partly due to uncertainties in MR thermometry estimates, partly due to uncertainties in the acoustic properties of tissue.

Statement of Originality

I hereby declare that this submission is my own work and, to the best of my knowledge, it contains no materials previously published or written by another person, or substantial proportions of material which have been accepted for the award of any other degree or diploma at the University of Oxford or any other educational institution, except where due acknowledgement is made in the thesis.

Any contribution made to the research by others, with whom I have worked at the University of Oxford or elsewhere, is explicitly acknowledged in the thesis.

I also declare that the intellectual content of this thesis is the product of my own work, except to the extent that assistance from others in the project's design and conception or in style, presentation and linguistic expression is acknowledged.

Edward Jackson

Hilary 2015

Acknowledgements

The work in this thesis would not have been possible without the assistance I have received from many people during my time in Oxford. I would especially like to thank my two supervisors, Constantin Coussios and Robin Cleveland. I have benefitted hugely from their experience, guidance, and enthusiasm, and am very grateful to have had them as mentors.

The BUBBL group has provided me with a friendly, supportive atmosphere to pursue my studies, and make lasting friendships. In particular, I would like to thank Shan Qiao for his help with PZlex simulations, and Carl Jensen for his previous work on PAM-based temperature estimation. Jamie Collin and Christian Coviello provided help and advice on almost any topic throughout my time in BUBBL, and Jim Fisk and David Salisbury have expertly produced many, many pieces of equipment used in this thesis. Outside BUBBL, Sean Smart and Paul Kinchesh have been invaluable in patiently sharing their knowledge of all things MRI-related. Huge thanks are owed to Joe Martin, for his help with the MR-HIFU experiments, which involved sharing many long days in the MRI bunker.

I would like to thank my grandparents, James and Frances Milford for keeping me well looked after for the final months of my thesis, and the rest of my family for their support. Lastly, I would like to thank Sarah, whose love and encouragement has made a world of difference.

I also gratefully acknowledge the generous support of the UK Engineering Physical Sciences Research Council.

Dissemination

Peer Reviewed Journal Papers E. J. Jackson, R.O. Cleveland, C.-C. Coussios, "Nonlinear Acoustic Properties of ex vivo Bovine Liver and the Effects of Temperature and Denaturation" Physics in Medicine and Biology 59.12 (2014): 3223

Conference Presentations

E. Jackson, J. Martin, P. Kinchesh, S. Smart, R.O. Cleveland, C.-C. Coussios, "Passive Acoustic Mapping and MR Thermometry for Monitoring High Intensity Focused Ultrasound" 14th International Symposium on Therapeutic Ultrasound, April 2014

E. J. Jackson, R.O. Cleveland, C.-C. Coussios, "The Origins of Nonlinear Enhancement in ex-vivo Tissue During High Intensity Focused Ultrasound Ablation" 21st International Congress on Acoustics, June 2013

CONTENTS

LIST OF FIGURES

CHAPTER 1

HIGH INTENSITY ULTRASOUND THERAPY: TREATMENT AND MONITORING

In addition to its use as a diagnostic modality, as a therapeutic tool ultrasound has a long history and an exciting future.

Therapeutic ultrasound is commonly known as 'High Intensity Focused Ultrasound', or HIFU, as the acoustic intensity required to produce a therapeutic effect is much higher than in diagnostic applications. In these treatments a focused ultrasound transducer creates a pressure wave that propagates through tissue, and at the focus of the transducer the amplitude of the pressure wave is much higher than elsewhere. Locally it is able to deliver enough energy to create a therapeutic effect at the desired treatment location leaving surrounding areas unharmed (Haar and Coussios, 2007b). Therapeutic effects can be thermal, due to energy from the acoustic wave being converted into heat through absorption, or mechanical, where energy from the pressure wave disrupts the tissue as it passes through it. The thera-

peutic effect and mechanism depends on the ultrasound parameters used, the type of transducer, and the acoustic properties of the target (Haar and Coussios, 2007b; Coussios and Roy, 2008; Bailey et al., 2003; Xu et al., 2007).

In this section the development of therapeutic ultrasound techniques is examined before looking in more detail at two important aspects of high intensity focused ultrasound (HIFU) treatment- monitoring and planning. It is shown that while there are many advantages to HIFU therapy there are still needs in these two areas.

1.1 The Beginnings of High Intensity Focused Ultrasound

The use of high intensity focused ultrasound (HIFU) as a noninvasive technique to create areas of thermal damage, or 'lesions', was first developed by Lynn et al. (1942). Their study used a voltage applied to a focused piezoelectric crystal at its resonant frequency to produce ultrasound that created 'melted defects' in paraffin blocks, areas of damage in samples of ex-vivo liver, and changes in the brains of living animals. Subsequent work by Fry et al. (1954) and Fry (1958) used multiple transducers to provide a focusing effect and was able to create localised volumes of damaged tissue in the central nervous system. This work continued for the next decade, alongside the development of ultrasound imaging techniques Erikson, Fry, and Jones (1974).

Other work used the same technique to create lesions in the retina Lizzi et al., 1978 or to destroy solid tumours (Fry and Johnson, 1978) (Burov and Andreevskaya, 1956). Frizzell et al. (1977) examined the mechanism behind the lesions created and by simulating the thermal effects during the treatment was able to show that the primary cause of damage is the temperature rise at the focus due to the absorption of

the ultrasound. Histological examination of the lesions (Chen et al., 1993) showed that the treated volume comprised a well defined volume of completely denatured tissue without damage to the surrounding area. Although very promising this technique did not immediately gain wide clinical uptake due to a lack of a method for accurately identifying the target volume (Haar and Coussios, 2007a).

With improvements in ultrasound imaging techniques further attempts were made to monitor HIFU by looking for a hyperechoic region on a B-mode ultrasound image (Haar, Sinnett, and Rivens, 1989) (Vallancien et al., 1990) (Vaezy et al., 2001a). In addition to ultrasonic methods attempts began to monitor using magnetic resonance imaging. Following on from these developments in monitoring newer clinical trials began to show promising results. Some of the first clinical trials using commercial HIFU devices were to treat prostate cancer, due to its easy ultrasonic access(Gelet et al., 1995) (Chapelon et al., 1999). These studies had satisfactory outcomes the results are comparable to what can be achieved using radiation therapy(Gelet et al., 2001).

Initially MR imaging was also used to identify the region that thermal effects occurred in and to visualise the treated volume (Cline et al., 1992). Later, the technique was extended to measure the relative temperature rise within the focal region (Hynynen et al., 1993) (Ishihara et al., 1995). Using MRI guidance, trials to create thermal lesions within uterine fibroids also showed volume reduction correlating to treatment volume and encouraging symptomatic response.

These developments in imaging technology were enough to renew interest in HIFU ablation as a clinical possibility. It has many advantages as a treatment for solid tumours (Kennedy, 2005) in that it is cheap, as well as being noninvasive and nonionising. The side effects of the treatment are much less severe than chemotherapy and in comparison to surgery the recovery time is much shorter. In contrast to

radiotherapy in particular there is no limit to the number of repeat treatments a patient can receive, nor does it preclude the use of any other treatment. In contrast to other minimally invasive techniques such as radiofrequency ablation, laser ablation or cryoablation, HIFU is the only treatment that is truly noninvasive, as all the other methods require the insertion of a probe. Probe insertion brings with it a risk of visceral or vascular puncture, tumour seeding along the needle track as well as the risk of infection. In addition, once the probe is inserted it is impossible to move the probe around the target area without reinsertion, while successive shots from an extracorporeal HIFU transducer can be combined to 'paint out' a lesion.

1.2 Acoustic Cavitation

In addition to thermal ablation, there are a number of other applications of therapeutic ultrasound. In the majority, if not all, of the applications discussed below acoustic cavitation plays a role in the efficacy of the treatment, therefore this section begins with a brief description of the phenomenon.

Acoustic cavitation has an important role to play in enhancing the rate of heating during HIFU ablation and is the driving mechanism behind many other applications of therapeutic ultrasound. Cavitation can be defined in its most general sense as 'the creation of new surfaces, and/or expansion/contraction/distortion of new ones within the body of a liquid, the process being coupled to acoustic energy' (Leighton, 1994). This therefore refers to the creation of a vapour cavity in response in response to the rarefaction phase of an acoustic pressure field, the expansion of bubbles 'seeded' by pre-existing gas pockets or cavitation nuclei in a medium. In acoustic cavitation bubbles also undergo subsequent expansion, contraction and collapse in response to compression and rarefaction phases of a sound field. While cavitation enhanced heating will be discussed in greater detail in later chapters,

here it is only necessary to mention two types of acoustically driven bubble oscillation that are commonly referred to as 'stable' and 'inertial' cavitation (Coussios and Roy, 2008). 'Stable' cavitation is the prolonged pulsation of a bubble subject to acoustic stress about its equilibrium radius, the bubble oscillates in a periodic manner, expanding and contracting depending on the instantaneous pressure of the surrounding medium. At higher pressures the cavitation becomes 'inertial'. This is when the cavity grows explosively before collapsing violently, the collapse driven by the inertia of the inrushing fluid.

The two regimes can very broadly be said to bring with them different biological effects (Coussios and Roy, 2008). 'Stable' cavitation encourages microstreaming as a circulating flow is set up around the oscillating bubble (Elder, 1959), and is one of the important effects in enhancing drug penetration. 'Inertial' cavitation readily leads to localised heating effects Holt and Roy, 2001, as the sound emitted from the rapid collapses are readily absorbed by the surrounding tissue and converted into heat, increasing the rate of energy deposition around the collapsing bubbles. In both cases, in addition to their therapeutic effect, cavitating bubbles themselves produce acoustic emissions. This is important from a monitoring point of view, as the sound from cavitating bubbles can be detected, and localised (Gyongy and Coussios, 2010), giving an indication of the spatial extent, and the magnitude of the therapeutic effect.

1.2.1 Further Applications of High Intensity Focused Ultrasound

One of the most commonly used non-ablative applications of therapeutic ultrasound is extra-corporeal shock wave lithotripsy, as a treatment for the fractionation of kidney stones. It uses high amplitude focused shock waves to fragment renal and biliary stones so they can be passed through the ureters and cystic duct (Lingeman

et al., 1986). It has been shown that acoustic cavitation is a key contributor to stone breakup, in particular the violent collapse of bubble clouds or clusters (Pishchalnikov et al., 2003; Zhu et al., 2002).

Another technique that uses the mechanical effect of cavitating bubbles is histotripsy, in which nonthermal mechanical effects of ultrasound (cavitation) can be used to progressively homogenize tissue (Roberts et al., 2006) as an alternative to thermal ablation. The bubbles can be created either by applying short pulses at high intensities to produce cavitation, or slightly longer millisecond pulses that boil the tissue. In both cases, bubbles are produced that undergo large changes in radii and create lesions that show no sign of thermal damage (Kreider et al., 2011). Focal pressures for histotripsy are much higher than for HIFU, using above 10 MPa peak negative focal pressure, and over 40 MPa peak positive pressure (Maxwell et al., 2012).

Therapeutic ultrasound is also able to enable targeted drug delivery and localised enhancement of drug activity (Coussios and Roy, 2008). This can be achieved through a variety of means, exploiting mechanical and thermal effects. Thermally, a localised temperature rise is generated through the same mechanisms as for thermal ablation, although lower input powers reduce the final temperature rise to 5-10 °C. This can then be used to release anti-cancer drugs encapsulated inside thermally sensitive lipid or polymer spheres to enable highly localised release of chemotherapeutic drugs (Mylonopoulou et al., 2010; Dromi et al., 2007; Grüll and Langereis, 2012).

Localised drug delivery can also be achieved through non thermal methods, by using the mechanical aspect of ultrasound to disrupt ultrasound contrast agents that carry a drug payload. In addition to carrying the drug payload the bubbles can also be modified to target specific sites within the body, such as tumours (Fer-

rara, Pollard, and Borden, 2007; Klibanov, 2006). This effect has been used to deliver not only drugs but also other therapies, such as oncolytic viruses (Carlisle et al., 2013; Bazan-Peregrino et al., 2013), and has been shown to work by enhancing extravasation, increasing the transport of drugs through leaky vasculature in tumours. Ultrasound also increases the permeability of skin, increasing the penetration of drugs passing through the stratum corneum (Lavon and Kost, 2004; Mitragotri, Blankschtein, and Langer, 1995). This is another application where increasing the amount of inertial cavitation has been shown to enhance delivery (Bhatnagar, Schiffter, and Coussios, 2014).

Ultrasound has also been shown to enhance thrombolysis in the treatment of strokes (Medel et al., 2009) when combined with thrombolytic drugs. The enhancement has been shown to only occur in the presence of cavitation (Datta et al., 2006) and suggests that stable bubble oscillations around the clot play a key role in its destruction.

Finally, ultrasound has been shown to be able to reversibly open the blood-brain barrier that allows for the otherwise problematic delivery of therapeutic agents to treat diseases of the central nervous system (Hynynen et al., 2005). Again, analysis of the mechanism behind the opening suggests that the interaction of bubbles and ultrasound, possibly stable cavitation, is one of the key contributors to effective treatment (McDannold, Vykhodtseva, and Hynynen, 2006).

While the current work is mostly concerned with HIFU ablation, the effects of cavitation must still be taken into account, as cavitation-enhanced heating plays an important role in providing effective heating that can be readily monitored. Additionally, the number, variety and effectiveness of the varied treatment regimes identified above show that cavitation-driven non-thermal treatments make up a significant proportion of therapeutic ultrasound applications.

1.3 Treatment Monitoring and Assessment of HIFU Ablation

As one of the main advantages of HIFU therapy is its noninvasiveness, by its very nature this makes monitoring and assessment a challenge. There are a number of competing methods for HIFU monitoring and assessment, which can be broadly split into ultrasound-based methods, and magnetic resonance imaging methods. While MRI methods have become the 'gold standard' for monitoring HIFU treatment ultrasound methods are able to compete on grounds of superior frame rate, portability, and cost (Rivens et al., 2007). In cases where the imaging is able to monitor temperature rise during treatment a method is required to relate temperature rise to treatment outcomes. This is the thermal dose and is discussed in the final section of the chapter.

1.3.1 Ultrasound Methods

1.3.1.1 B-mode monitoring

Ultrasound imaging seems the natural accompaniment to ultrasound surgery. Ultrasound imaging transducers can be placed confocally inside therapy transducers, or therapy and imaging can be performed with the same device (Rivens et al., 2007).

Early HIFU monitoring depended on standard B-mode ultrasound monitoring. In this technique a linear array of transducers send out short ultrasonic pulses and build up an image based on the relative magnitudes and return times of echoes generated by changes in density and compressibility of the medium. In B-mode monitoring successful treatment is monitored by looking for a hyperechoic 'bright spot' that appears at the HIFU focus and corresponds with the subsequent appearance of a lesion (Vaezy et al., 2001b; Haar, Sinnett, and Rivens, 1989; Wu et al., 2003). The

bright spot is brought about either by a cloud of bubbles generated through cavitation or more likely by much larger bubbles caused by boiling the tissue (Rabkin et al., 2006; Rabkin, Zderic, and Vaezy, 2005) and does not coincide with the appearance of the lesion. Indeed it is entirely possible to create lesions without the appearance of cavitation activity (Nandlall, Jackson, and Coussios, 2011). This suggests that by the time boiling temperatures have been reached in tissue this is past the point of thermal denaturation (Coussios et al., 2007) and a lesion is likely to have formed before hyperecho is observed. Hyperecho is unsuitable for post-treatment assessment as bubbles decay with time.The presence of a large cloud of hyperechoic bubbles leads to distortion of the lesion and unpredictable lesion growth towards the transducer (Bailey et al., 2001). Therefore B-mode is unsuitable for lesion monitoring.

1.3.1.2 Ultrasound Elastography

Ultrasound elastography is able to provide qualitative images of strain and elastic modulus distributions in soft tissues. By externally compressing the tissue and taking the cross correlation of a-line pairs in pre- and post- compression images the strain profile along the transducer axis is calculated. An image of the elastic modulus can be created by measuring the stress applied by the compressing transducer and correcting for a nonuniform stress field (Ophir et al., 1991). However, as this correction requires knowledge of the 3D components of stress and strain in the tissue, this problem is ill-posed (Bamber et al., 1999). Solving it either requires techniques that converge on the most likely stress/strain distribution (Bamber et al., 1999), or assumptions about the nature of the stress field (Skovoroda, Emelianov, and o'Donnell, 1995).

As tissue is heated its proteins begin to lose their structure and become initially less stiff, but as the protein changes become irreversible stiffness increases(Wu et

al., 2001), and elastographic techniques have been used to determine the sizes of lesions (Kallel et al., 1999; Righetti et al., 1999; Shi et al., 1999). Elastograms in human trials are able to outperform B-mode imaging, as the B-mode bright spot decayed after treatment, and elastograms correlated much better with the extent of the lesion observed on MR images (Souchon et al., 2003). However, there are problems associated with poor signal-to-noise ratio (SNR) and patient motion making cross-correlation difficult, and performance decreases with depth, and in general elastograms underestimate lesion volume compared to MRI images of lesions (Curiel et al., 2005). As speed of sound also changes with temperature, and tissue expands thermally, this creates the illusion of displacement, and means that elastograms cannot be taken during treatment itself while the temperature is changing, only during pauses once the tissue has cooled (Curiel et al., 2005; Souchon et al., 2003). The presence of cavitation is also not necessarily compatible with elastography. While it is able to enhance image contrast and SNR, cavitating bubbles also shield the lesion, with pre-focal bubbles making the lesion location itself hypoechoic, reducing SNR (Curiel et al., 2005), while in another study it creates artefacts on the elastograms(Thittai, Galaz, and Ophir, 2011).

It is possible that rather than externally compressing the region of interest tissue can be compressed by the force ultrasound exerts, known as the acoustic radiation force, and this method of imaging has had some success in observing lesions (Azuma et al., 2005; Fahey et al., 2004). An alternative similar technique is now emerging known as harmonic motion imaging (HMI) (Maleke and Konofagou, 2010).This technique uses HIFU to deliver the radiation force, and amplitude-modulates the HIFU signal with a low frequency carrier to create sinusoidal positive displacement. This has been shown to be able to detect HIFU lesions, and is well suited to real time monitoring, as the therapeutic acoustic signal can be easily mod-

ulated to provide displacement (Hou et al., 2011; Curiel and Hynynen, 2011). However, while stiffness increases, many other properties of tissue change at the same time that work to counteract the decrease in movement associated with a stiffer lesion, most notably the increase in attenuation described in chapter 2, which increases the acoustic radiation force. In addition, changes in the speed of sound and thermal expansion create artificial displacements, while the increased attenuation of the tissue will increase the displacement due to an increased acoustic radiation force. The increase in attenuation will partly depend on the state of the lesion, and partly on the presence of cavitation. Due to the many conflicting factors, it has been shown that HMI is not always a robust detector of lesion formation (Draudt, 2012).

1.3.1.3 Monitoring Changes in Acoustic Properties

As described in chapter 2 many acoustic properties of tissue are known to change during thermal denaturation. The most dramatic of these is the attenuation coefficient, which roughly doubles after tissue has been denatured. It is possible to detect lesions by calculating the attenuation coefficient and its frequency dependence from the frequency spectrum of a reflected imaging pulse by looking at the reduction in the signal after treatment and accounting for the distance travelled through tissue (Rahimian and Tavakkoli, 2013; Ribault et al., 1998; Zhang et al., 2009). In these papers some of the detected change in attenuation post-treatment is due to the change in tissue properties, but a large proportion of this change is due to transient cavitation effects. This is true of a number of studies analysing backscattered signals to detect lesions, (Anand, 2004; Kumon et al., 2012; Kemmerer and Oelze, 2012; Silverman et al., 2006) where changes in the backscattered ultrasound images are observed and quantified, but it is unclear to what extent the changes are attributable to cavitation or a change in the acoustic properties of the medium.

1.3.1.4 Ultrasound Thermometry

It is possible to use ultrasound to measure the temperature of heated tissue. The most common technique is to exploit the temperature dependance of sound speed, and thermal expansion to track changes in the distance between scatterers (Seip et al., 1996; Simon, VanBaren, and Ebbini, 1998). The sound speed of most tissue initially increases with temperature, as temperature passes 50-60 °C the speed of sound decreases (Techavipoo et al., 2012). In addition to sound speed, the coefficient of thermal expansion for the tissue must also be measured (Arthur et al., 2005), both of these parameters vary from tissue to tissue. Other methods use reflection techniques to measure either the attenuation and nonlinearity coefficients of tissue. These methods require knowledge of the relationship between temperature and the properties under observation, which are not always available for all tissue types, and are rarely available for tissues that have undergone thermal denaturation. SNR is also an issue, as the size of the lesion is often small compared to the total acoustic path.

1.3.1.5 Reflex Transmission Imaging

Reflex transmission imaging has been used for monitoring lesion formation and temperature rise. It works by insonating a region of interest with a focused source, and uses scatterers beyond the region of interest to provide reflected acoustic energy. The reflected sound is then amplified and integrated to provide a pixel value, and an image is built up of a raster scan of pixels (Green and Arditi, 1985; Green, Ostrem, and Whitehurst, 1991). The value of this pixel depends mostly on attenuation (Green, Ostrem, and Whitehurst, 1991) and has been used to provide intensity based images of thermal lesions (King et al., 2003). The main difference between this imaging technique and B-mode imaging is that in RTI, pre-focal signals are ig-

nored, and signals behind the focus are amplified and integrated to provide a pixel at a particular location at the focal distance (Green and Arditi, 1985). This technique has also been used to determine temperature rise by taking the relative phase of ultrasound images and relating them to temperature (Farny and Clement, 2008). The source of the backscattered ultrasound and the detector may be the same transducer or separate transducers.

1.3.1.6 Passive Acoustic Mapping

The majority of the above monitoring techniques are either unsuitable for real-time monitoring or are compromised in the presence of cavitation. In therapies where cavitation is the main contributing factor to treatment outcome it is advantageous to monitor the cavitation emissions themselves, using the acoustic emissions of the bubbles to help, rather than hinder monitoring. An emerging technique to map the location and activity of bubbles during HIFU treatment is called passive acoustic mapping. In this modality an array of transducers passively receives acoustic emissions from cavitating bubbles and through delay and sum beamforming creates real-time spatial maps of cavitation activity. These maps can be analysed in the frequency domain to determine the type of bubble activity (Gyongy and Coussios, 2010; Jensen et al., 2012; Arvanitis and McDannold, 2011). Maps of this kind have been shown to correlate well with the extent of lesion formation even when no cavitation is visible on a conventional B-mode image (Jensen et al., 2012), has been used to estimate the amount of cavitation enhanced heating in ablation experiments (Jensen, Cleveland, and Coussios, 2013), monitor cavitation intracranially (Jones, O'Reilly, and Hynynen, 2013), and has also shown promise as a tool to monitor drug release (Mylonopoulou et al., 2010).

1.3.2 MRI Treatment Monitoring

The other noninvasive, non-ionising imaging modality that is particularly well suited to monitoring temperature in HIFU treatments is magnetic resonance imaging (MRI). There are two main ways MRI is used in thermal treatments in particular, for treatment monitoring and assessment, through its ability to monitor temperature in real time, and visualise thermal lesions. Here a brief overview of the techniques and capabilities is provided, and shows that cost concerns aside, MR guided HIFU is considered the 'gold standard' for HIFU monitoring (Rivens et al., 2007). A more detailed overview of the physics of the MRI techniques used in this study is described in chapter 4

1.3.2.1 MR Thermometry

There are many MRI sensitive parameters that vary with temperature that have been used for thermometry, namely the T1 and T2 decay times and the diffusion coefficient. However, they all suffer from one or more drawbacks that have limited their widespread uptake. The dependence of T1 and T2 relaxation times on temperature differ between tissue types, are only linear within a small temperature range, and change depending on whether the tissue has been treated or not. Scan times to measure these parameters accurately are on the order of minutes, and therefore slower than HIFU treatments where temperatures can rise by tens of degrees in seconds.The diffusion coefficient is very sensitive to changes in temperature, but again depends on whether the tissue has been treated or untreated, and requires tissue to be completely isotropic. Again, scan times to measure diffusion are very long (Quesson, Zwart, and Moonen, 2000; Rieke and Butts Pauly, 2008).

The method that has become much more widely used is the proton resonance frequency shift (PRF) method (Quesson, Zwart, and Moonen, 2000; Rieke and Butts

Pauly, 2008). The change in PRF occurs because as temperature increases the bonds between hydrogen oxygen atoms in water molecules become more stretched. This reduces the degree of association of the water molecules and increases the degree of electron shielding of the protons. This change in shielding creates a inhomogeneity in the magnetic field, and it was shown by Sekihara, Matsui, and Kohno (1985) that inhomogeneities in a static magnetic field can be visualised in the phase component of MR images.

Ishihara et al. (1995), De Poorter (1995a), and De Poorter (1995b) used these phase maps to visualise temperature fields. In comparison to the other methods the proton resonance frequency (PRF) changes linearly with temperature and remains linear for a large enough temperature range to cover HIFU treatment. It remains constant for treated and untreated tissue and is similar for different types of non-fatty tissue (Quesson, Zwart, and Moonen, 2000). This technique gives a simple formula for calculating the relative temperature rise in the medium after subtracting a reference unheated phase image from the phase image of the treated tissue:

$$\Delta T = \frac{\Phi(T) - \Phi(T_{ref})}{\alpha \gamma TE B_0} \tag{1.1}$$

Where T is temperature, $\Phi(T)$ and $\Phi(T_{ref})$ are the phase of the temperature image and the reference image. B_0 is the magnetic field strength, $TEistheechotime$, γ is the gyromagnetic ratio α is the temperature-dependent proton resonant frequency change coefficient. This technique is commonly capable of measuring temperature to within 1°C, with a 2mm voxel size, and 1Hz temporal resolution (Quesson, Zwart, and Moonen, 2000). Better temporal and spatial resolution is available at higher field strengths, and spatial resolution can be improved at the expense of temporal resolution, and vice versa. Even at these resolutions for HIFU treatments

at high power this monitoring method will suffer from averaging effects, as high frequency ultrasound fields and cavitation events vary on length scales smaller than a millimetre, and high temperatures can be reached in fractions of seconds (Canney et al., 2010). Thermometry is often performed in orthogonal 2-D planes centred at the HIFU focus which increases the available frame rate, but must assume that heating is radially symmetric.

1.3.2.2 MR Treatment Assessment

In addition to being used to measure temperature MR images can also be used to visualise lesions directly. The fact that the T1 and T2 relaxation times are susceptible to changes in the state of necrosed tissue means that images weighted towards either relaxation time can be used to visualise lesions. This assessment can only be performed once tissue has cooled, and may take a few minutes to appear on an MR image (Graham, Bronskill, and Henkelman, 1998).

The T2 time constant increases with temperature, and the T1 constant initially increases for tissue heated at temperature up to 70 °C before decreasing (Graham, Bronskill, and Henkelman, 1998). A typical T1 weighted image of a lesion shows a hyperintense outer region with a hypointense core (Graham et al., 1999b) or a bright core with a heterogeneous centre in T2 weighted imaging (Graham, Bronskill, and Henkelman, 1998; Rouvière et al., 2001). As cells are exposed to heat their structure and extracellular matrix change (Wu et al., 2001). This causes tissue to stiffen, whiten and changes the way water is stored in the tissue (Graham, Bronskill, and Henkelman, 1998). The latter causes the change in MR images, as water compartments are created and fluid is liberated from cells. MR images are also affected by coagulated blood and water in denatured tissue having greater access to paramagnetic centres in the blood (Graham, Bronskill, and Henkelman, 1998).

The changes in MR images have been shown to have excellent agreement with histological examination (Rowland et al., 1997; Hynynen et al., 1994; Chen et al., 1999) to such an extent that MR images themselves have been used to correlate treatment predictions from different thermal damage models with volumes of damaged tissue (McDannold et al., 2000).

1.3.3 Thermometry and Thermal Dose

Temperature measurement, especially MR thermometry is one of the most widely used ways of monitoring HIFU ablation. However, it is still necessary to relate temperature to tissue damage. One model that has gained widespread acceptance is the 'Cumulative Equivalent Minutes at 43°C' (CEM43) model developed by Sapareto and Dewey (1984) and this is the model used in most dose calculations (Rivens et al., 2007). The model assumption that tissue maintained at 43°C for 240 minutes fully denatures. As temperature increases the required treatment time reduces by half for every 1°C temperature increase.

The model uses the following formula to calculate equivalent minutes Dewhirst et al. (2003).

$$CEM_{43} = \int R^{43-T(t)} dt \tag{1.2}$$

In this formula T is temperature in °C, t is time, and R is a temperature dependent parameter, 0.25 below 43°C and 0.5 above. There are then a certain number of equivalent minutes required to denature tissue,depending on the tissue type (Damianou, Hynynen, and Fan, 1995), although across various tissue types 240 equivalent minutes has been shown to be a conservative estimate for complete thermal coagulation (McDannold et al., 2000).

While this model has gained wide acceptance it is not tissue dependent and is based on empirical measurements around 43°C Dewhirst et al. (2003). During HIFU, temperatures can reach almost 100 °C, for which the present model has not been formally validated. It has been shown to not always predict lesions, as for example investigations linking changes in the optical properties of tissue to temperature have found it necessary to vary the constants used in the thermal dose (Adams et al., 2014). Other thermal models have been developed such as those by Feng, Oden, and Rylander (2008), O'Neill et al. (2011) and Breen et al. (2007). Each is based on a slightly different set of assumptions and have been empirically validated using different methods. As a result all predict very different treatment times for the same temperature rises, and work is ongoing to determine which, if any, of these gives the result that best matches histological observations.

1.4 Treatment Planning in HIFU

Treatment planning is just as important as treatment monitoring in ensuring that HIFU treatment is effective and fast. For thermal treatments in particular this involves being able to choose an ultrasound input that will create a lesion of the correct size, in the correct location. Early attempts to find thresholds for lesion damage used empirical data to create graphs of acoustic intensity versus time, and from this were able to derive formulae for damage thresholds of the form

$$I\sqrt{t} = C \tag{1.3}$$

where I is acoustic intensity, based on the power output of the device, t is time, and C is an empirically derived constant (Frizzell et al., 1977; Frizzell, 1988; Fry et al., 1970). These studies showed that there was similarity for the same tissues between

different mammalian species, and gave thresholds that were either frequency independent or only weakly dependent on frequency. This is because although acoustic absorption increases with frequency, diffusion also increases due to the smaller size of the focus (Carstensen et al., 1981). However, even though these studies find a single formula for lesion formation, they do identify different lesioning mechanisms, with cavitation effects causing lesions to be formed within very short times if the intensity is high enough (>2500 W/cm^2), and the heat sink effect of perfusion increasing the intensity required to cause a lesion for heating times above 10s (Frizzell, 1988). However, as temperature correlates with lesioning better than intensity (McDannold et al., 2000) it is better to use the in situ acoustic intensity to predict temperature rise, and then to use a thermal model to predict lesioning (Coussios and Roy, 2008; Haar and Coussios, 2007b).

The equation for predicting temperature rise is the Pennes (1948) bioheat equation,

$$\rho_t C_t \frac{\partial T}{\partial t} = k_t \nabla^2 T - w_b C_b (T - T_b) + Q_m + Q_{ac} \tag{1.4}$$

where ρ_t is the density of tissue, C_t and C_m are the specific heat capacities of tissue and blood respectively, T and T_b are the temperatures of tissue and blood, k_t is the tissue thermal conductivity. w_b is the perfusion flow rate, and Q_m and Q_{ac} are the metabolic heating rate and rate of heat deposition by ultrasound.

In simple treatment planning models a linear model is used to calculate the intensity profile of a HIFU field (Robinson and Lele, 1972; Hill et al., 1994; Wu and Du, 1990). The intensity field is then related to the rate of heat deposition by the acoustic absorption coefficient by the following equation where I is the spatially varying ultrasound intensity which is proportional to pressure squared, and α_{abs} is

and the coefficient of absorption. This is usually taken to be a fraction of the total attenuation coefficient α.

$$Q_{ac} = 2\alpha_{abs} I \tag{1.5}$$

(Nyborg, 1981). This relationship holds true at relatively low intensities in plane wave conditions, but as intensity increases the apparent absorption coefficient begins to increase with intensity (Carstensen et al., 1981; Dalecki et al., 1991). The reason for this is what is known as a finite-amplitude or nonlinear effect.

The finite amplitude effects in ultrasound are discussed in more detail in chapter 2 but are described briefly here. In linear acoustics the phase speed of a wave is assumed to be equal to the speed of sound, which is a constant c_0. In fact, the phase speed varies at different points along the wave. the phase speed is highest in high-density compressions and lowest in low-density rarefactions (Duck, 2002). This is due to the fact that any point in the wave is travelling at the speed of sound in the medium plus the particle velocity of that point in the wave, and that speed of sound itself increases with pressure. The net effect of this is that points of high pressure travel faster and low pressure travel slightly slower, distorting the wave and eventually resulting in shocks. In the frequency domain this distortion manifests itself in the generation of harmonics of the input signal.

This has two important effects on the rate of heating. Firstly, the higher harmonics are more readily absorbed by the tissue as absorption increases with frequency increasing the heating rate, and the interaction of nonlinear effects and diffraction effects cause the location of the highest heating rate to move towards the transducer (Bailey et al., 2003; Meaney, Cahill, and Haar, 2000). As HIFU treatment, by its very nature, involves high intensities, these finite amplitude effects must be taken into

account when considering lesion formation (Khokhlova et al., 2006)

One way to take this into consideration is to simulate the full nonlinear field, and then sum the heating contribution of every harmonic in the wave (Meaney, Cahill, and Haar, 2000; Khokhlova et al., 2006).

$$Q_{ac} = 2 \sum_{n=1}^{\infty} \alpha(n f_0) I_n(x, y, z) \tag{1.6}$$

There are a number of equations that can be used to calculate the focused nonlinear acoustic fields, or there are hydrophones capable of measuring fields at nonlinear pressures (Haller et al., 2012). One commonly used equation is the KZK equation (Bailey et al., 2001; Canney et al., 2010; Khokhlova et al., 2006; Meaney, Cahill, and Haar, 2000; Curra et al., 2000), which is itself a simplified version of the more computationally intensive Westervelt equation (Jing, Shen, and Clement, 2011). Another commonly used commercial program is known as PZFlex (Wojcik et al., 1995; Wojcik et al., 1993; Wojcik et al., 1998; Wojcik et al., 1999). Both of these methods are investigated in chapter 3

If acoustic cavitation is enhancing the heating then extra heating terms can be added to the equation to take account of this (Coussios and Roy, 2008). These terms take account of viscous absorption at the bubble wall and absorption of acoustic emissions from oscillating bubbles. However, to use these equations to predict temperature rise it is necessary to know in advance the size, and number of bubbles in the acoustic field. Both of these properties are unknown in advance as cavitation is a stochastic phenomenon, and bubble size can change from one acoustic cycle to the next (Coussios and Roy, 2008). This makes pre-treatment prediction of cavitation enhanced heating difficult, although it does allow the magnitude of heating to be estimated. In practice, acoustic emissions recorded during HIFU exposure

can be calibrated and converted into heating terms, Farny, Holt, and Roy, 2010; Jensen, Cleveland, and Coussios, 2013, but this then becomes more of a monitoring than a planning technique. Another method of incorporating cavitation enhanced heating is to determine a temperature-based cavitation threshold and wherever a thermal model passes the threshold, redistribute all of the energy that would have been deposited behind the point of cavitation inception in a small spherical volume (Meaney, Cahill, and Haar, 2000).

1.5 Contributions of the Current Work

This thesis addresses problems in planning and monitoring HIFU treatments concerned with two important nonlinear phenomena: distortions of the HIFU field at high intensities due to finite amplitude effects, and cavitation.

In chapter 2 the variation of the nonlinear parameter B/A is measured as tissue is heated and cooled to assess how B/A varies with temperature and denaturation. This is relevant to both treatment planning and monitoring. From a treatment planning point of view, nonlinearity needs to be captured as high amplitudes are employed so acoustic fields and thermal heating are sensitive to changes in B/A. From a monitoring perspective, B/A could be used to detect lesions using nonlinear US imaging techniques if it undergoes a large enough change during the ablation process.

Chapter 3 compares two methods of simulating focused nonlinear US fields- the KZK equation and PZFlex. These two methods are also compared against hydrophone measurements at mild nonlinear pressures. All three methods have their uncertainties- the assumptions made in formulating the KZK equation, the discrepancies and artefacts that occur when comparing different hydrophones, and the

lack of documentation and benchmarking for PZFlex. This chapter compares the two simulation methods, assesses how they differ, to what extent, and how this affects treatment planning outcomes.

While MR thermometry is the gold standard for HIFU imaging, its 1Hz frame rate and resolution in the order of mm makes it a poor method for monitoring cavitation events that give information about the non-thermal, mechanical effects in drug delivery applications. Monitoring cavitation events in thermal applications, where measuring the bubble activity tracks sources of heating rather than temperature rise, gives early information about temperature rises before they are measured by MRI. The design of a combined system to monitor HIFU treatments is described in chapter 4. In chapter 5 the suitability of using passively acquired maps of cavitation activity to estimate temperature rise is assessed, by comparing temperature estimates from PAM with temperature maps recorded using MR thermometry.

Overall, the aim of this thesis is to examine these two nonlinear phenomena in order to improve HIFU treatment monitoring and modelling.

CHAPTER 2

NONLINEAR ACOUSTIC PROPERTIES OF EX VIVO BOVINE LIVER AND THE EFFECTS OF TEMPERATURE AND DENATURATION

2.1 INTRODUCTION

In this chapter the nonlinear effects of high amplitude pressure waves are introduced and discussed in the context of their effect on HIFU acoustic fields and heating rates. Due to the high pressure amplitudes involved nonlinear acoustic effects must be understood and the relevant medium property is the parameter of nonlinearity B/A. Here B/A was measured in ex-vivo bovine liver, over a heating/-cooling cycle replicating temperatures reached during HIFU ablation, adapting a finite amplitude insertion technique (FAIS), which also allowed for measurement of sound-speed and attenuation. The method measures the nonlinear progression of a plane wave through liver and B/A was chosen so that numerical simula-

tions matched measured waveforms. To create plane-wave conditions, sinusoidal tone bursts were transmitted by a 100mm-diameter 1.125MHz unfocused transducer and measured using a 15mm-diameter 2.25MHz broadband transducer in the near field. Attenuation and sound-speed were calculated using a reflected pulse from the smaller transducer using the larger transducer as reflecting interface. Results showed that attenuation initially decreased with heating then increased after denaturation, sound speed initially increased with temperature and then decreased, and B/A showed an increase with temperature but no significant post-heating change. The B/A data disagree with other reports that show a significant change post-treatment and the measurements here suggest that any nonlinear enhancement in the received ultrasound signal post-treatment is likely due to acoustic cavitation rather than changes in tissue nonlinearity.

2.1.1 Nonlinear Plane Waves and B/A

Acoustic waves are modelled by describing the progression of small-amplitude perturbations in pressure, velocity or density to an ambient state. For example, in the case of pressure, $p = p_0 + p'$, where p_0 is the ambient value and p' is the acoustic contribution. It is derived by combining equations of conservation of mass and momentum, and an equation of state that relates pressure to density. In this case the equation of state is the Taylor series expansion of $P = P(\rho, s)$ along the isentrope s_0 where the partial derivatives are all evaluated at their unperturbed state.(Beyer, Hamilton, and Blackstock, 1998a).

$$p' = \left(\frac{\partial p}{\partial \rho}\right)_{s,0} \rho' + \frac{1}{2}\left(\frac{\partial^2 p}{\partial \rho^2}\right)_{s,0} \rho'^2 + \ldots \tag{2.1}$$

This can be also be expressed in the form

$$p' = A\left(\frac{\rho'}{\rho_0}\right) + \frac{B}{2!}\left(\frac{\rho'}{\rho_0}\right)^2 + \ldots \tag{2.2}$$

The linear approximation neglects any terms of order ρ'^2 or higher (Pierce, 1989a). The fluid mechanics equations can then be reduced to a one-dimensional wave equation:

$$\frac{\partial^2 p'}{\partial x^2} - \frac{1}{c_0^2}\frac{\partial^2 p'}{\partial t^2} = 0 \tag{2.3}$$

For a forward travelling wave this equation has solutions of the form

$$p' = f(x - c_0 t) \tag{2.4}$$

where c_0 is the small signal wave speed

$$c_0^2 = \left(\frac{\partial p}{\partial \rho}\right)_{s,0} \tag{2.5}$$

At higher acoustic pressures these second order terms become non-negligible, and the equations can be reformulated omitting third-order or higher terms. The effects of the second order terms are called nonlinear, or finite-amplitude effects, and these waves have some different behaviour to linear waves. For example, the solution to a lossless forward travelling plane wave takes the form of the implicit equation

$$p' = f(x - (v + c)t) \tag{2.6}$$

where both the particle velocity, v, and the speed of sound, c are functions of pressure. Keeping only second order terms leads to solutions of the form

$$v + c \approx c_0 + \beta v \tag{2.7}$$

$$v = \frac{\rho'}{\rho_0} c_0 \tag{2.8}$$

$$\beta = 1 + \frac{1}{2}\frac{B}{A} \tag{2.9}$$

where B/A is the ratio of the coefficients of the quadratic and linear terms in the Taylor series expansion of the relationship between pressure and density in equation 2.2 (Pierce, 1989b).

The physical interpretation of this result is that any point on the wave travels at a particular velocity that depends on the pressure at that point, and that this velocity increases with pressure. The pressure dependent change in speed is described by the β, referred to as the coefficient of nonlinearity, which has two contributions. The first is a convective contribution due to the speed of the particle in the wave itself, the second is due to the nonlinear relationship between pressure and density in the medium that depends on the acoustic medium. The parameter B/A is therefore the medium-dependent acoustic property that contributes to the rate that nonlinear effects develop.

As compressional parts of the wave travel faster, and rarefactional parts travel slower, the wave steepens as it progresses. This causes an initially sinusoidal wave to steepen, and in the frequency domain, causes harmonics to develop. In the lossless case described above the harmonics develop with distance according to Bessel functions. However, beyond a certain distance known as the shock formation distance the solution become multivalued, and physically unrealistic as shown in figure2.1 (a). The dimensionless distance $\sigma = \frac{x}{\bar{x}}$ is used to gauge the level of nonlinear distortion where $\bar{x}$ is given by

$$\bar{x} = \frac{\rho_0 c_0^3}{\beta p_0 \omega_0} \tag{2.10}$$

It shows that waves become nonlinear in shorter distances with increasing β, frequency ω_0, or initial pressure p_0. For a pure sinusoid, shocks form at the value $\sigma = 1$ (Blackstock, 1998) .

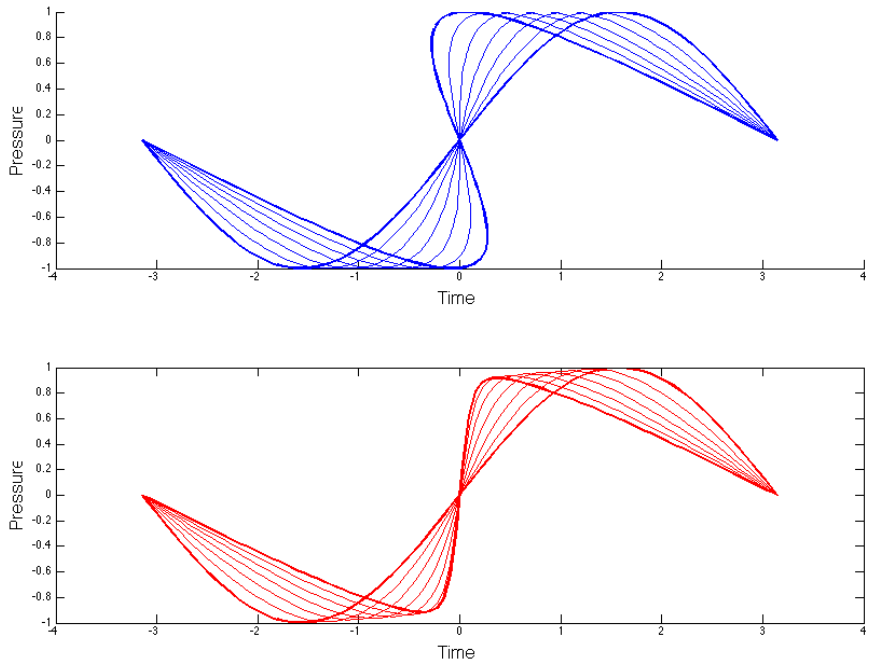

Figure 2.1: The two graphs both show an initially sinusoidal wave steepening due to nonlinear propagation. The upper figure shows the wave steepening according to the lossless Poisson solution, which beyond the shock formation distance become multi-valued. The lower figure shows the same solution for the Burgers solution, which incorporates attenuation. In this case the solution stays single valued.

A more realistic solution is the Burgers equation, which remains single valued and incorporates attenuation (Hamilton, L., and Blackstock, 1998a). The Burgers equation is

$$\frac{\partial p}{\partial x} - \frac{\delta}{2c_0^3}\frac{\partial^2 p}{\partial \tau^2} = \frac{\beta}{2\rho_0 c_0^3}\frac{\partial p^2}{\partial \tau} \tag{2.11}$$

where δ is sound diffusivity and is related to the viscosity and thermal conduction in the fluid, and τ is retarded time $(t - x/c_0)$. Figure 2.1 (b) shows how an initially sinusoidal waveform propagates when modelled by the Burgers equation, where the nonphysical multivalued pressure does not occur due to attenuation.

2.1.2 Effects of Nonlinear Propagation in HIFU Therapy

There are three main ways in which nonlinear propagation effects that can impact HIFU therapy; changing the shape of the focus, changing the rate of heating, and changing the ratio of positive to negative pressure. The impact of each of these will be discussed in turn.

In focused fields nonlinearity changes the shape of the focus. One way of interpreting this is that due to nonlinear effects energy has taken out of the field at the fundamental frequency and is converted into energy at a higher frequency. The higher frequency fields have higher gains, and so for the same transducer geometry they have smaller, tighter focii. The intensity in the focal region is therefore increased with a corresponding decrease elsewhere.

In examples by Khokhlova et al. (2006), Bailey et al. (2003), and Filonenko and Khokhlova (2001) nonlinear models predict increases in intensity of around 15-20% higher than equivalent linear models for intensities between 1500 and 6000 W/cm^2 at HIFU frequencies between 1.7 and 3.5MHz and predicted linear pressure amplitudes of 10-12MPa. The extra intensity only occurs around the focus, making the shape of the beam narrower.

The second effect is the increase in the rate of heat deposition due to nonlinear

distortion. The rate of heat deposition Q by a nonlinear wave can be written

$$Q = 4 \sum_{n=0}^{\infty} \alpha_n |C_n|^2 / c_0 \rho_0 \tag{2.12}$$

where C_n is the peak to peak amplitude of the nth harmonic and α_n is the absorption at that frequency. In most tissues absorption increases with frequency roughly linearly, and therefore the transfer of energy from the fundamental to the higher harmonics by nonlinearity will lead to greater absorption and therefore greater heating rates.

For the same three studies mentioned above the predicted rate of heating increases by a factor of 4-10 when nonlinearity is taken into account. At higher instantaneous intensities of around 16000W/cm^2 the increase is of a factor of 100 (Canney et al., 2010). Pinton et al. (2011) modelled transcranial HIFU heating, and predicts that even at lower pressures of 4MPa at 1MHz the received thermal dose becomes an order of magnitude larger when nonlinearity is taken into account. In temperature rise calculations for heating liver taking nonlinear heating into account doubles the dimensions of heated volumes that exceed a 75 °C temperature rise (Filonenko and Khokhlova, 2001; Bailey et al., 2003).

One way to show the effects of nonlinear heating experimentally is to employ tone bursts where the burst length and pressure amplitude are controlled so that the time average intensity is the same in each case, and according to linear theory the rate of heating should also be the identical. Hynynen (1987) shows that measured temperature rises increase at the focus as nonlinear effects were enhanced, while post-focally they reduce. In Khokhlova et al. (2006) and Bailey et al. (2003) enhanced heating leads to larger lesions in a gel phantom at the higher pressure, while in Canney et al. (2010) nonlinear heating causes visible millisecond boiling.

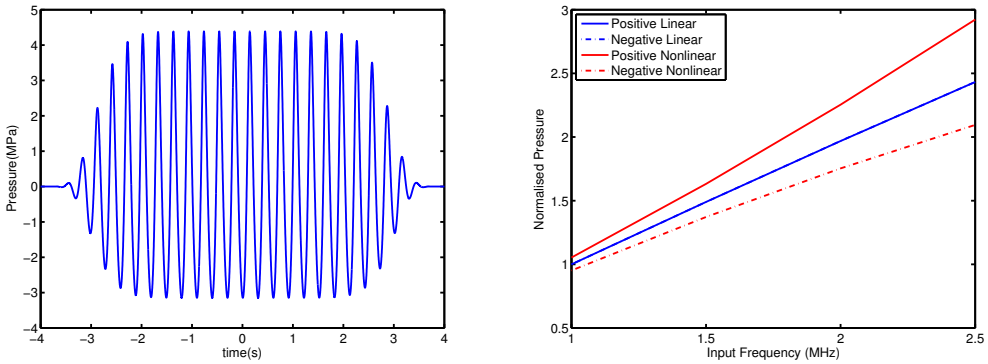

(a) (b)

Figure 2.2: (a) shows the simulated pressure waveform at the focus of a 3MHz HIFU transducer with a focal length of 62.6mm, aperture radius of 31mm and a central hole of 10mm diameter, driven with an input pressure of 0.053MPa. The wavefronts are slightly shocked, and the positive pressure is larger than the negative pressure by 0.5MPa. (b) shows the magnitude of the positive and negative pressure for linear and nonlinear simulations, with pressures normalised to the magnitude of the positive linear pressure at 1MHz. As the input frequency increases, pressure at the focus increases linearly with frequency in the linear case. When nonlinearity is taken into account, the positive pressure increases at a faster rate, and negative at a slower rate than expected. The same effect occurs when increasing the source pressure.

As nonlinear effects have such a pronounced effect on rates of HIFU heating, accurate knowledge of B/A is important from a modelling approach. As temperature rises are so rapid, and because HIFU exposures often create large thermal lesions by making multiple exposures at overlapping locations, it is also very important to know how B/A changes with temperature and how it changes once tissue denatures.

The third effect is the discrepancy between positive and negative pressure in nonlinear focused fields. Figure 2.2 (a) shows a typical waveform at the focus of a HIFU transducer. In this example, the positive pressure is 1MPa larger than the negative pressure. Figure 2.2 (b) shows how this difference between positive and negative pressure increases with frequency. The same effect happens as the input pressure is increased. This means that the linear prediction of both positive and negative pressure being (a) equal and (b) linearly increasing with frequency and in-

put pressure is false. This effect is particularly important when determining cavitation thresholds which rely on the peak negative pressure, as doubling the input voltage to a transducer does not necessarily double the peak negative focal pressure.

2.1.2.1 Monitoring Changes in B/A

A further reason to monitor B/A throughout the processes of heating and denaturation is to determine whether there is a suitably large change in B/A in order to use it for monitoring HIFU therapy. As mentioned in 1.3.1.4 methods exist to detect lesions based on changes in acoustic attenuation of treated tissue. A similar method to the one suggested by (Liu et al., 2008) to measure temperature based on noninvasively determining B/A could be used to also determine whether tissue has been successfully treated or not. This would require a large change in the value of B/A in treated tissues. Studies by Silverman et al. (2006), Anand (2004), and Ebbini, Bischof, and Coad (2001) report large changes in received nonlinear signals from treated tissue, possibly suggesting a large change in B/A. However, while these papers detect changes in the nonlinear portion of the backscattered signal, it is unclear whether these are due to changes in the nonlinear properties of the tissue, or the nonlinear scattering of sound caused by acoustic cavitation. Characterising B/A as a function of temperature and denaturation will allow for important insight into the source of the nonlinear signals.

The nonlinearity parameter can be measured by a number of techniques and the most common for tissue is the finite amplitude insertion (FAIS) technique (see, e.g., Gong et al. (1989)) in which the rate of growth of the 2nd harmonic generated from a single frequency source is measured from which B/A can be determined (Law, Frizzell, and Dunn, 1985), (Errabolu et al., 1988). There are a number of studies measuring B/A of liver using the FAIS technique, summarised in Figure 2.11. Two

studies have reported the temperature dependence of B/A in ex-vivo liver (Lu et al., 2004), (Choi et al., 2011) and both found that it increased linearly with temperature. However only one of the studies increased the temperature high enough to induce thermal necrosis and they reported a 100 % increase in B/A post heating (Choi et al., 2011). This is an important result as it suggests that such a large change in B/A could be used for ultrasound based real time monitoring of HIFU treatment and will also impact nonlinear heating rates.

2.1.2.2 Measuring Thermally Induced Changes in B/A

In this chapter B/A is measured in liver as a function of temperature. An adapted version of the finite amplitude insertion (FAIS) technique is used to measure the attenuation and B/A of ex vivo bovine liver during a heating and cooling cycle reaching similar temperatures to those in HIFU ablation. In this work B/A was determined from measurements very near to the transmitting transducer face, to ensure plane wave conditions, and then fitting measured nonlinear waveforms to those simulated using the Burgers equation. This method has been used to determine B/A in a number of liquids (Chavrier, 2006), (Harris et al., 2007), and is easily extendable to the measurement of tissue samples. This method has a number of potential advantages as it removes the need for diffraction correction, is able to measure sound speed and attenuation without moving the sample, and is able to model the behaviour of arbitrary waveforms. As the only source available that was large enough for these experiments generated a nonlinear waveform with a significant third harmonic, this later advantage was particularly useful.

2.2 Materials and Methods

The experimental set-up for the measurements is shown in Figure 2.3. The sample was placed between two transducers: a 100mm diameter 1.125MHz unfocused transducer (Channel Industries, Santa Barbara, CA USA) and a 14mm diameter 2.25 MHz unfocused transducer (V306, Olympus Panametrics-NDT, Waltham, MA, USA). The smaller transducer was calibrated using a technique described in Section 2.2.2. For the sound speed and attenuation measurements the smaller transducer was attached to a pulser-receiver (DPR 300, JSR Ultrasonics, Pittsford, NY, USA) and the larger transducer used as a reflecting surface. The reflected pulse was recorded by an oscilloscope (Waverunner 104xi Teledyne LeCroy Chestnut Ridge NY, USA), and stored for later analysis using Matlab (Natick, MA, USA). For B/A measurements a signal generator sent 20 cycles at 1.125MHz through a 55dB broadband amplifier (1140LA, E&I, Rochester, NY, USA) to the larger transducer and the output voltage from the smaller transducer was recorded by the digital oscilloscope for a number of input levels. From these measurements through the same sample region all the acoustic properties could be determined.

Following the methods described by Chavrier (2006) and Harris et al. (2007) measurements are taken in the very near field of the transducer where, with appropriate time-gating of the signal it is possible to achieve plane wave conditions by avoiding edge diffraction effects. The region for plane wave conditions was determined by assuming the samples of tissue are a maximum 23mm thick and the transducer has a diameter of 100mm. At a frequency of 1.125MHz 20 cycles have a burst duration of 17.8μs. The time it takes for the central plane wave travel through the sample with a maximum speed of sound of 1600m/s is 15.6μs. The total time for the whole burst to reach the transducer is therefore 32.1μs. The distance from the edge of the large transducer to the receiving transducer is 51.4mm, so the time

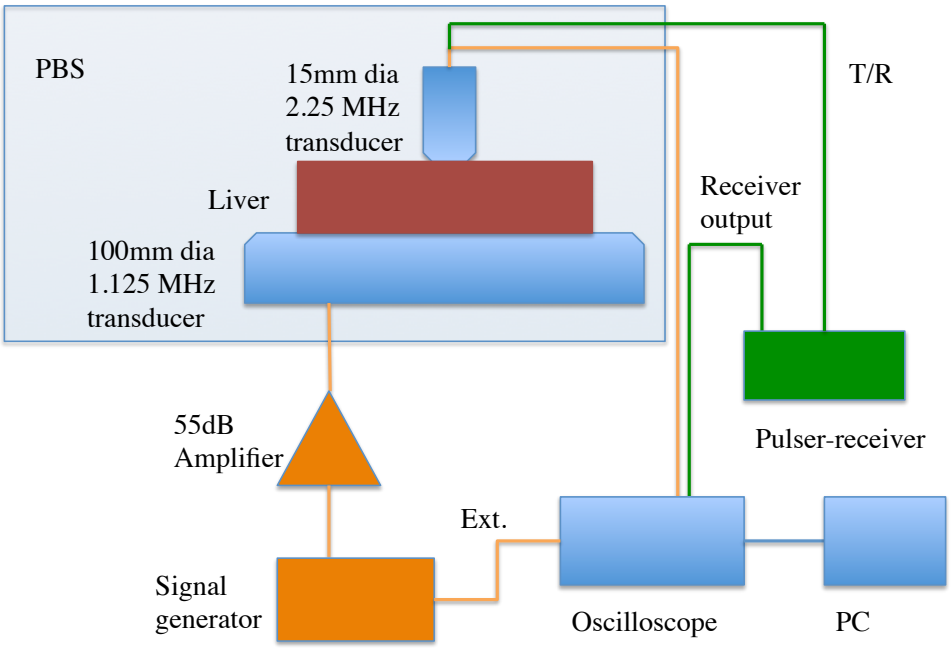

Figure 2.3: The experimental set-up for attenuation and B/A measurements. When measuring B/A the output of the 2.25 MHz transducer is connected to the oscilloscope, when measuring attenuation it is connected to the transmit/receive channel of the pulser/receiver and the 'receiver output' channel is connected to the oscilloscope.

taken for the edge wave to add diffraction effects is also 32.1µs. Therefore the 20 cycle pulse should act as a plane wave, however, to account for the ring up and down of the transmitting transducer only the middle ten cycles were analysed. As the transverse scan taken at this distance in Figure 2.4 shows, the pressure remains within 10% of the mean and phase within 15 degrees in the near field, which was deemed good enough to achieve plane wave conditions.

Fresh bovine liver tissue was obtained from an abattoir on the day of slaughter. It was cut into a cylinder of 100mm diameter and ≈23mm thick, and degassed by placing it in a vacuum chamber filled with Dulbecco's phosphate buffered saline (PBS) solution (Fisher Scientific Watham, MA, USA) at -0.7 bar for 1 hour. Experiments were conducted in a tank also filled with PBS, with a heater attached. It was noted that the temperature of the tissue changed more slowly than the temperature

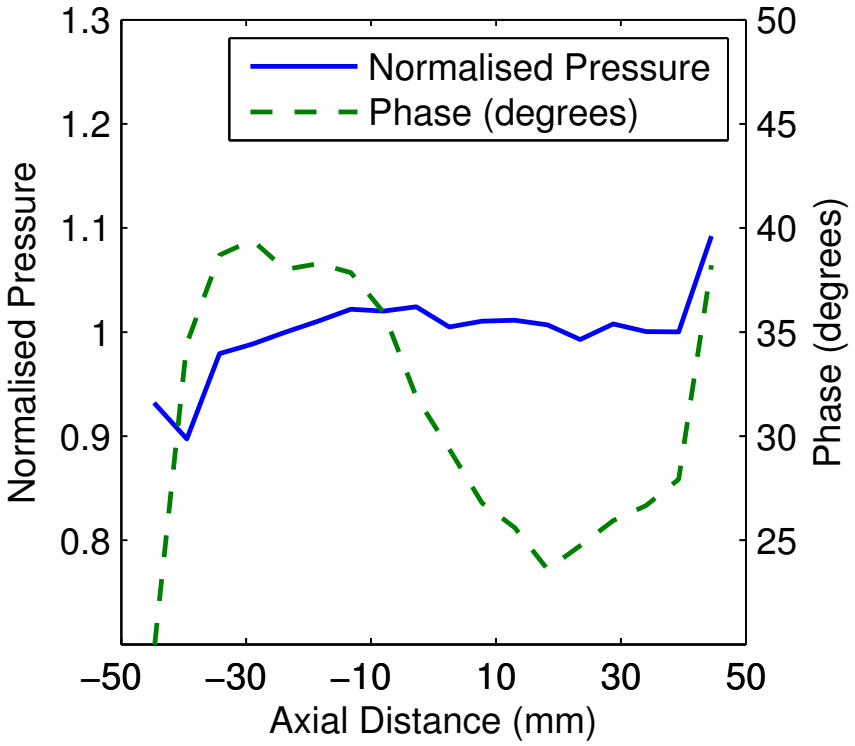

Figure 2.4: A transverse hydrophone scan across the face of the large transducer in the near field taken with a needle hydrophone at a distance of 24 mm measuring the normalised pressure amplitude and phase in the near field of the large transducer. Both the amplitude and phase remain constant over the middle 60mm of the transducer, with edge waves causing constructive and destructive interference at the edges. The phase changes by 15 degrees over the face of the transducer.

of the surrounding water. In order to ensure a uniform temperature distribution throughout the sample, and as inserting a thermocouple into the measured sample was impractical, a second sample of the same size was also kept in the tank with a needle thermocouple (Hyp-0 Omega Stamford, CT, USA) placed at its centre. Acoustic measurements in the first sample were taken when the centre of the second tissue sample reached the target temperature

Experiments were carried out at five different locations in five different liver samples. The temperature of the tank was initially at 23°C and measurements of all acoustic properties were taken. It was then raised to 37°C and 50°C, and mea-

surements were repeated at each temperature. The liver was then heated to 60°C, and left for 30 minutes to fully denature, and using the heat diffusion equation the temperature history difference between samples was calculated to be negligible. Although the commonly used CEM43 model (Sapareto and Dewey, 1984) predicts >96% cell death within 0.11s at 60°C, another published model O'Neill et al., 2011 predicts cell death after 17 minutes. Additionally, there are effects related to the liberation of fluid from the tissue due to thermal coagulation Graham et al., 1999a that take on the order of thirty minutes to appear in T2-weighted MRI images Chen et al., 1999. Leaving the tissue for thirty minutes therefore allows time for all thermal changes to the tissue to complete. The sample was then re-degassed and allowed to cool with measurements taken at 50 and 37°C. Not all samples had readings taken at every temperature point, although every sample followed the same heating/cooling cycle.

Results from multiple experiments are displayed individually, and are also combined to give a weighted average and a weighted variance, using the following formulae:

$$\bar{x} = \frac{\sum_{i=1}^{n}(x_i/\sigma_i^2)}{\sum_{i=1}^{n}(1/\sigma_i^2)} \tag{2.13}$$

$$\sigma^2 = \frac{\sum_{i=1}^{n}(1/\sigma_i^2)(x_i-\bar{x})^2}{\sum_{i=1}^{n}(1/\sigma_i^2)} \tag{2.14}$$

x_i and σ_i^2 are the average and variance for each measured value (attenuation coefficient, B/A, speed of sound) from the individual measurements in each individual liver sample, $bar(x)$ and σ^2 are the weighted average and variance across all samples.

The weighted value is the value that is the maximum likelihood estimate of the

measurements, if the measurements are assumed to be independent and normally distributed about the same mean. For determining statistical significance the data for all livers at the same temperature and state of denaturation were compared using a two-way ANOVA test to remove the effect of variation between livers, with a p value of 0.05 used for determining the threshold of significance.

2.2.1 Sound speed and density

The speed of sound was calculated by comparing the time of flight of a pulse sent and received by the 2.25MHz transducer and reflected from the 1.125 MHz transducer in PBS and in tissue for a constant distance between the two transducers. The constant distance was achieved by first measuring the time-of-flight in liver and then carefully removing the sample without disturbing the transducers and then taking the measurement in PBS. The speed of sound in PBS was measured to be equivalent to that in water and so the temperature dependent sound speed for water was employed (Marczak, 1997). The density of liver was measured as $1040\pm10 kg/m^3$ by weighing the tissue and measuring the volume of water it displaced.

2.2.2 Transducer Sensitivity

In order to measure attenuation and B/A it was necessary to determine the sensitivity of the receiving transducer. Calibrations were made at 1.125, 2.25 and 3.375MHz by comparing the voltage received by the transducer in the far field of an identical 15mm broadband transducer emitting tone bursts at the three frequencies 15 cycles long with a spatially averaged hydrophone scan over an area corresponding to the size of the smaller transducer. The phase response of the hydrophone was unknown. It was assumed that the phase response of the receive transducer was flat.

The difference in acoustic impedance between PBS and liver will lead to a

change in both the receive and transmit sensitivities of the two transducers when tissue is placed against them. This effect needs to be accounted for as small changes in amplitude can impact both the calculation of attenuation and nonlinearity. A method involving three measurements, as shown in Figure 2.5, was used to calculate the effect of the tissue on the transducers. The method involves sending a pulse from the pulser-receiver to the large transducer and measuring the response with the smaller transducer. The tissue was placed between the transducers, in three different positions: (a) in between the two transducers (b) touching the smaller transducer, and (c) touching the larger transducer. The expressions for the received voltage $y(\omega)$ for the three configurations can be written as

$$y_a(\omega) = S(\omega)\,T_{wt}\,A(\omega)\,T_{tw}\,R(\omega)\,u(\omega) \tag{2.15}$$

$$y_b(\omega) = S(\omega)\,T_{wt}\,A(\omega)\,C_{SR}\,R(\omega)\,u(\omega) \tag{2.16}$$

$$y_c(\omega) = S(\omega)\,C_{LT}\,A(\omega)\,T_{tw}\,R(\omega)\,u(\omega) \tag{2.17}$$

where $y(\omega)$ is the frequency spectrum of the received voltage, $u(\omega)$ is the input voltage, $S(\omega)$ is the transmit sensitivity (in Pa/V) of the large transducer in water and $R(\omega)$ the receive sensitivity (in V/Pa) of the small transducer in water. $A(\omega)$ is the (unknown) frequency dependent attenuation of the tissue, and T_{wt} and T_{tw} are the water-tissue and tissue-water transmission coefficients respectively, which can be calculated assuming plane wave conditions. Finally, $C_{LT}(\omega)$ is the correction to the transmit sensitivity of the large transducer due to tissue and $C_{SR}(\omega)$ the correction of the receive sensitivity of the small transducer. Manipulation of the three equations allows the corrections to be determined: $C_{LT}(\omega) = y_c(\omega) \times T_{wt}/y_a(\omega)$ and $C_{SR}(\omega) = y_b(\omega) \times T_{tw}/y_a(\omega)$. Identical experiments were conducted using a pair of the smaller transducers, in order to find $C_{ST}(\omega)$, the adjustment to be made to the transmit

sensitivity of the smaller transducer. The water layer at around 3-4mm was greater than twice the wavelength in tissue, so the issue of multiple reflections was avoided by time-gating the signal to only look at the first two cycles received.

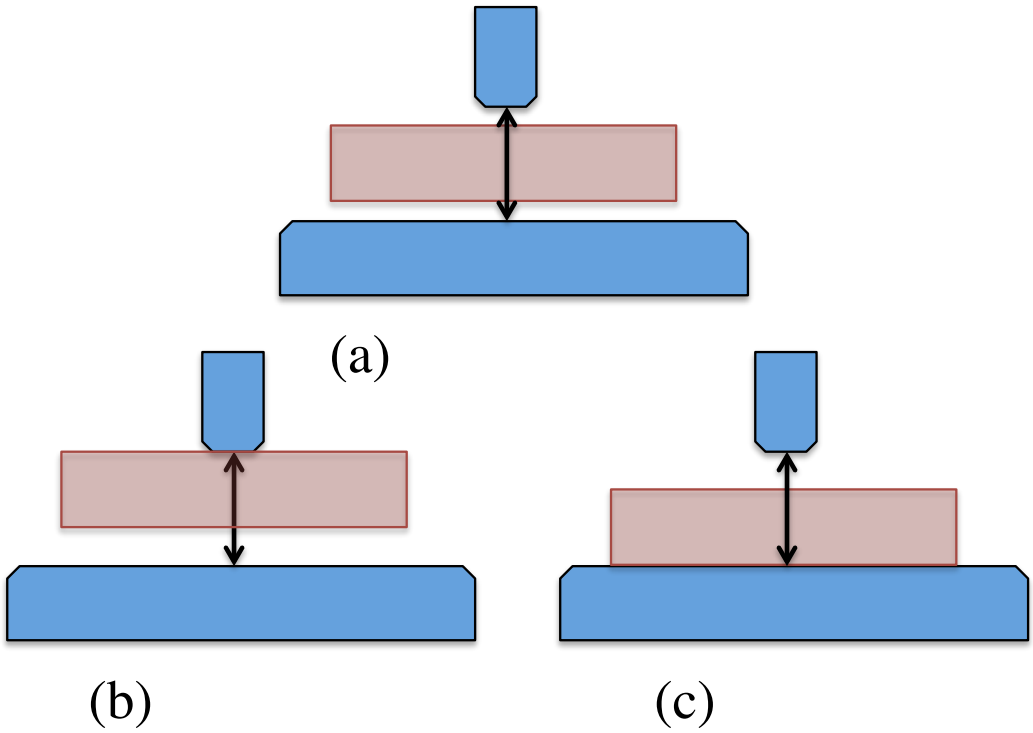

Figure 2.5: The configurations of transducers and tissue for determining the effect of acoustic impedance on transducer sensitivity, with the large 1.125 MHz transducer beneath the smaller 2.25 MHz transducer, and the position of the tissue indicated by the box in between the transducers. In each configuration a pulse is sent from the large transducer and measured with the smaller transducer.

2.2.3 Attenuation

When measuring the acoustic parameters the tissue was placed in between the two transducers, touching the face of each one, then the tissue was removed and a measurement taken in water. Attenuation in the sample was calculated by comparing the spectra of reflected pulses sent from the 2.25MHz transducer through water and tissue, using the large transducer as a reflecting interface. This configuration allowed for the B/A measurements to then be taken without moving the sample.

A maximum pressure amplitude of 10 kPa was used in the attenuation measurements, which was low enough that nonlinear effects, on the order of 1×10^4 times smaller than the fundamental, could be ignored. The attenuation was calculated using the formula

$$A(\omega) = \frac{y_t(\omega)}{y_w(\omega)} \frac{1}{C_{ST}(\omega) C_{SR}(\omega)} \frac{R_t}{R_w} \tag{2.18}$$

where y_t and y_w are the voltages recorded in tissue and water respectively, and $C_{ST}(\omega)$ and $C_{SR}(\omega)$ are the adjustments to the receive and transmit sensitivities of the smaller transducer due to the impedance of the tissue. R_t and R_w are the reflection coefficients at the large transducer face in tissue and water. This is then converted into an exponential attenuation coefficient based on distance.

With a typical acoustic impedance for PZT of 30MRayls (Grewe et al., 1990) the difference between R_t and R_w is less than 1.5%. At 2.25MHz (the central frequency of the smaller transducer), counting the two coefficients as identical leads to an underestimate of attenuation of less than 2%, if attenuation is assumed to be 4Np/m at 1MHz, increase with a power law of $f^{1.1}$ and the tissue is 25mm thick. Frequencies in bands 100KHz around the resonant frequencies of the transducer were ignored, due to the resonance of the transducer at these frequencies.

The attenuation coefficient in soft tissue was assumed to follow a power law of the form,

$$\alpha(f) = \alpha_0 \times \left(\frac{f}{1MHz} \right)^{\eta} \tag{2.19}$$

where α_0 is the attenuation in Np/m at 1 MHz, f is frequency and η is the power law exponent. The coefficients α_0 and η are calculated by fitting the power law expression to the measured attenuation.

2.2.4 Parameter of nonlinearity

In order to determine B/A it was assumed that the propagation could be modelled using plane waves. This was achieved by placing the receive transducer in the very near field of the large circular transducer. As described in section 2.2 for samples less than 23mm thick up to 17.8µs of plane waves could be recorded from the centre of the transducer before edge waves contributed to diffraction effects. Here a frequency domain version of the Burgers equation (Hamilton, L., and Blackstock, 1998a) was used as the nonlinear model. The pressure was taken to be harmonics of the driving frequency f_0 with corresponding fundamental angular frequency $\omega_0 = 2\pi f_0$

$$P(x,t) = \sum_{n=1}^{\infty} (P_n(x)e^{j\omega_0 t} + P_n^*(x)e^{-j\omega_0 t})/2 \tag{2.20}$$

where $P_n(x)$ is the complex coefficient of the n$^{\text{th}}$ harmonic as a function of distance and $*$ indicates the complex conjugate. The Burgers equation can be expressed in spectral form as (Ginsberg, Hamilton, and Blackstock, 1998).

$$\frac{dP_n}{dx} = -\alpha_n P_n + \frac{1}{\bar{x}} j \frac{n}{4} \left(\sum_{m=1}^{n-1} P_m P_{n-m} + \sum_{m=n+1}^{M} P_m P_{m-n}^* \right) \tag{2.21}$$

where x is the distance from the transducer, $\alpha_n = \alpha(nf)$ is the attenuation coefficient at the n$^{\text{th}}$ harmonic and $\bar{x}$ is the plane wave shock formation distance of the fundamental frequency. This nonlinear differential equation was solved using the inbuilt ode23 solver provided with MATLAB with 10 harmonics in the solution.

The measurements consisted of exciting the large transducer with a sinusoidal burst of 20 cycles at 1.125 MHz, sent through a the 55dB amplifier. After propagation the signal was detected by the smaller, calibrated receive transducer and converted into pressure. The amplitude of the burst sent by the signal generator was increased

from 100 to 900 mV (peak to peak) in 50mV increments. First, the nonlinear wave was measured in water and, using known properties of water, the source conditions at the first and third harmonics, $P_1(0)$ and $P_3(0)$, were determined. Measurements were then taken with the liver in place. The nonlinear propagation in liver was then simulated with the Burgers equation using the density, temperature-varying sound speed and attenuation measurements and adjusting for sensitivity changes, as described above. The value of B/A was then varied in the simulation until the predicted data matched the measured values.

2.3 RESULTS

2.3.1 The effect of acoustic impedance on transducer sensitivity

The effect of the tissue on the smaller transducer was to increase its transmit sensitivity by 4% and its receive sensitivity by 7%. It was found that the effect of the tissue on the loading of the larger transducer was to increase its transmit sensitivity by 0.1% at 1.125MHz and decrease the transmit sensitivity by 9% at 3.375MHz.

2.3.2 Sound speed

Figure 2.6 shows the dependence of sound speed with temperature. It increased significantly with temperature from 1567m/s at 23°C to 1599m/s at 50°C, and decreased again as it is cooled. The weighted average sound speed at 37°C after heating was 1584m/s compared with 1592m/s at 37°C before heating, a small, but statistically significant ($p<0.01$), decrease.

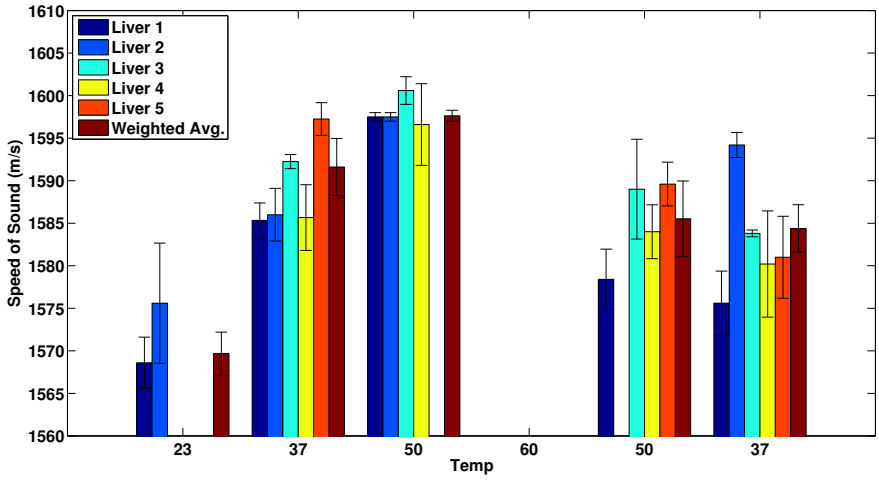

Figure 2.6: A plot of the sound-speed of ex vivo bovine liver in m/s during the heating/cooling cycle where the error bars represent one standard deviation. Speed of sound initially increased with temperature, then fell again with cooling.

2.3.3 Attenuation

Figures 2.7 and 2.8 show the attenuation at 1MHz and the power law exponent of frequency dependence of attenuation. Average attenuation at 1MHz initially decreased slightly with heating across samples, from 6.48±0.02Np/m at room temperature to 5.2±0.37Np/m at 50°C although this was not statistically significant. Post-heating there was a large, significant increase, with a weighted average value of 5.53±0.52 Np/m for untreated tissue at 37°C, which rose to 10.8±1.32 Np/m at the same temperature after denaturation. There was no consistent or statistically significant change in the power law exponent.

2.3.4 Parameter of nonlinearity

Figure 2.9(a) shows the amplitude of the second harmonic in water and tissue as a function of the source pressure amplitude at the fundamental for one liver at room temperature. Data is shown for both the measurements and for simulations using the Burgers equation. For the amplitude in water B/A was taken to be 5.0 at room

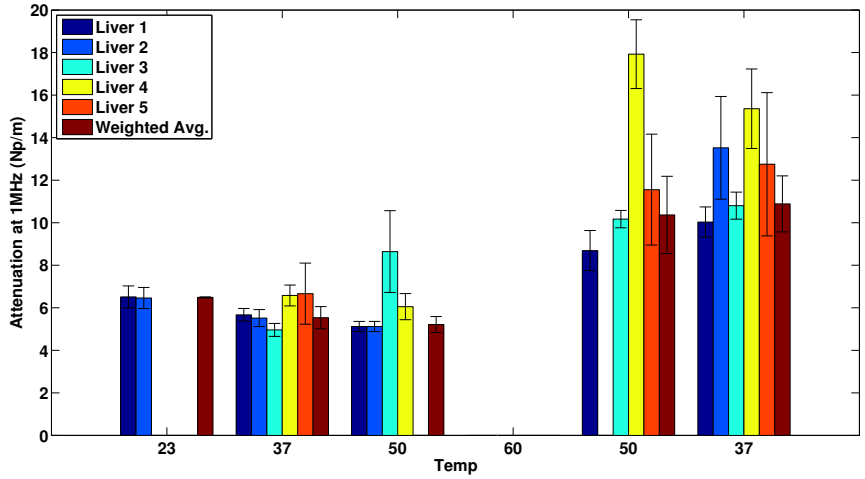

Figure 2.7: A plot of the attenuation of five ex vivo bovine liver samples during a heating/cooling cycle in Np/m converted to a 1 MHz reference where the error bars represent the standard variation. The average attenuation of liver decreases initially with heating, before rising as the liver begins to change irreversibly. Comparing pre- and post-heated tissue at 37°C shows a dramatic increase in the attenuation.

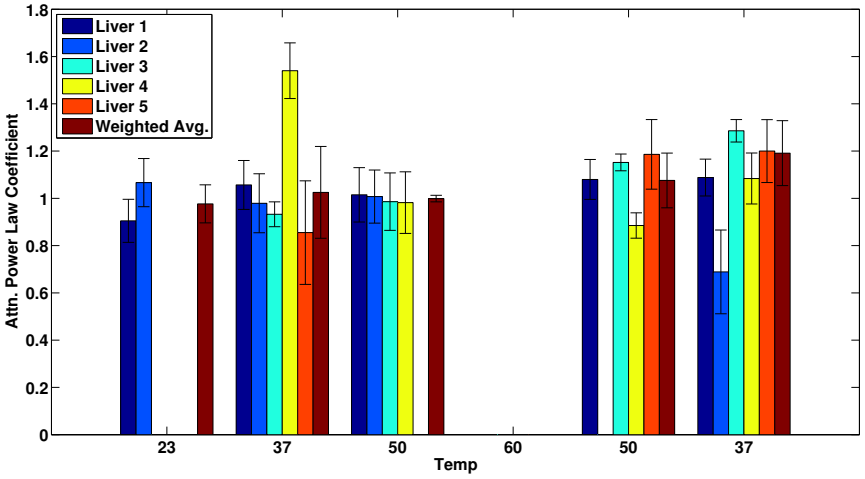

Figure 2.8: A plot of the attenuation power law coefficient during a heating/cooling cycle, where the error bars represent the standard deviation. There was no significant change of the power law exponent with temperature.

temperature (Beyer, Hamilton, and Blackstock, 1998b) and agreement between the model and measurements is excellent confirming that the plane wave approximation is valid for this experimental set-up. The simulated curve is also shown for the case when the third harmonic in the source was neglected showing that it was necessary to account for the presence of the third harmonic in the source condition.

B/A was found for tissue by minimising the error between the recorded and simulated values of the second harmonic. Figure 2.9(b) shows an example data set which resulted in determining B/A= 7.3 for this particular sample. The method employed here resulted in B/A=7.14±0.07 - a value that was consistent with the literature, see the discussion. The variance of 0.07 is the weighted variance calculated in equation 2.14 and is due to the variation between different samples.

Figure 2.10 shows the variation in B/A with the heating and cooling cycle for the five livers. As the temperature increased from 23°C to 50°C the weighted mean of B/A increased from 7.19±0.12 to 8.53±0.71, with the average B/A of each individual liver increasing. Once the tissue had denatured there was no significant difference in the values of B/A.

2.4 Discussion

2.4.1 The measurement method

Here we considered the effect of thermal denaturation on the nonlinear acoustic properties of tissue. A new configuration for measuring the acoustic properties of tissue samples, including B/A, was presented. One advantage of the technique is that it allows for sound speed, attenuation and nonlinearity coefficient to be measured without disturbing the sample. Also because the measurements are carried out using a quasi-plane wave, we speculate that the signal-to-noise ratio of this

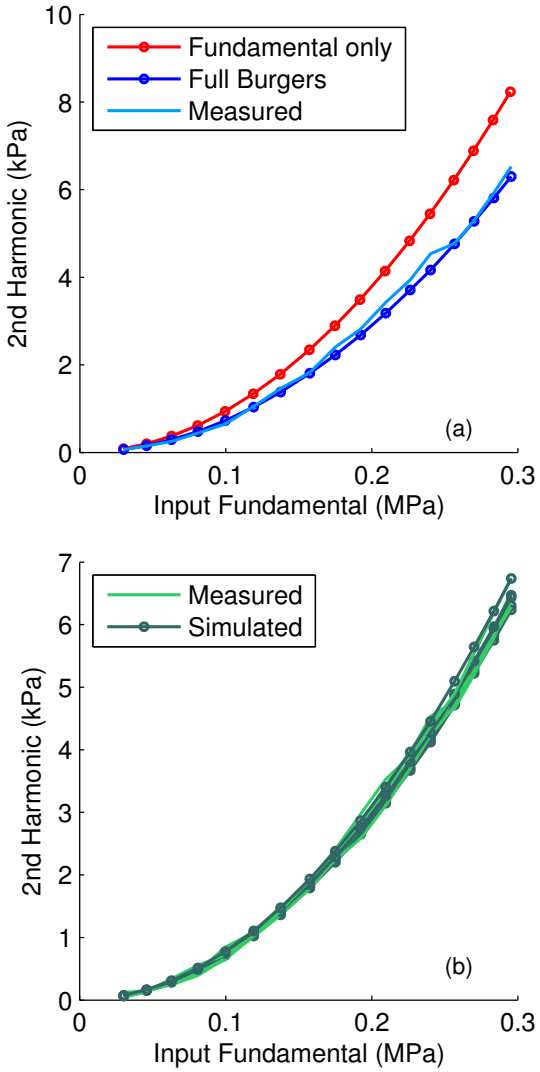

Figure 2.9: (a) A graph of the second harmonic amplitude against the amplitude of the input signal at the fundamental frequency in water. The dark blue dotted line is simulated and the light blue measured, showing good agreement. The red solid line shows the simulation neglecting the effect of the third harmonic in the source.(b) shows the amplitude of the second harmonic measured at five locations in one sample of liver (light green solid) and the simulated data for each location in dark green dotted lines.

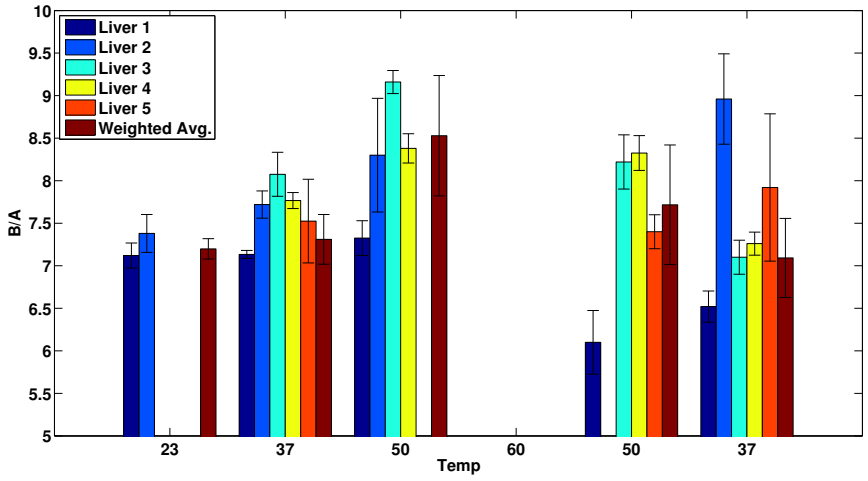

Figure 2.10: A plot of the B/A of ex vivo bovine liver during a heating cooling cycle, where the error bars represent one standard deviation. B/A increases significantly between 37 and 50°C ($p < 0.05$), but there is no significant change between denatured and fresh tissue at 37°C.

method may be improved compared to the methods most widely used method for measuring B/A in biological samples, where either complex diffraction correction is needed (Gong et al., 1989) or plane wave-like conditions are created by being outside the Rayleigh distance, and an acoustic absorber is employed to remove any second harmonic component that has generated in the near field (Dong et al., 1999). In the former case errors in the diffraction correction manifest themselves in the B/A estimate. In the latter case being in the very far field and using an absorber means that amplitudes are low and nonlinear distortion weak. In the method described here the wave is quasi-planar because we are in the near-field and the amplitudes are higher.

The method developed was shown to provide good agreement with the nonlinearity coefficient of water, and has previously been shown to accurately measure B/A in other well-documented liquids (Chavrier, 2006), Harris et al., 2007. Measurements of B/A in fresh liver also showed good agreement with literature values for

fresh tissue, and are shown in Figure 2.11. This shows that the method can be extended to measuring samples of ex-vivo tissue, and that the measurements made in fresh tissue can be reliably compared with those made in denatured tissue to detect any thermally induced changes.

2.4.2 The effects of temperature and denaturation on acoustic properties

The speed of sound was measured as 1574±1.3m/s, which agrees well with literature values of 1608 m/s Law, Frizzell, and Dunn (1985), 1580 m/s (Techavipoo et al., 2012) and 1558 m/s (Bush et al., 1993). The attenuation value at 1 MHz was 0.481±0 0.045 dB/cm at 37°C and increased almost linearly with frequency. The frequency relationship and attenuation values are within the wide range of reported values for attenuation in liver tissue: 0.56 dB/cm at 1MHz (Choi et al., 2011), 4.01 dB/cm at 5MHz (which corresponds to 0.80 at 1MHz, assuming linear variation of attenuation with frequency) (Techavipoo et al., 2012), 0.69 dB/cm at 1MHz (Goss, Frizzell, and Dunn, 1979)), 2.99 dB/cm at 3MHz (1.00 at 1MHz), (Bush et al., 1993), 0.35 dB/cm at 1MHz (Zderic et al., 2004) and 0.80 at 2.4MHz dB/cm (0.33 at 1MHz) (Clarke, Bush, and Ter Haar, 2003). The measurements of B/A were also consistent with literature values, as shown in Figure 2.11.

For sound speed we observed an initial increase as temperature rose to 50°C which is consistent with other reports Choi et al., 2011. After thermal denaturation a small decrease in the speed of sound was found. The literature is not consistent on this measurement. Some reports suggest a slight increase (Bush et al., 1993; Choi et al., 2011), one report has shown both slight increases and decreases (Techavipoo et al., 2012). In all cases the changes were slight and it appears that variability is likely greater than any underlying trend.

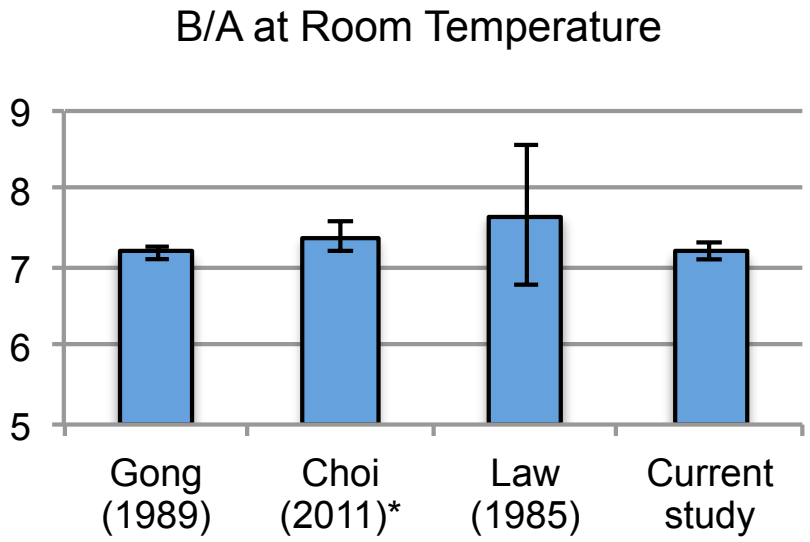

Figure 2.11: The weighted value of B/A measured in this study compared with values of B/A measured by Gong et al. (1989), and Law, Frizzell, and Dunn (1985) for bovine liver at room temperature, and the value for porcine liver reported by Choi et al. (2011). There is good agreement between our measurements and previously reported values. Our data was not inconsistent with values in the literature in this case. Note that for Choi et al. (2011), the data is taken at 30°C, the lowest temperature reported in this study.

For acoustic attenuation an increase of 140% was measured here which is consistent with other reports on the literature (see Figure 2.12). We observed no statistically significant change in the frequency dependence of tissue over the five samples tested here. We note that Choi et al. (2011) reported a drop in the power law exponent, but this was only in one sample and we also observed a drop in one of our samples. Zderic et al. (2004) reported a drop in the power law exponent for liver and spleen but an increase in abdominal wall. However they also noted that their power law exponents were lower than other reports in the literature. Our results are therefore within the range of variability observed in the literature.

The key result for this work was determining the change in the nonlinearity parameter for a heating and cooling cycle. We observed that during heating B/A of

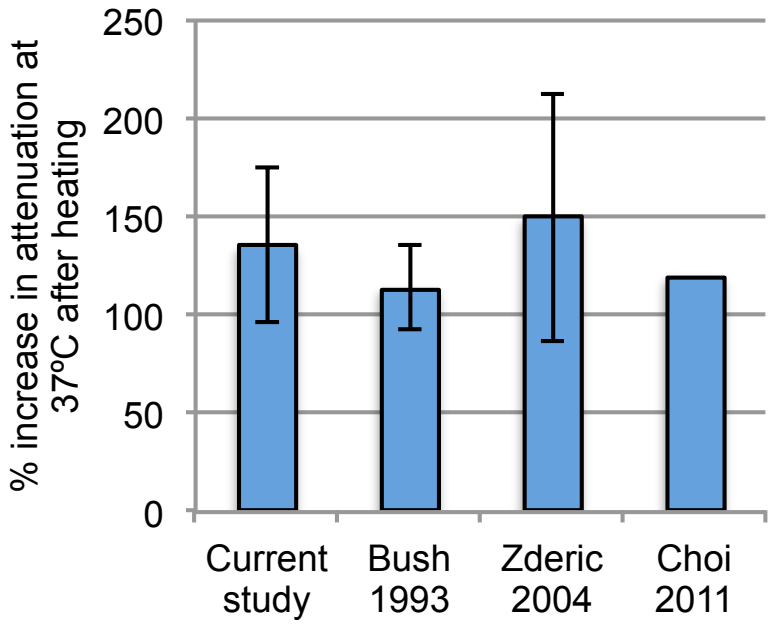

Figure 2.12: A plot of the increase in attenuation of ex vivo liver after heating, comparing values measured in this study with those reported by Bush et al. (1993) and Choi et al. (2011), Zderic et al. (2004) and Choi et al. (2011). As can be seen, the increase in post-heating attenuation can vary widely, and the increases reported in this study agree well with those reported elsewhere.

fresh tissue increased with temperature at an average rate of 0.048/°C and this is within the range in literature data of 0.073/°C (Choi et al., 2011), 0.099/°C (Lu et al., 2004), 0.067 (Liu et al., 2008) and 0.026/ °C (Sehgal et al., 1986) However after thermal denaturation, we found no significant increase in B/A, which is in stark contrast to the twofold increase reported by Choi.

It is possible the differences in the methods may have contributed to the discrepancy. We considered three potential differences that may have affected the results. First, the two studies employed a different temperature history: in this study the maximum temperature was 60°C, while in Choi et al. (2011)the maximum temperature was 75°C. However given that the rise in attenuation in both studies was in line with previously reported values for thermally denatured tissue we anticipate

this was not a significant effect. Second in the study by Choi et al. (2011)) the attenuation data were taken in one sample of liver, and this values was used to determine B/A in a separate experiment with a different sample. In this study, attenuation was measured separately and in situ for each sample. The effect of employing attenuation from different samples was modelled by recalculating the value of B/A over the range of measured values of attenuation for denatured tissue and despite the variation the value of B/A varied by less than 20%. Lastly, in this study all samples were de-gassed after heating before cooling, to remove any bubbles that may have formed during the heating process. It is possible that bubbles formed during heating may have contribute to the large rise in B/A reported by Choi et al. (2011) An experiment was carried out to test this theory by not degassing the sample but no difference in B/A was observed. However, this does not mean that bubbles were necessarily present in our sample and we speculate the presence of bubbles is the most likely explanation for the discrepancy between our study and that of Choi et al.

We note that both this study and that of Choi et al. (2011) employed a water bath to simulate the heating associated with HIFU exposure. Water bath heating is slower than HIFU heating, and there is no mechanical effect contributing to denaturation, either from the pressure field displacing the tissue or from the mechanical effect of cavitating bubbles, and it remains to be seen whether this different process of denaturation has an effect on the way the acoustic properties of tissue change.

2.5 Conclusions

A method based on the finite amplitude insertion method was adapted to measure the attenuation coefficient and nonlinear parameter of ex-vivo bovine liver during a heating/cooling cycle designed to replicate a treatment by high intensity thera-

peutic ultrasound. The method improves the signal to noise ratio of previous techniques and produces results that agree well with literature data for sound-speed, attenuation and B/A of fresh tissue. After heating and cooling tissue it was found that only attenuation demonstrated a significant change post-denaturation, a result consistent with the literature. Notably we found that B/A did not change significantly after denaturation. As the nonlinearity of tissue can only be detected by monitoring the nonlinear progression of waves through nonlinear media, and that HIFU lesions will make up a small fraction of the acoustic path length in most monitoring geometries, we speculate that a very large change in B/A is needed to detect lesions. Our results suggest that firstly B/A is not a robust indicator of tissue state in HIFU and secondly that heating rates will not be significantly affected by changes in B/A during HIFU ablation.

CHAPTER 3

COMPARING TWO METHODS FOR MODELLING NONLINEAR FOCUSED ULTRASOUND FIELDS

3.1 INTRODUCTION

In chapter 2 it was shown that in order to accurately model or predict the effects of HIFU treatment it is important to capture the effects of nonlinearity on the acoustic field, and the importance of using the correct value for the parameter of nonlinearity, B/A. In this chapter we examine the accuracy of two different methods of modelling nonlinear effects in focused acoustic fields often used in HIFU.

The first method uses a numerical solution to the Khokhlov-Zabolotskaya-Kuznetzov (KZK) equation (Zabolotskaya and Khokhlov, 1969), (V.P., 1971). The KZK equation has become so widely used it can be considered one of the basic equations of nonlinear acoustics (Rudenko, 2010) and has been shown to agree well with hydrophone measurements of highly nonlinear fields (Canney et al., 2008).

The second method is a commercial software package known as PZFlex (Wojcik et al., 1993) which uses a finite element approach for solving nonlinear propagation. PZFlex is becoming popular as a tool for transducer design. While PZFlex has been shown to agree well with various analytical solutions and approximations to nonlinear fields (Wojcik et al., 1993) there are no existing validations of PZFlex against other methods for calculating nonlinear fields or against measurements of nonlinear HIFU fields.

In this chapter we compare PZFlex against KZK simulations and multiple hydrophone measurements of focused acoustic fields of HIFU transducers used at therapeutic pressures. Our measurements and simulations show that PZFlex appears to underestimate the growth of harmonics due to nonlinear distortion, and incorrectly models the shape of higher harmonics.

3.1.1 KZK Equation

Section 2.1.1 described the Burgers equation- a 1-D wave equation that accounted for absorption and finite-amplitude nonlinearity. The KZK equation is an augmentation of the Burgers equation that additionally accounts for the effect of diffraction in directional sound beams. The KZK equation is derived by invoking the paraxial approximation.This is the assumption that the envelope of the wave is propagating predominantly in the z direction and that the pressure envelope varies slowly in z compared to variations in x and y. For this to be the case a commonly held rule of thumb states that the solution is only valid for angles of less than 20 degrees from any point on the source as shown in figure 3.1. In HIFU, transducers typically have an aperture diameter that is close to the focal length, making the focus at 30°to the edge of the transducer, which violates this rule. Nevertheless, many papers use transducers with lower f-numbers (Canney et al., 2008; Khokhlova et al., 2006; Bailey

et al., 2001) and achieve good agreement with hydrophone measurements.

In axially symmetric coordinates the KZK equation can be written as

$$\frac{\partial^2 p}{\partial z \partial \tau} - \frac{c_0}{2}\nabla_\perp^2 p - \frac{\delta}{2c_0^3}\frac{\partial^3 p}{\partial \tau^3} = \frac{\beta}{2\rho_0 c_0^3}\frac{\partial^2 p^2}{\partial \tau^2} \tag{3.1}$$

where p is pressure, τ is retarded time $t - z/c_0$, β is the coefficient of nonlinearity, ρ_0 and c_0 are density and sound speed, δ is diffusivity, z is the direction of the sound beam and $\nabla_\perp^2 = \frac{1}{r}\frac{\partial}{\partial r} + \frac{\partial^2}{\partial r^2}$ is a Laplacian that operates in the plane perpendicular to the axis of the beam. In this paper the solution used is the 'Texas' code developed by (Lee and Hamilton, 1995) which solves each part of the equation - attenuation, diffraction and nonlinearity - in separate steps using finite difference methods.

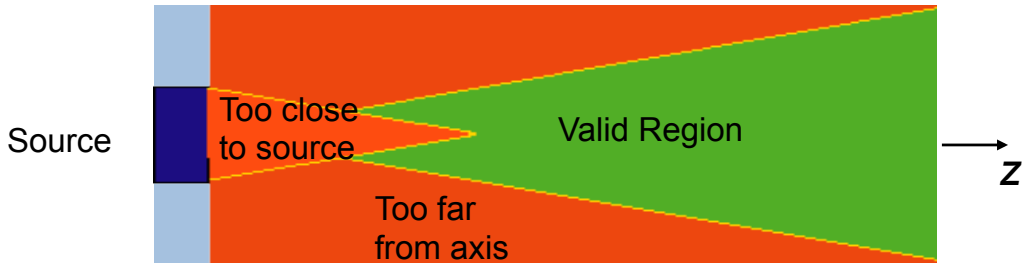

Figure 3.1: A plot of the rough areas of validity for KZK solutions, courtesy of R. Cleveland. A rule of thumb states that the solution is valid at any point less than 20 degrees from any point on the source.

3.1.2 PZFlex

PZFlex uses a finite element method to solve incrementally linear versions of the continuity, momentum and state equations directly, rather than combining them into a wave equation. For the equation of state they use the B/A 2nd order expansion of the Taylor series relationship between pressure and density (Wojcik et al., 1995; Wojcik et al., 1993). Incrementally linear refers to the process of advancing a solution in time by discrete increments and modifying material properties at the

end of each according to the instantaneous and/or historical (integrated) state of the material. Suitably small increments are chosen for the solution to be linear to first order over each increment(Wojcik et al., 1995). In the case of nonlinear propagation this involves solving linear versions of the continuity and momentum equations and updating the pressure dependent speed of sound between each time step. In this way it captures all second order effects, in the same way as the full second order wave equation.

Although this approximation will result in a solution accurate to second order it is known that at too many wavelengths from the source the method can become inaccurate as errors are propagated through the solution (Wojcik et al., 1997). Although there is no exact measure for the number of wavelengths required to cause errors, it is suggested that the order of hundreds of wavelengths may cause problems.

Very few experimental validations for PZFlex exist. Those that do exist are for nonlinear pulses from imaging transducers using PZflex's spectral method rather than finite elements (Wojcik et al., 1998). For the finite element method, it has been shown that the solution for a focused HIFU source matches approximations for the growth of harmonics to within 10% (Wojcik et al., 1998). Apart from this there are no validations for finite-element PZFlex against either the KZK solution or hydrophone measurements.

The lack of validation of PZFlex against other simulation methods or hydrophones mean that testing the accuracy of PZFlex must be conducted if it can be trusted as a method of treatment planning and modelling.

3.2 METHODS

The accuracy of each modelling method was analysed by comparing the simulations to hydrophone measurements of acoustic fields of HIFU transducers at different frequencies and pressures. Three different HIFU transducers were used: a 1MHz HIFU transducer, (Precision Acoustics, UK) a 0.5MHz transducer (H107, Sonic Concepts, WA) and a 1.1MHz transducer driven at its third harmonic (H105, Sonic Concepts, WA).

First the KZK and PZFlex simulations were used to produce linear simulations of the field at low pressures, where the loss in pressure at the fundamental is negligible and the positive pressure is equal to negative pressure. This was done to ensure the geometry of the simulated transducers accurately capture the shape of the focused field, and to determine the relationship between the applied voltage to the transducer and the initial p_0 surface pressure input to the KZK code and the surface velocity term that is used as the input to PZFlex.

Once the fields had been successfully modelled at low pressures, the source conditions were increased to those used in HIFU treatments, where nonlinearity begins to have an effect. At this stage the two simulation methods were compared to the fields measured by the three hydrophones.

3.2.1 Inputs to the KZK Equation

In addition to the acoustic properties of water the KZK equation takes as its input source a function of the form $p = p_0 F(r,t)$ where p_0 is a characteristic pressure and $F(r,t)$ captures the curvature of the source by relating time dependence to radial position in the source plane (Lee and Hamilton, 1995). The number of harmonics in the solution is specified as well as the number of time points in the wave form, and

the number of radial points. There is a limit to the maximum number of each due to memory requirements, but temporal and radial resolution did not affect the results. The simulation used a waveform with 20 cycles, zero-padded front and back, 270 time points per cycle, 2500 radial points between the origin and the radius of the transducer and 7 harmonics in the solution and a spatial step of 5e-4 relative to a normalised distance of 1 to the geometric focus. These settings were chosen by modifying the values until increasing the number of cycles, harmonics, numbers of points, or decreasing the spatial step no longer affected the solution.

The output to the solution was given in terms of pressure amplitudes at the different harmonics in a 2-d grid for distances 1.5 times the length of the focus of the transducer and equal to the radius.

3.2.2 Inputs to PZFlex

In PZFlex models, focused transducers are modelled as a rigid structure and a velocity condition is applied normally to the surface of the transducers as an acoustic source. 8 element hexahedral nodes are used for meshing the model. The velocity condition was chosen to match measured output pressure at the fundamental at low pressures, and then increased linearly with applied voltage at higher intensities. The grid spacing uses 60 elements per wavelength of fundamental frequency at the slowest velocity, as this provides 15 elements per wavelength at the third harmonic, which is necessary for negligible numerical dispersion. The explicit algorithm used by PZFlex is conditionally unstable, so in the code the time step is set to a fraction of the Courant-Friedrichs-Lewy limit- a necessary condition for convergence while solving certain partial differential equations. In this paper, the value of the time-step is chosen to be 0.8 times the CFL limit.

3.2.3 Hydrophones

Three hydrophones were used to measure the acoustic field; a Precision Acoustics (PA) needle hydrophone (75 micron probe Needle Hydrophone, Precision Acoustics, UK), an Onda needle hydrophone (HNA-0400, Onda, CA) and a Fabry-Perot Optical Hydrophone (FOH) (Fibre-Optic Hydrophone, Precision Acoustics, UK). The PA needle and Onda hydrophones both use a small piezoelectric polyvinylidene (PVdF) membrane in the tip of the hydrophone connected to a particular preamplifier to create a voltage output. The FOH uses a different principle. The tip of the FOH is a 10µm polymer spacer sandwiched between a pair of gold mirrors. Light emitted by a tuneable laser hits the tip and is reflected back down the fibre. The interference between the two reflectors in the tip produces a phase shift in the reflected light that depends on acoustically-driven changes to the thickness of the tip. This phase change can be demodulated to obtain a measure of pressure (Morris et al., 2009).

The sensors of the hydrophones will spatially average over the active area of the hydrophone. This was taken into account in the simulations by applying a spatial averaging in the radial direction to the simulations. The hydrophone most sensitive to spatial averaging was the Onda, as it had an effective radius of 400 µm, compared to the the PA needle hydrophone (75µm) and the FOH (10µm).

The PA needle and the Onda hydrophones had been calibrated in increments of 1MHz and 0.1MHz respectively in units of mV/MPa. For sensitivities in between calibrated frequencies the sensitivity of the hydrophones was estimated by linear interpolation.

The fibre optic hydrophone was placed with the fibre perpendicular to the acoustic beam, as it was found that when aligned with the axis of the HIFU transducer it suffered from artefacts caused by reflections from the hydrophone holder.

These artefacts disappear in the perpendicular orientation but it was necessary to recalibrate the hydrophone as it has been shown that its sensitivity decreases with angle and that each frequency is reduced by a different amount (Morris et al., 2009).

3.2.3.1 Hydrophone Calibration

The FOH was calibrated in the far field of a 25mm radius, unfocused, broadband transducer with a central frequency of 2.25MHz (Immersion Transducer, Olympus Corp, Japan) at a distance of 1m. The transducer was driven by a signal generator (Agilent 33250A) connected to a 55dB broadband amplifier (1140LA, E&I, Rochester, NY, USA). Waveforms measured with the FOH in this position were compared with measurements taken with the Onda and PA needle hydrophones. At this distance the hydrophone is outside the Rayleigh distance of the transducer and the wave is spherical. In addition, the distance is such that the waveform has developed significant nonlinearity and has formed steep shocked wavefronts. This creates a waveform containing the original frequency and a series of harmonics up to around 15MHz that allows calibration at frequencies higher than the source transducer can output.

At each harmonic n of the input frequency the sensitivity $S_f(n)$ of the FOH was calculated using the formula

$$S_f(n) = S_{ref}(n)\frac{V_f(n)}{V_{ref}(n)} \tag{3.2}$$

where S_{ref} is the sensitivity of the reference hydrophone, V_f and V_{ref} are the voltage amplitudes measured on the FOH and reference hydrophones respectively. Phase response data was unavailable for the reference hydrophones, but this was not required for analysing the relative magnitudes of the harmonics.

Readings were taken for input frequencies of 1, 1.1, 1.5, 2, 2.2 and 2.5 MHz. For the frequencies where there was overlap between the harmonics the average of the two sensitivities was used. The sensitivity was calculated by taking the average of the sensitivities calculated from the two reference hydrophones.

3.2.4 Measurement and Modelling Approach for Simulating Acoustic Fields

The KZK and PZFlex simulations were run with nonlinearity turned off to ensure they captured the linear field of the transducer. These were compared to hydrophone scans at very low pressures and to two linear analytical solutions to the field of a focusing transducer; the O'Neil (1949) solution and the Fresnel solution (Lucas and Muir, 1982). The difference between the two solutions is that the Fresnel solution applies the same paraxial approximation made by the KZK solution. The pressure was then increased to levels where nonlinearity became appreciable, that is, measurable harmonics begin to appear in the spectrum of the waveform. A maximum of pressure of 5MPa was employed as, above these pressures, even in degassed, filtered water, cavitation was observed which could damage the hydrophones.

To perform the hydrophone scans the HIFU transducers were driven by tone bursts 20 cycles long sent from a signal generator through a 55dB broadband amplifier connected to the transducer via each transducer's impedance matching network. The experiments took place inside tanks of filtered, degassed, de-ionised water at room temperature. The hydrophones were attached to a computer controlled movement stage and received voltages recorded on an oscilloscope. The hydrophones were aligned to the focus by finding the maximum value of pressure in the transverse plane, and then moving to the geometric focus based on time-of-

flight calculated from the speed of sound in water, at the temperature measured in the tank.

3.3 RESULTS

3.3.1 Linear Modelling

The geometry of the central hole in some of the transducers was suitably captured in the linear solutions by subtracting the field of a transducer the same size as the hole from the solution for the O'Neil and Fresnel solutions. In the KZK solution the hole was successfully modelled by setting the pressure to zero within the hole radius.

For the 3.3MHz transducer, figure 3.2 shows hydrophone measurements at low pressure compared with linear KZK and PZFlex simulations, and two linear solutions for focused acoustic fields- the O'Neil solution O'Neil, 1949 and one based on the Fresnel approximation. The geometry of the central hole in some of the transducers was suitably captured in the linear solutions by subtracting the field of a transducer the same size as the hole from the solution for the O'Neil and Fresnel solutions. In the KZK solution the hole was successfully modelled by setting the pressure to zero within the hole radius. The physical dimensions of the transducer given in the data sheet are aperture radius 32mm, central hole radius 12mm, focal length 62.6mm. These dimensions were used as the input to the O'Neil solution. To match the positions of the nodes, the KZK, PZFlex and Fresnel solution used slightly different dimensions of 31mm for aperture radius, and 10mm for the hole. The same values were used for the geometry of the identically sized 0.5MHz transducer. The 1MHz transducer was successfully modelled using its geometry of 75mm focal length and 28mm aperture radius for all the simultaions.

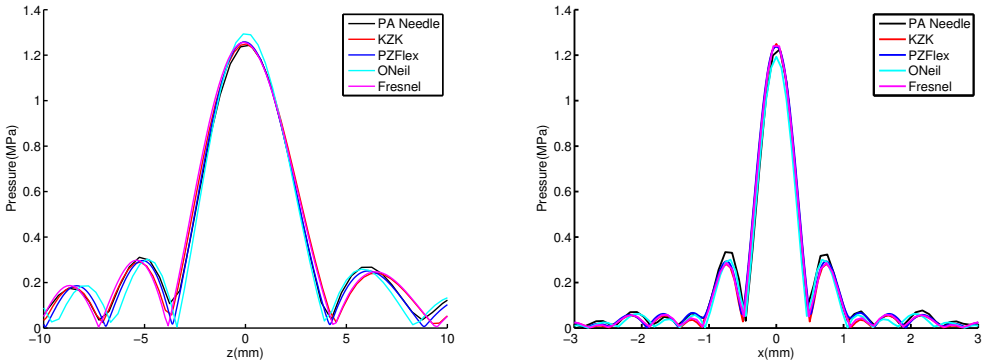

(a) (b)

Figure 3.2: A comparison of hydrophone data, KZK and PZFlex simulations, the O'Neil solutions and the Fresnel solution for the axial and transverse pressure fields at the focus of the 3MHz transducer. The physical dimensions of the transducer given in the data sheet are aperture radius 32mm, central hole radius 12mm, focal length 62.6mm. These dimensions were used as the input to the O'Neil solution. To match the positions of the nodes, the KZK, PZFlex and Fresnel solution used dimensions of 31 for aperture radius, and 10mm for the hole.

3.3.2 0.5 MHz Transducer

The first transducer modelled was a 0.5 MHz HIFU transducer (Sonic Concepts, WA). It had a centre frequency of 0.5MHz, focal length of 62.6mm and aperture radius of 32mm. The hole in the centre of the transducer was 10mm radius. The only hydrophone calibrated at 0.5MHz was the Onda. The field is broad enough at this frequency that spatial averaging was negligible. Figure 3.3 shows good agreement between the measurements and both simulations of the first and second harmonics at the focus for the two pressures.

3.3.3 1MHz Transducer

The next transducer was a 1MHz HIFU transducer (Precision Acoustics, UK). It had a centre frequency of 1MHz, focal length of 75mm and aperture radius of 28mm.

For the 1MHz transducer there was reasonable agreement between the two sim-

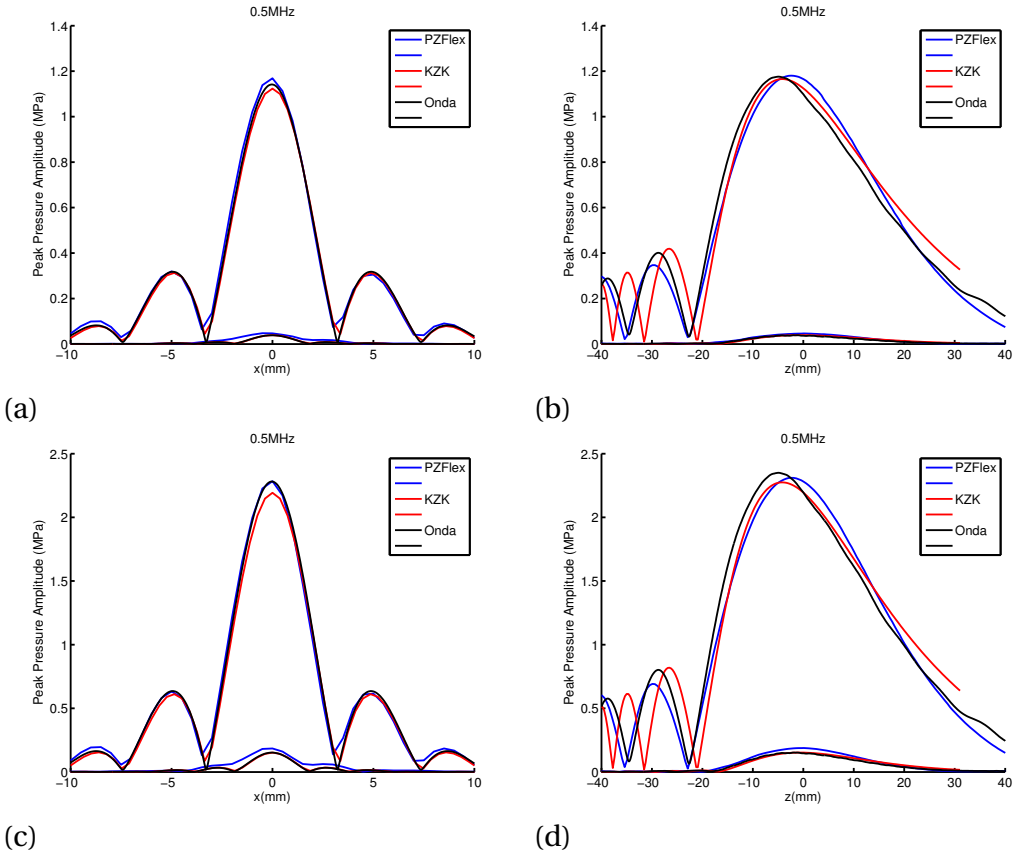

Figure 3.3: A plot of the first and second harmonic pressures generated by a transducer at 0.5MHz in the radial (a,c) and axial (b,d) directions and at an input voltage to the matching network of 62V (a,b) and 124V (c,d). The black lines show the hydrophone measurements taken by the Onda hydrophone, the blue lines show simulations in PZFlex and the red lines are KZK simulations. There is good agreement at the focus between all three methods.

ulations and hydrophone measurements at the focus at low pressures, as shown in figure 3.4. In the axial direction, the lack of pre-focal nulls measured by the hydrophone strongly suggested that the source was not an ideal piston. As the input voltage increased the agreement worsened, with the measured second harmonic larger than simulations predicted, and the third harmonic was completely different in shape to the simulations. A possible reason for this was the presence of a third harmonic component in the source. In order to test this hypothesis hydrophone readings were taken at much higher voltages over the face of the transducer using

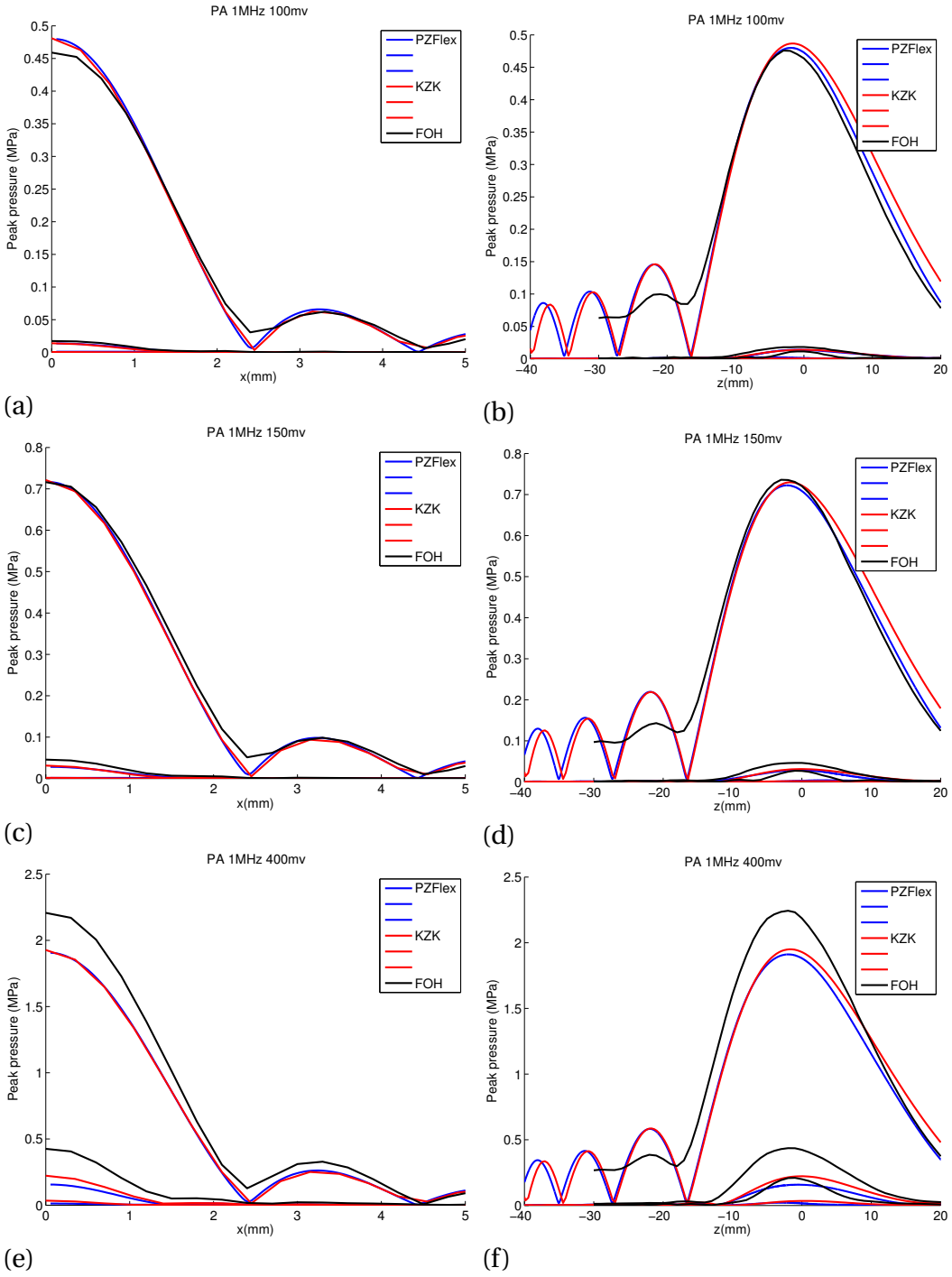

Figure 3.4: A plot of the first, second and third harmonic pressures generated by the 1MHz transducer in the transverse and axial directions. Three driving voltages at the signal generator are shown (100,150 and 400mv) corresponding to 56, 84 and 225V at the matching network. The FOH measurements, KZK and PZFlex simulations are shown. The lack of nulls in the axial direction suggests the source was not a perfect piston. As the driving amplitude increases the second and third harmonic increase in a way not accurately captured by either the KZK or PZFlex simulations, and the harmonics generated by KZK become greater than by PZFlex.

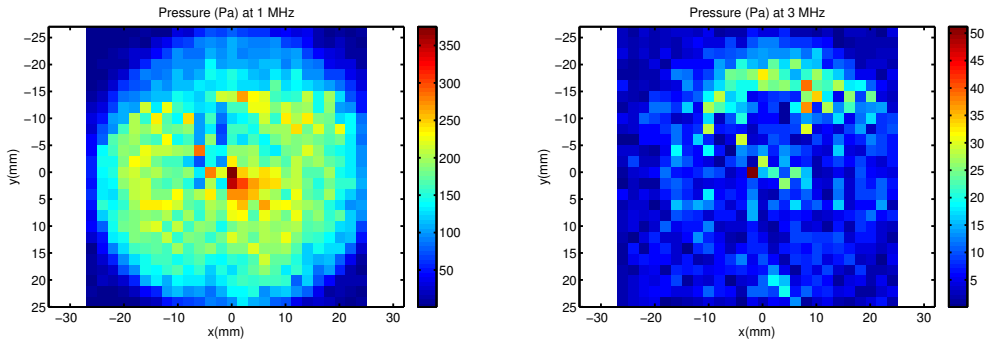

(a) (b)

Figure 3.5: This figure shows the spatial distribution of pressure at the fundamental frequency and third harmonic measured 5mm from the face of the 1MHz transducer using the FOH. There is a small region of the focus that produces a measurable third harmonic around 15% as large as the pressure at the fundamental. Averaged over the surface of the whole transducer the third harmonic is 5.6% of the input pressure.

the FOH, which does not suffer from electrical interference. The hydrophone scan of the face of the transducer shown in figure 3.5 showed that there was a third harmonic component present, although it was not uniform. It also shows that the pressure field at 1MHz is not uniform, confirming the theory that the transducer is not behaving as a perfect piston source.

A third harmonic was also added to the KZK simulation, and the results are shown in figure 3.6. Adding a third harmonic to the source pressure increases the third harmonic at the focus, and depending on the phase can increase or decrease the 2nd harmonic at the focus. A close match to the hydrophone measurements was found by varying the magnitude and the relative phase of the added third harmonic iteratively. Figure 3.6 shows the effect of changing the phase of the input third harmonic on the fundamental, second and third harmonics. The magnitude of the input third harmonic was chosen to be 8% of the input fundamental. This gave the best match between the simulation and the hydrophone measurements, although in the hydrophone scans of the face of the transducer in figure 3.5 the third har-

monic over the surface of the whole transducer is 5.6% of the input pressure.

For each separate input the in order to match the simulations the third harmonic component must be a different value- it is not constant nor does it increase linearly with input pressure. This, plus the fact that the transducer is not behaving like a perfect piston source, makes it difficult to find a set of inputs that can be used to model any input voltage to the 1MHz transducer.

3.3.4 3.3MHz Transducer

The final transducer investigated is a Precision Acoustics H102 HIFU transducer driven at its third harmonic (3.3MHz). It has the same dimensions as the 0.5MHz transducer used in section : 62.6mm focal length, 32mm aperture radius and a 12mm radius central hole. Figure 3.7 applies spatial averaging to PZFlex simulations to examine the importance of spatial averaging for each hydrophone used. This is done by spatially averaging the simulated values over a circular disc with the same radius as the active area of the each hydrophone. It shows that when measured with the PA needle hydrophone and FOH the effect of spatial averaging is negligible, but for the Onda hydrophone the measured pressures are significantly reduced.

Figure 3.8 shows plots of the first, second and third harmonic pressures generated by the H102 transducer at 3.3MHz in the transverse direction driven at 50mV (a),(c) and 100mV(b),(d) at the signal generator which corresponds to 28 and 56V at the matching network. The black lines show the hydrophone measurements, blue shows PZFlex simulation and red shows KZK simulation. (a) and (b) show the pressures measured by the PA needle and the FOH, (c) and (d) show the pressures measured by the Onda hydrophone. For these measurements the harmonics generated by the KZK method are higher than those generated by PZFlex, and appear to agree better with the FOH and PA needle hydrophone measurements, while PZFlex agrees

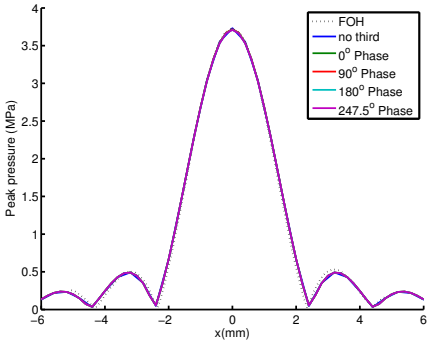

(a)

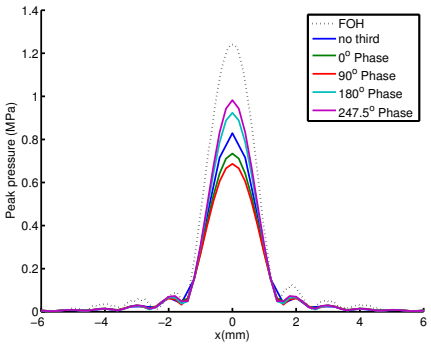

(b)

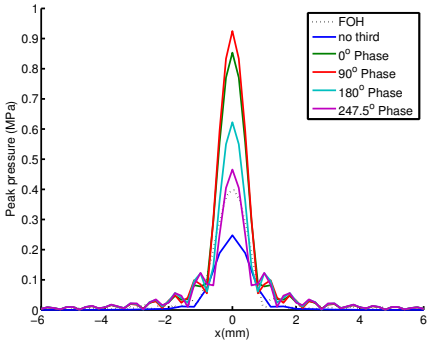

(c)

Figure 3.6: Plots of the first, second and third harmonics in the transverse direction. These plots show how adding a third harmonic to the source and subsequently changing the phase can increase or decrease the 2nd harmonic, and increase the third harmonic by different amounts according to the phase. The magnitude of the third harmonic was found by iteratively updating the phase and magnitude. The best match between the simulation and the measurement comes when the third harmonic input is 8% of the fundamental input, and the phase difference between the two is 247.5°.

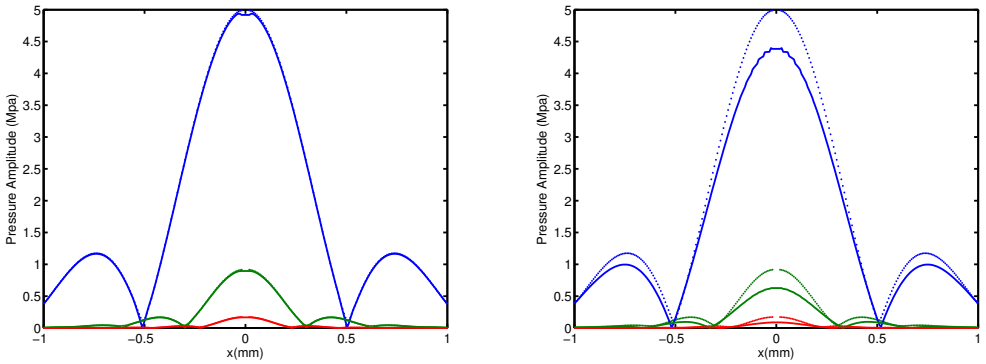

(a) (b)

Figure 3.7: This figure shows the effect of spatial averaging at 3.3MHz for the fundamental, second and third harmonics, by showing the results of the PZFlex simulation before and after spatial averaging is applied, at the length scale of (a) the PA needle hydrophone and the FOH and (b) the Onda hydrophone. The simulation before spatial averaging is shown in the dotted line and the averaged simulation is shown in the solid line. The smaller PA needle hydrophone and FOH values are unaffected by spatial averaging, while the Onda hydrophone is particularly affected.

better with the Onda hydrophone measurements.

3.4 Discussion

As frequency and pressure increases the KZK and PZFlex solutions show discrepancies, with the KZK predicting harmonics of higher amplitude than PZFlex. At 3.3MHz this difference is as large as 100% (figure 3.8). In this situation the KZK prediction agreed better with the PA needle hydrophone and FOH, while PZFlex agreed better with the Onda hydrophone. On balance, the measurements from the smaller hydrophones ought to be more accurate than the measurements from the Onda hydrophone, as the size of the focus at 3.3MHz is almost the same size as its tip.

One reason for the discrepancy could be the lower number of points per cycle used in the PZFlex solution. However, reducing the number of tau points in the KZK solution had little effect on the harmonics generated apart from a slight reduction

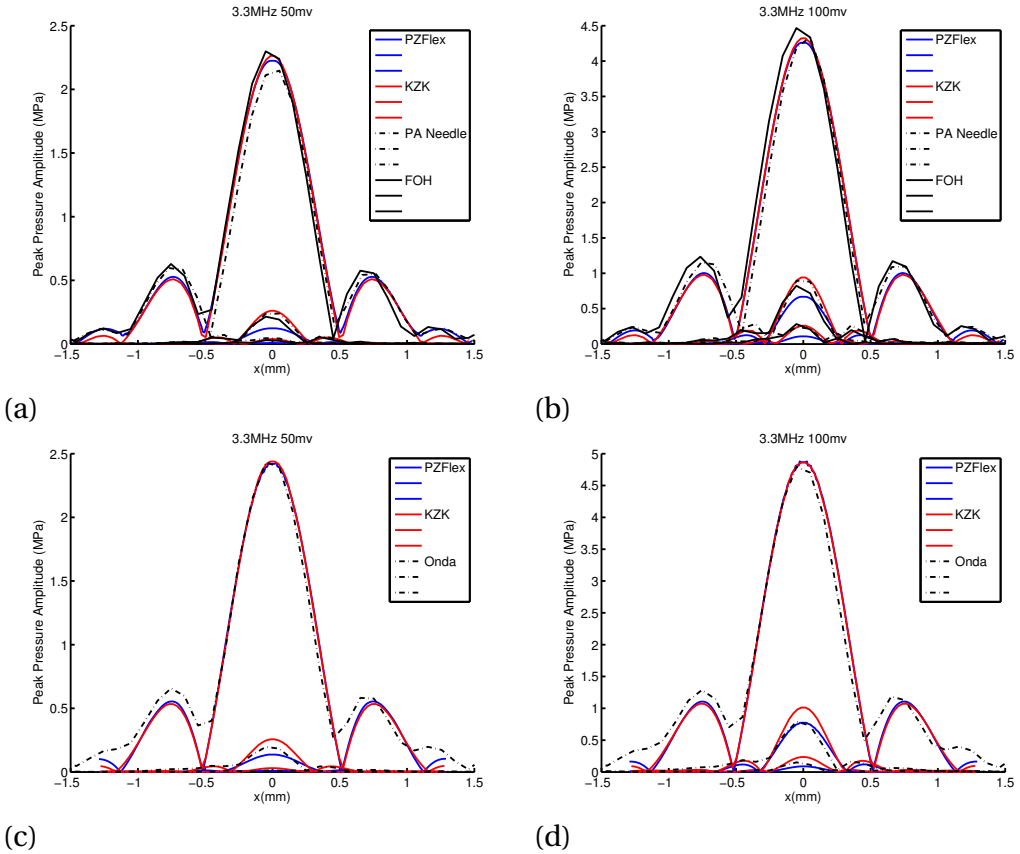

Figure 3.8: A plot of the first, second and third harmonic pressures generated by an H102 transducer at 3.3MHz in the transverse direction driven at 50mV (a),(c) and 100mV(b),(d) at the signal generator which corresponds to 28 and 56V at the matching network.. The black lines show the hydrophone measurements, blue shows PZFlex simulation and red shows KZK simulation. (a) and (b) show the pressures measured by the PA needle hydrophone and the FOH, (c) and (d) show the pressures measured by the Onda hydrophone. For the PA needle hydrophone and the FOH the spatial averaging effect is negligible. For the Onda hydrophone spatial averaging is very significant, and has been applied to both simulations. For these measurements the harmonics generated by the KZK method are higher than those generated by PZFlex, and appear to be in better agreement with the FOH and PA needle hydrophone measurements. PZFlex is in better agreement with better with the Onda hydrophone measurements.

at 3.3MHz, but this was small compared to the discrepancy between the two methods. Increasing the number of harmonics in the solution or reducing the number of radial points in the KZK simulation had little effect on the result suggesting the discrepancy is not sensitive to the numerical grid.

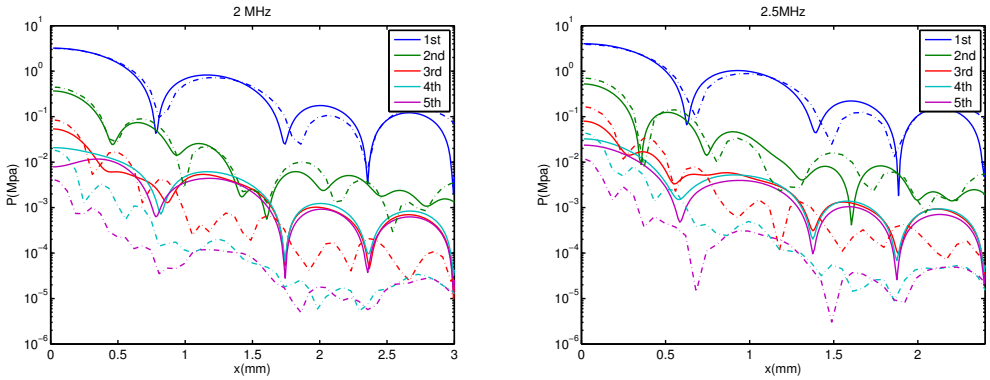

(a) (b)

Figure 3.9: A comparison of KZK and PZFlex simulations at 2 and 2.5MHz showing the first five harmonics in the transverse direction for each simulation. The KZK simulated harmonics are the dotted lines, and the PZFlex simulations are the plain solid lines. While the KZK harmonics grow around the focus in progressively tighter 'fingers' and reduce in magnitude with increasing harmonic number, the higher harmonics for PZFlex become the same magnitude and do not necessarily grow around the centre, instead following the shape of the fundamental frequency.

Additional simulations were calculated at input frequencies of 2 and 2.5 MHz at two different source pressures. The results for harmonics up to the fifth harmonic are shown in figure 3.9. Looking at the higher harmonics it becomes clear that there is an issue with the PZFlex simulations. At higher source frequencies the higher harmonics in the KZK solution grow around the focus, and each successive harmonic is roughly an order of magnitude lower. However, the 4th and 5th harmonics for the PZFlex solution are the same magnitude as each other, and are clearly the wrong shape. Rather than growing around the centre in increasingly tight 'fingers', PZFlex harmonics mirror the shape of the field at the fundamental frequency.

3.5 Conclusions

At frequencies below 1MHz and focal pressure amplitudes below 2MPa there was good agreement between KZK, PZFlex and hydrophone measurements. As the pressure and frequency increases, discrepancies appear between the two simulation

methods and measurements. For the hydrophone measurements this can be attributed to non-ideal source behaviour, and spatial averaging effects at high frequencies. KZK simulations agreed better with measurements from the smallest hydrophones. At higher frequencies and pressures the shapes of the harmonics generated by PZFlex appear to be incorrect. These results suggest that the KZK solution is better at simulating HIFU fields than PZFlex where nonlinearity is present above 1MHz, despite the fact that the KZK equation uses a paraxial approximation to account for diffraction.

CHAPTER 4

COMBINING PASSIVE ACOUSTIC MAPPING AND MR THERMOMETRY FOR MONITORING THERMAL ABLATION BY HIFU

4.1 INTRODUCTION

Chapter 2 showed that changes in B/A are unsuitable for monitoring thermal ablation, and 3 showed that there are challenges in modelling nonlinear ultrasound fields. Both of these results increase the need for more effective real-time treatment monitoring. In this chapter we describe the development of a combined apparatus that is capable of performing simultaneous passive acoustic mapping (PAM) and magnetic resonance (MR) thermometry. As discussed in section 1.3.2.1 MR thermometry is the current gold standard for monitoring thermal HIFU treatments, despite its high cost, and limited spatio-temporal resolution. In contrast, passive acoustic mapping (PAM) is a new method of monitoring the strength of acoustic

sources, especially cavitating bubbles, in real time during HIFU. It determines the strength and location of acoustic sources by using delay and sum beamforming techniques on acoustic emissions received passively on an ultrasound array. It is able to monitor ablation with low cost and very high temporal and spatial resolution (Jensen et al., 2012).

There are two main reasons for combining passive acoustic maps and MR thermometry. The first is that the combination of the two methods can give complementary information. MRI provides soft tissue localisation and high sensitivity temperature mapping, while ultrasound provides localisation of the focus early in the ultrasound exposure before any tissue damage occurs Jensen et al. (2012) as well as rapid spatiotemporal mapping of stable or inertial cavitation throughout the ultrasound exposurecavitation (Arvanitis and McDannold, 2011). In many HIFU applications cavitation has a purely mechanical role, such as drug delivery or blood brain barrier disruption (Arvanitis, Livingstone, and McDannold, 2013). This type of cavitation does not appear on MR images, but can be seen clearly on acoustic maps. While the outcome of these therapies can be monitored with MRI, cavitation mapping is the only way of providing real-time feedback about the process driving the treatment.

The second is that in thermal applications cavitation provides an extra source of heating that can be monitored by PAM. PAM-derived estimates of lesion size or cavitation-enhanced heating have the potential to replace or complement MR thermometry, but must first be validated against it. In Jensen et al. (2012) maps provided focus localisation and quantitative prediction of lesion occurrence beyond a certain threshold level and in Jensen, Cleveland, and Coussios (2013) a combined measurement and modelling approach shows that cavitation maps can be used to estimate temperature rise. In both of these scenarios PAM can compete with MR

thermometry on grounds of cost, spatial resolution and speed, but for a true assessment of PAM's monitoring potential require benchmarking against full MR temperature maps. Through combination of the two methods, feedback control of thermal ablation could be improved. The higher temporal resolution of cavitation-based feedback control (Hockham, Coussios, and Arora, 2010) combined with the accuracy of MR-thermometry based control (Bever et al., 2014) could lead to improved controllers. To achieve this, validation of the cavitation-based monitoring methods against MR methods is required.

Following the development of the combined PAM/MR thermometry system described in this chapter, chapter 5 compares PAM-derived estimates of temperature rise with MR thermometry measurements.

4.1.1 MR Imaging

4.1.1.1 The Magnetic Resonance Signal

In magnetic resonance imaging, the signal recorded is emitted by protons in a magnetic field precessing at their resonant frequency. The source of the protons in biological tissue is the nuclei of hydrogen atoms in water molecules. The precession frequency of the proton ω_p is known as the Larmor frequency and depends on the strength of the magnetic field, B_0, which is aligned along the bore of the MR coil, and the gyromagnetic ratio of the proton, γ.

$$\omega_p = \gamma B_0 \tag{4.1}$$

In order to produce a signal the protons are excited by the application of a magnetic field that rotates at the Larmor frequency perpendicular to the direction of B_0, this field is produced by what is known as the radio-frequency (RF) pulse. At

this frequency, protons absorb this energy, and once the oscillating field is removed the nuclei release or reradiate the energy as they return to their initial state. This re-radiation of energy by the nuclei as they return to their initial state is what is observed as the MRI signal. For a body with a spatial distribution of protons $\rho_p(x,y,z)$ the signal emitted from the body is

$$S(t) = \int\int\int \rho_p(x,y,z) e^{i\omega_p t} dxdydz \tag{4.2}$$

In order to encode spatial information in the signal gradients fields are applied that vary linearly in x,y and z. Firstly, to select a 2-D plane through the subject a magnetic field is applied that varies linearly in the 'z' direction. This changes the resonant frequency of the protons in the field, which becomes

$$\omega_p = \omega_{p0} + \Delta\omega_z = \gamma B_0 + \gamma G_z z \tag{4.3}$$

(Hinshaw and Lent, 1983). Applying an RF pulse at the resonant frequency multiplied with a sinc function excites only protons in a slice of thickness $\Delta z = \Delta\omega/\gamma G_z$, where $\Delta\omega$ is the width of the FT of the sinc function as shown in figure 4.1.

In order to encode the signal in the x direction, gradient fields in the x directions are applied, after slice selection, while the signal is being emitted. The protons in the subject now oscillate at frequencies that depend on their location- $\omega_p = \gamma B_0 + \gamma G_x x$ (Hinshaw and Lent, 1983). In order to encode the y direction a gradient $G_y y$ is applied after the slice select gradient is applied before the x direction gradient for a short time $d\tau$, which adds a phase offset $\gamma G_y y d\tau$. The gradient in the x direction is known as the frequency-encoding gradient and the gradient in the y direction is known as the phase encoding gradient. Combining signals with multiple phase

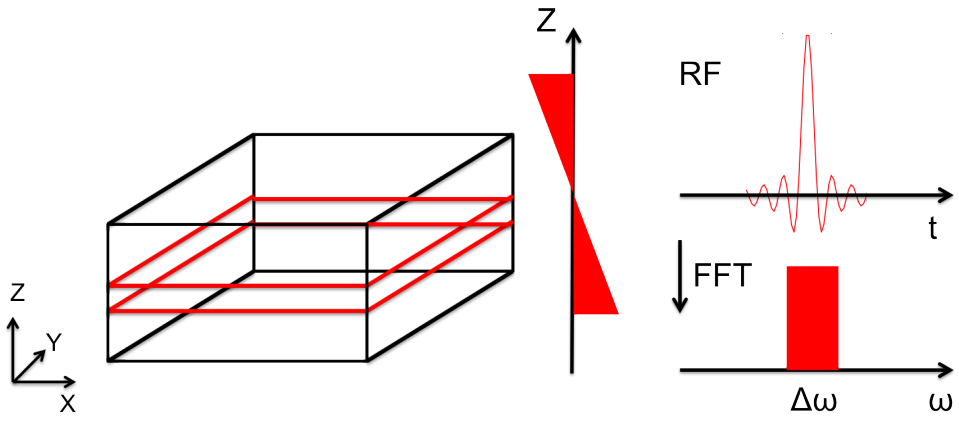

Figure 4.1: In order to select a 2-D slice through the subject a linear gradient is applied in the z direction. This changes the resonant frequency of the protons in the subject $\omega_p = \gamma B_0 + \gamma G_z z$. Applying an RF pulse at the resonant frequency multiplied with a sinc function excites only protons in a slice of thickness $\Delta z = \Delta\omega/\gamma G_z$, where $\Delta\omega$ is the width of the FT of the sinc function.

offsets, the signal received from a slice in the z direction now becomes (Brown et al., 2014).

$$S(k_x, k_y) = \int\int \rho_p(x, y) e^{ik_x x + ik_y y} dx dy \tag{4.4}$$

where the oscillation at ω_p is ignored, $k_x = \gamma G_x t$ and $k_y = \gamma G_y \tau$.

To recover the image, $\rho(x, y)$ from the signal $S(k_x = \gamma G_x t, k_y = \gamma G_y \tau)$, the 2-D inverse Fourier transform of the signal is taken. In this case

$$\rho(x, y) = FT^{-1}[S(k_x, k_y)] = \frac{1}{(2\pi)^2} \int\int S(k_x, k_y) e^{(-ik_x x - ik_y y)} dk_x dk_y \tag{4.5}$$

4.1.2 MR Thermometry

As discussed in section 1.3.2.1 the most commonly used method for MR thermometry is the proton resonance frequency (PRF) method, creating phase maps where

the change in phase is proportional to the change in temperature. It has become the preferred method due to its excellent linearity and its independence to tissue type (Rieke and Butts Pauly, 2008). Sekihara, Matsui, and Kohno (1985) shows that any inhomogeneity in a magnetic field can be visualised by looking at the phase of the MRI image, as inhomogeneities change the resonant frequency of the protons. In the commonly used echo-planar sequence, the signal in an inhomogeneous field is

$$S(t,\tau) = \int\int \rho_p(x,y) e^{i\omega_0 t + i\gamma G_x t x + i\gamma G_y \tau y + i\gamma \Delta B_0 TE} dxdy \tag{4.6}$$

where TE is the effective echo time (a parameter related to the timing of phase-encoding gradients), and $\Delta B_0(x,y)$ is the variation in the magnetic field. After inverse Fourier transforms, the resulting image obtained is

$$s(x,y) = \rho_p(x,y) e^{i\gamma \Delta B_0 TE} \tag{4.7}$$

and so taking an image of the phase gives an image of the inhomogeneity.

Ishihara et al. (1995) notes that as well as being a function of x and y, the inhomogeneity is also a function of temperature. Looking at the relative phase Φ between two images, one at a reference temperature and one with a temperature change gives the following result.

$$\Delta\Phi(x,y,T) = \Phi(x,y,T) - \Phi(x,y,T_{ref}) = \gamma \Delta B_T(\Delta T) TE \tag{4.8}$$

The relative phase image therefore depends only on the relationship between a change in temperature and a change in the magnetic field, the function $\Delta B_T(T)$. This change is due to the way that proton shielding changes with temperature. In

water molecules hydrogen nuclei are shielded from the magnetic field by the electrons in the molecule. Hydrogen bonds between molecules reduce this shielding. As the temperature increases, the water molecules on average spend less time in a hydrogen bonded state, and the degree of shielding increases. This has the same effect as locally decreasing the magnetic field. This change in local magnetic field is linear, and proportional to the constant magnetic field B_0. It is written as

$$\Delta B_T(T) = B_0 \alpha \Delta T \tag{4.9}$$

where α is the temperature-dependent proton resonant frequency change coefficient (Rieke and Butts Pauly, 2008) which for water molecules is $-1.03 \pm 0.02 \times 10^{-8}/°C$. Putting this back into the equation for phase change and rearranging, we see that the relative temperature change between two 2-D images is given by

$$\Delta T(x,y) = \frac{\Phi(T) - \Phi(T_{ref})}{\alpha \gamma T_E B_0} \tag{4.10}$$

4.1.3 Passive Acoustic Mapping

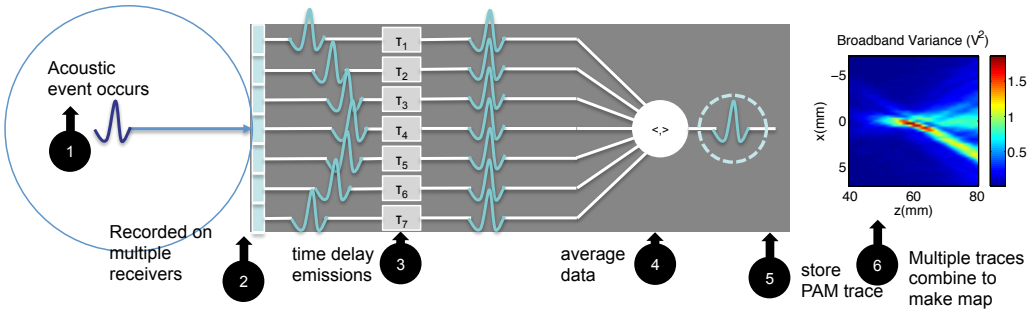

Figure 4.2: An outline of the Passive Acoustic Mapping Algorithm: An acoustic event occurs and is passively recorded on a multi-element array. A beamforming algorithm is then applied to determine the strength of the sources at a certain location. The summed rf traces are then analysed in the frequency spectrum and combined to create spatial maps of bubble activity.

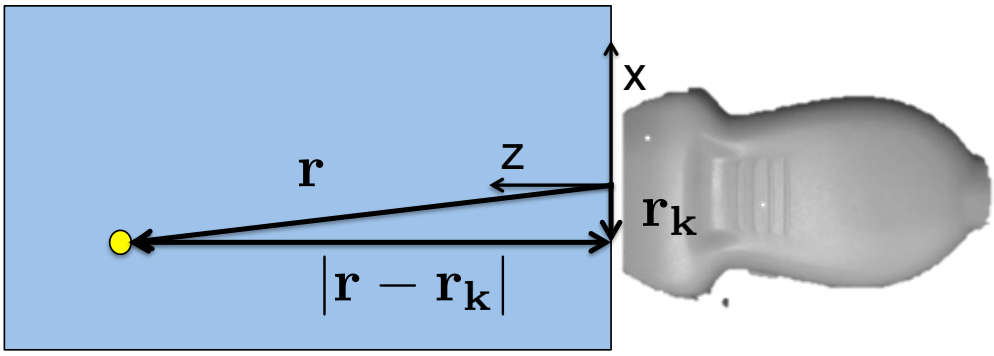

Figure 4.3: The co-ordinate system used for processing passive acoustic maps: An acoustic event occurs at position $\mathbf{r}$ and is passively recorded on a multi-element array with k elements each at position $\mathbf{r_k}$.

In passive acoustic mapping (PAM) voltage traces are recorded on a multi-element diagnostic ultrasound array. Delay-and-sum beam-forming techniques are applied to determine emissions from a certain location. It is based on the idea that an acoustic point source such as a bubble centred at position $\mathbf{r}$ with strength $q(\mathbf{r}, t)$ results in a pressure at point $\mathbf{r}'$ of

$$p(r', t) = \frac{q(t - |\mathbf{r}' - \mathbf{r}|/c)}{4\pi|\mathbf{r}' - \mathbf{r}|} \tag{4.11}$$

where c is the speed of sound. With an array of calibrated acoustic sensors at positions $\mathbf{r_1} \ldots \mathbf{r_N}$ the estimated source strength $\tilde{q}$ and acoustic power $\tilde{P}$ are given by

$$\tilde{q}(r, t) = \frac{1}{N} \sum_{i=1}^{N} 4\pi|\mathbf{r}_i - \mathbf{r}|\tilde{p}(\mathbf{r}_i, t + |\mathbf{r}_i - \mathbf{r}|/c) \tag{4.12}$$

$$\tilde{P}(r, t) = \frac{\langle \tilde{q}^2(r, t) \rangle}{4\pi\rho c} \tag{4.13}$$

where $\tilde{p}(\mathbf{r_i}, t)$ is the pressure recorded on sensor i and $\langle . \rangle$ is the average operator (Gyöngy and Coussios, 2010).

The following process converts the 64 voltage traces recorded on the diagnostic ultrasound into passive acoustic maps (Gyöngy and Coussios, 2010). Traces are taken 25 times a second and each trace lasts for 138μs. The co-ordinate system used is shown in figure 4.3. $v_k(t)$ is the voltage trace recorded on channel k of the imaging transducer. This is converted to pressure by taking the Fourier transform of the voltage trace and dividing by the sensitivity $s(\omega)$ of the transducer at each frequency. In this chapter, a nominal sensitivity of 1mV/Pa is used, in chapter 5 the measured frequency dependent calibration is applied.

$$P_k(\omega) = V_k(\omega)/s(\omega) \tag{4.14}$$

To find the source strength q' at position $\mathbf{r}$, first the pressure on each channel is delayed and spherical spreading is accounted for, giving q'_k.

$$q'_k(\mathbf{r},t) = 4\pi|\mathbf{r}-\mathbf{r_k}|p_k(t+|\mathbf{r}-\mathbf{r_k}|/c) \tag{4.15}$$

At this stage two methods can be used for the delay-and-sum beamforming, time exposure acoustics (TEA) (Gyongy and Coussios, 2010) and robust Capon beamforming (RCB) (Coviello, Faragher, and Coussios, 2010). In time exposure acoustics the delayed q'_k are simply averaged, and assumed to sum coherently

$$q'_{tea}(\mathbf{r},t) = \sum_{k=1}^{N} q'_k(\mathbf{r},t)/N \tag{4.16}$$

The robust capon beamformer method the sum has weights w_k attached that reduce artefacts. The weights are calculated using an optimisation technique that is designed to pass any signals arriving from a specified look direction undisturbed

while minimising the array output power so as to limit interfering signals not from the look direction (Coviello et al., 2013)

$$q'_{rcb}(\mathbf{r},t) = \sum_{k=1}^{N} w_k(|\mathbf{r}-\mathbf{r_k}|)\, q'_k(\mathbf{r},t)/N \tag{4.17}$$

In analysing cavitation it is useful to separate broadband noise from harmonics emissions. This is especially true in these experiments as harmonic signals from the incident HIFU mix with harmonic signals from bubbles. This separation is performed using a comb filter in the frequency domain. The comb filter separates broadband harmonic emissions by setting all of the signal within a band of 0.3MHz centred around each harmonic to zero for broad band emissions, and everything outside the band to zero for harmonic emissions. While in the frequency domain the pressure is then turned into a source power W by summing Q'_m, the DFT components of q'_{rcb}, to get

$$W(\mathbf{r}) = \frac{\sum_{m}^{N_{DFT}} {Q'_m}^2(\mathbf{r})}{4\pi\rho c N_{DFT}} \tag{4.18}$$

As the signal has zero mean, the power (the mean of squares) is the same as the variance of the signal (mean of squares - square of means). Passive maps are commonly described as having units of 'variance'. The comb filtering creates two PAM frames- one 'harmonic' map and one 'broadband' map.

4.2 METHODS

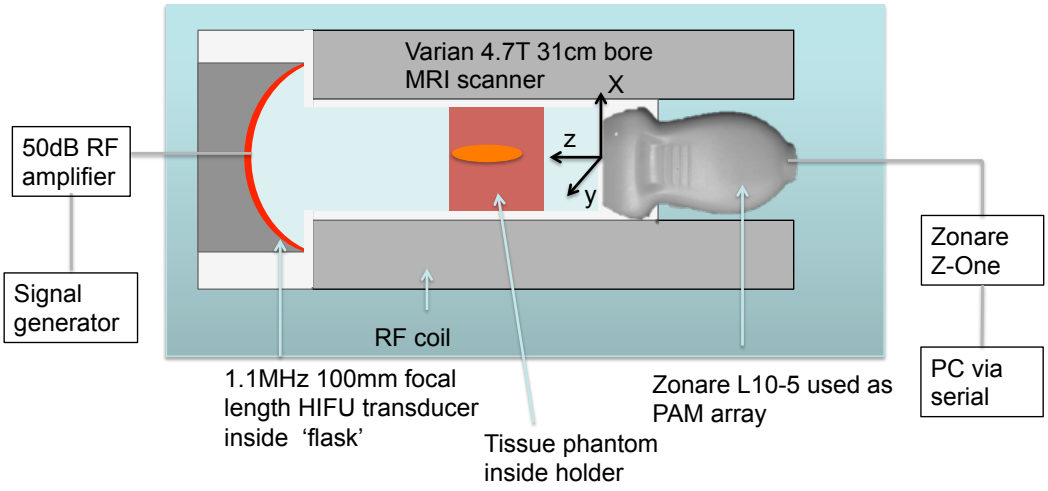

Figure 4.4: The combined PAM/MR Thermometry experimental apparatus, shown in cross section. The apparatus is essentially a sealed cylinder that is placed inside an MRI bore. The cylinder is filled with degassed water, with a tissue holder containing a sample of liver in the centre. One end of the holder has a mylar window to allow acoustic access for the Zonare ultrasound array. The other end is sealed by the HIFU transducer built into the assembly.

4.2.1 Combined Transducer and Sample Holder

In the basic ex vivo ablation experiment ex-vivo bovine liver at 37 °C was exposed to HIFU. In this case the HIFU transducer was a spherically focussed transducer (Channel Industries, Santa Barbara, CA USA) with a geometric focus of 98mm, and an effective aperture radius of 32mm. It had a resonant frequency of 1.125MHz and could provide pressures up to 12MPa peak to peak. It was driven by a signal generator (33220A, Agilent Technologies, Santa Clara, CA) connected to a 50dB broadband amplifier (1140LA, E&I, Rochester, NY, USA).

For passive acoustic mapping a Zonare Z-one imaging system (Zonare, Mountain View, CA) with a L10-5 probe attached was used. The settings on the Zonare and signal generator were sent via a serial connection, and cavitation traces were saved to disk for later analysis. The Zonare provides a trigger out signal which controlled the timing of the HIFU bursts from the signal generator.

For these experiments the MR scanner used was a Varian 4.7T small animal scanner. This had a bore diameter of 62mm and a length of 1.5m. For this reason the experimental apparatus had to be modified from the standard setup where sample, and therapy and imaging transducers are placed inside a water tank. Instead, all three had to fit inside the MRI bore. The experimental setup is shown in figure 4.4. The apparatus is essentially a sealed cylinder that is placed inside the MRI bore. The cylinder is filled with degassed water, with a tissue holder containing a sample of liver in the centre. One end of the holder has a mylar window to allow acoustic access for the Zonare ultrasound array. The other end is sealed by the HIFU transducer built into the assembly.

4.2.2 Passive Acoustic Mapping

In conventional passive mapping experiments the imaging transducer is either place inside, to the side of, or perpendicular to the HIFU transducer. Due to the space constraints of the experiment it was necessary to place the Zonare transducer facing the HIFU transducer, meaning that the PAM array is directly insonified by the HIFU beam. Preliminary experiments showed that harmonics of significant amplitude are indeed present in the passive map in the absence of cavitation due to the incident pressure from the HIFU transducer, although these harmonics are reduced by the presence of cavitating bubbles, as seen in 4.5, meaning that the harmonic part of the signal was not used to analyse cavitation. However, broadband noise on the maps was consistent with the presence of broadband noise on a perpendicularly aligned passive cavitation detector transducer. That is, even in this configuration the array is able to detect broadband emissions associated with cavitation.

The Zonare recorded pulses 138μs seconds long at a sampling frequency of 50MHz. These pulses were repeated at a frame rate of up to 25Hz for exposures up

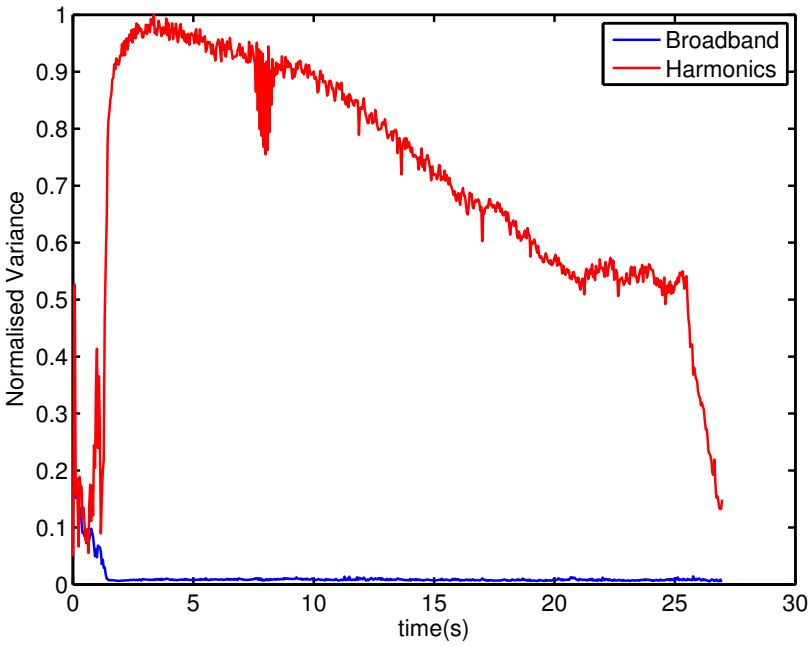

Figure 4.5: This figure shows broadband and harmonic variance over time, normalised to the maximum value of harmonic variance. In this exposure, there is a burst of broadband variance in the first 1.5s. During this time the harmonic signal drops, and then recovers. This is due to the bubbles reflecting the incident harmonics. Once the initial cavitation dies away, the harmonics still decrease. This could be due to the increase in cavitation as the tissue denatures, or to the presence of off-resonance bubbles that shield the incident HIFU but do not emit broadband noise.

to 27s long on a linear probe 5cm wide with 128 elements. The probe was sensitive between frequencies of 5 and 8MHz.

4.2.3 MR Thermometry

The sequence used for MR thermometry was a gradient-echo echo-planar-imaging sequence with a repetition time TR = 320ms and an echo time TE = 15ms. In the x, y and z directions the voxel size was $0.9 \times 0.9 \times 2$mm respectively, and temperature was recorded over a grid of $64 \times 64 \times 12$ voxels. As two complete sequences were taken to create a single image the effective temporal resolution of the sequence is 640ms.

4.2.3.1 Conversion from Phase to Temperature

Although the relationship between phase and temperature is given in equation 4.10 there are two further steps to extract accurate temperature information from phase images. The first is to remove background phase drift, where the phase gradually changes over time without any change in temperature. Fortunately, this change is linear with time, and constant over the volume of the sample. This is removed by fitting a straight line to the average phase change over time for a selection of voxels outside the heated region.

The second is to unwrap the phase signal, that is, to remove the discontinuities caused by the wrap-around in phase from π to $-\pi$ as the temperature increases and vice versa. The temporal unwrapping algorithm looks at the difference between voxels over time, and any time a jump in phase greater than π is recorded 2π is added to or subtracted from the rest of the signal depending on whether the change was an increase or a decrease. This process is shown in figure 4.6.

4.2.4 Preparation of Liver Samples

Fresh ex-vivo bovine liver was obtained on the day of slaughter from an abattoir (Mutchmeats, Witney, Oxfordshire) and prepared on the day of slaughter. After cutting into 10x10x5cm sections the samples were refrigerated overnight. On the morning of the experiment the day after slaughter they were cut to fit the cylindrical sample holders (4cm diameter, 5cm depth) and degassed in 10% phosphate buffered saline solution (Fisher Scientific Watham, MA, USA) at -0.9 bar in a vacuum chamber attached to a vacuum pump for 1 hour. The samples were sealed while fully submerged and kept at room temperature. Thirty minutes before use they were placed in a water bath at 37 °C to bring them up to temperature, which was followed by 5 minutes to set up and record pre-treatment images before the HIFU was turned on.

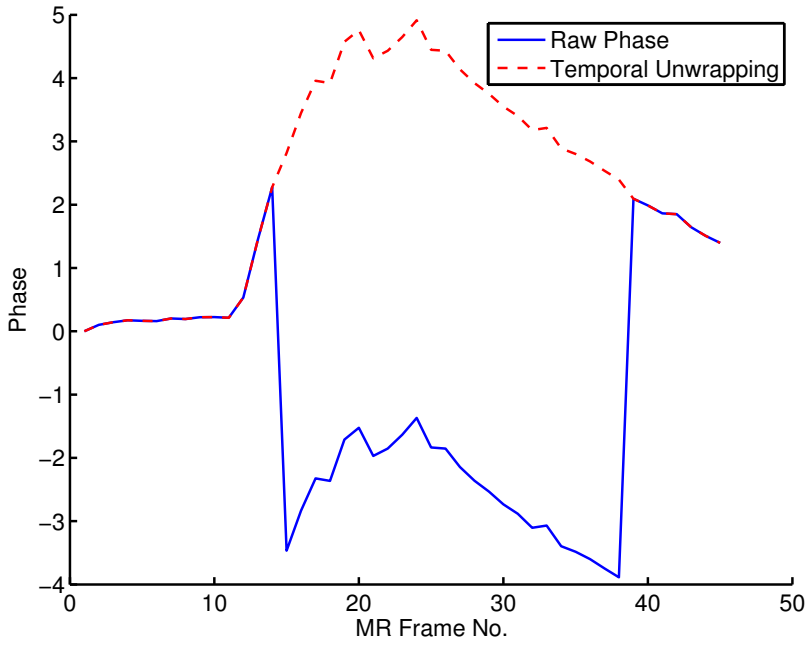

Figure 4.6: The effect of phase unwrapping. The blue line shows the raw phase for a voxel in the MR image during heating and cooling. The red line shows the same trace with the phase unwrapped.

By this point the temperature at the centre of the tissue was calculated to be less than 0.35°C below the ambient temperature of the water. While fully submerged in the water bath the sample was sealed inside the transducer assembly, and then immediately placed inside the MRI bore for HIFU exposure.

4.2.5 Cavitation Nuclei

It is necessary to degas abattoir liver tissue in order to remove large bubbles introduced by the retrieval process and to avoid large variability in cavitation threshold from one tissue to the next. Recent work in the laboratory has demonstrated that non-perfused liver tissue has a comparable cavitation threshold to perfused tissue in terms of the negative pressure required to produce cavitation, but that the probability of cavitation at a given pressure is substantially lowered by the absence of

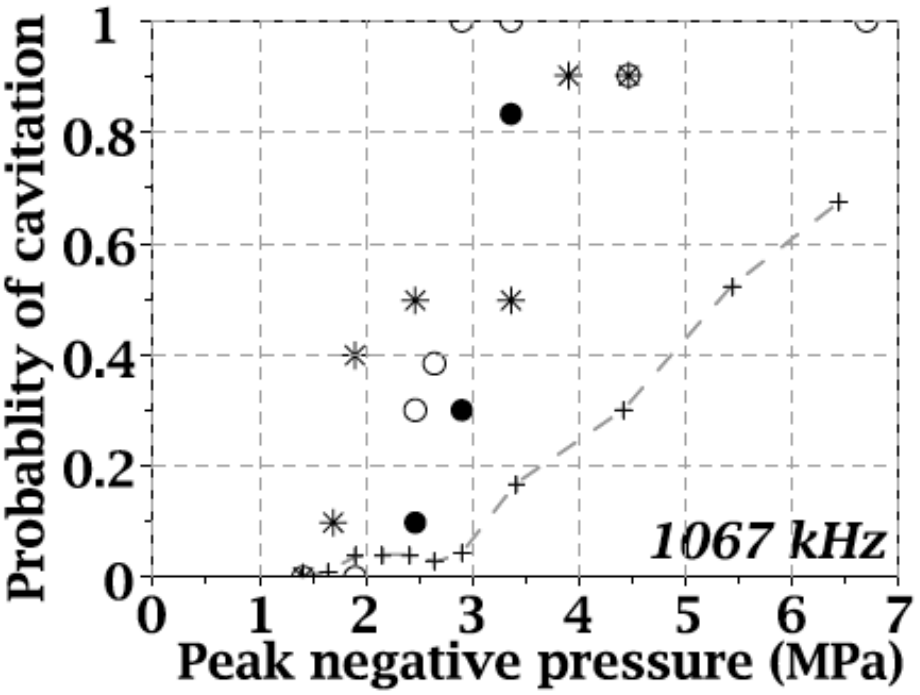

Figure 4.7: This figure shows the probability of cavitation occurring in perfused and non-perfused tissue at 1.067MHz. The crosses connected to the trendline show the probabilities for non-perfused ex-vivo liver tissue and the individual points show cavitation probabilities in different samples of perfused liver. In the range -4 to-6MPa a probability of cavitation of 100% is reached in perfused tissue, while the probability of cavitation in non-perfused tissuevaries from 25-60%. (Figure courtesy Dr. Stephane Labouret)

perfusion. As shown in figure 4.7, at 1 MHz in perfused tissue, a probability of cavitation of 100% is reached in the range -4 to -6 MPa. In order to enable reproducible cavitation behaviour in non-perfused abattoir tissue, exogenous cavitation nuclei were introduced.

The type of exogenous nuclei used in these experiments have also been developed recently in the laboratory, and consist of nano-sized particles that entrap and stabilise gas on their surface to dramatically lower the inertial cavitation threshold (Kwan et al., in press). They consist of a polystyrene template nanoparticle with a predominantly poly-methyl methacrylate coating. The coating causes swelling of the polystyrene template allowing for a void to form in the centre of the nanoparti-

cle which subsequently deforms and creates the cup shaped depression on the surface. This depression enables entrapment and stabilisation of gas after air drying the nanocups and re-suspension in water.

They were chosen because they do not interfere with MR imaging and provide sustained cavitation activity upon prolonged exposure. Most importantly, they yield sustained cavitation activity at a pressure of -6 MPa at 1 MHz in non-perfused liver tissue, which makes it consistent with observations in perfused liver tissue. As shown in figure 4.8 at a pressure of −6MPa cavitation occurs but only when nuclei are added. Having cavitation occur in the same pressure range ex vivo and in vivo is important, in order to ensure that the relative magnitude of effects due to non-linear propagation and cavitation is adequately represented.

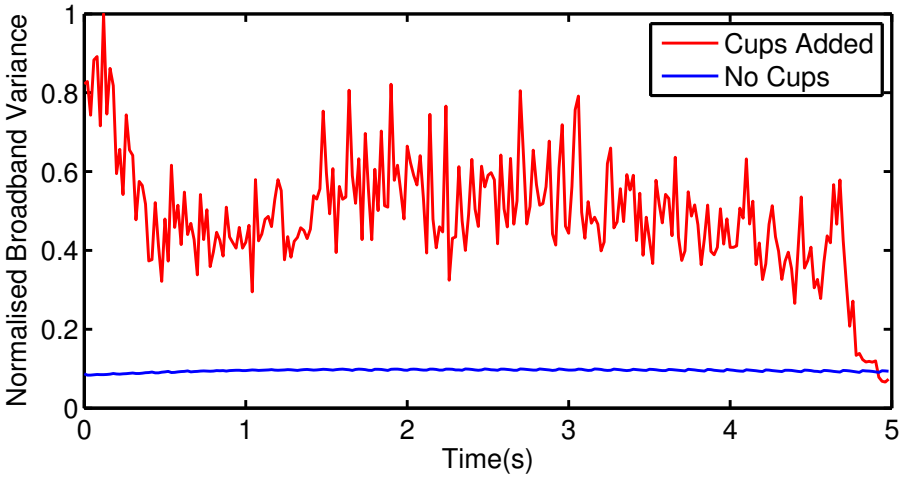

Figure 4.8: The graph shows the maximum broadband variance over time for ex-vivo liver with and without the addition of cavitation nuclei. Both exposures are 1MHz bursts 5000 cycles long at a pulse repetition frequency of 50Hz. The peak negative focal pressure is -6MPa. Without cups cavitation does not occur, whereas with cups added it is possible to achieve sustained inertial cavitation.

4.2.6 Lesion Imaging

Before and after each exposure the tissue was imaged using a high resolution ge3d (3-Dimensional Gradient Echo) sequence to determine whether a lesion had formed. Using this sequence lesions appeared as a hyperintense region on the images and corresponded well to visual assessment of lesions when samples were sliced open post exposure. To improve the lesion identification the pre-exposure image was subtracted from the post-exposure image before Wiener filtering to remove noise.

Post-exposure all the samples were sliced through the central plane and photographed with a ruler in shot for scale for analysing lesion size. As the appearance of the injected polymeric nano-cups closely resembled a small, fragmented lesion, in these cases the sliced tissue was also palpated to test the stiffness of the lesion. The size of the lesions such as the one seen in figure 4.9 agree with visual observations of lesion size.

4.2.7 Image registration

The Zonare array can image a 2-D plane within the 3-D image of the phantom which necessitates image registration between the two modalities. This requires an imaging phantom with fiducial markers visible to ultrasound and MRI. For this purpose a 5% weight/volume agar phantom was made with 3mm diameter acrylic ball bearings set into a particular pattern in a plane through the middle of the phantom. Images were registered by comparing magnitude EPI (echo-planar imaging) and ge3d images with B-mode ultrasound images.

4.3 RESULTS

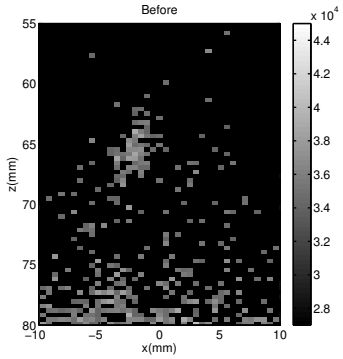

(a)

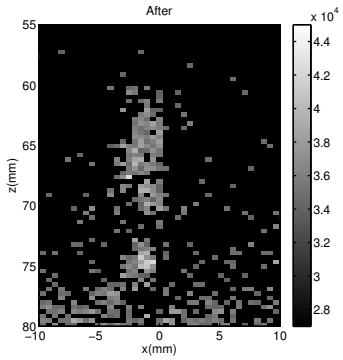

(b)

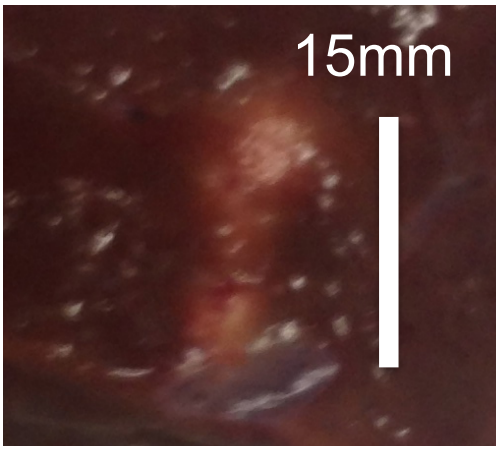

(c)

Figure 4.9: (a)(b)The two ge3d (3-D gradient echo) images show the same piece of tissue before and after HIFU treatment after the tissue has cooled. The cavitation nuclei are visible as a hyperintense region ins the upper image. After treatment the lesion is seen as an additional hyperintense region in the centre of the lower image. (c) A photograph of the lesion showing the cups and the surrounding lesion.

4.3.1 MR-Ultrasound Compatibility

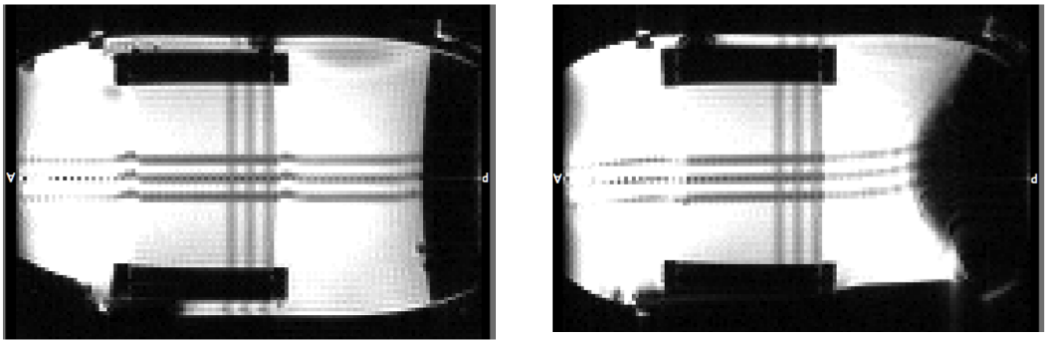

Figure 4.10: The effect of the imaging transducer on MRI images is shown in a pilot image. Each image shows a cross section of the combined MR-HIFU apparatus with a tissue holder in the centre containing a gel phantom. The gray lines indicate the direction of the magnetic field lines. There is no transducer in the left hand image and the darker lines through the phantom in the centre are straight. When an imaging transducer is added in the right hand image the lines are bent as the transducer disturbs the magnetic field, and there is a dark region close to the transducer. It is still possible to create a uniform, undisturbed field inside the region of interest by changing the shim settings of the scanner.

It has been shown that while ultrasound systems can be integrated into MR scanners (Feinberg et al., 2010), (Tang et al., 2008) , there is interference between the two systems that must be characterised. The presence of the therapeutic transducer had no effect on MR images, but the imaging transducer did create interference. The transducer head contains ferrous materials that distorted the magnetic field, and created a 'shadow' that is visible on the right of the right hand image in figure 4.10. It also distorted the magnetic field lines, shown by the curvature of the horizontal lines in the figure. Despite this, imaging was still possible as the sample was far enough away from the 'shadowed' area and the field lines within the sample were made uniform by correctly changing the shim settings of the MR scanner. The electrical pulses generated when the transducer is capturing B-mode images interfered with the MR images as shown in figure 4.11. While these could be mitigated by shielding the transducer as in (Feinberg et al., 2010) in our case images

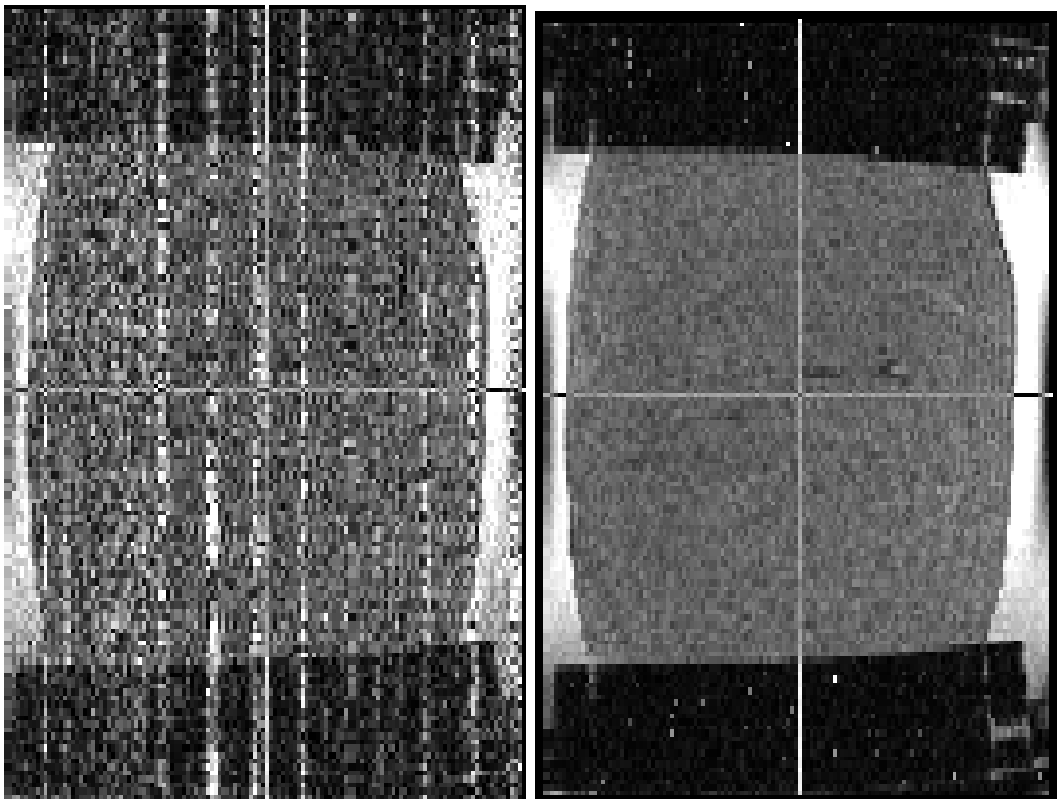

(a) (b)

Figure 4.11: Two ge3d images showing the effect of active ultrasound on MR images. Both images show a cross section of the liver sample (grey) with the plastic holder (in black above and below) and water (bright areas to the left and right). In the image on the left the ultrasound transducer is in B-mode, while on the right it has been placed into passive mode. Electrical noise from the B-mode pulses add noise to the image that disappears in passive mode. This does not pose a problem as the transducer is in passive mode for all MR Thermometry measurements. The noise in passive mode is the same as the noise with the imaging transducer turned off.

are only recorded passively while MRI scans are in progress, and created no extra noise. There were no detectable disturbances in either B-mode images or passive maps when the ultrasound scanner is placed inside the MR bore and MR scans are in progress.

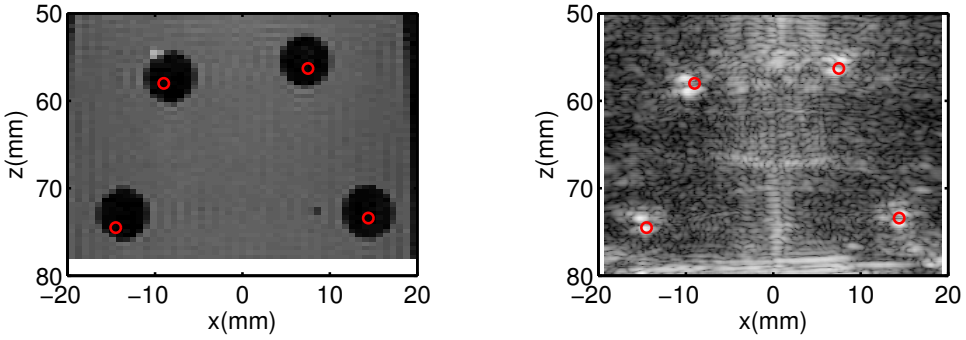

(a) (b)

Figure 4.12: MR and ultrasound images of the registration phantom. Both show the plastic balls set inside the phantom in a common co-ordinate frame where z is the axial distance from the imaging transducer and x is the radial distance from the centre of the transducer in the plane parallel to the transducer. The red circles show the locations of the fiducial markers in each image.

4.3.2 Image registration

Figure 4.12 shows MR and ultrasound images of the registration phantom taken with GE3d MR and B-mode ultrasound. Both show the plastic balls set inside the phantom in a common co-ordinate frame. In this chapter, z is the axial distance from the imaging transducer, x and y are the radial directions from the centre of the imaging transducer parallel and perpendicular to the linear array respectively. the HIFU focus is around 3cm long and 5mm wide.

4.3.3 Combined PAM and MR Thermometry Monitoring

At low HIFU pressures no cavitation is observed. Instead, as shown in figure 4.13 the harmonic section of the passive map shows the location of the harmonics generated at the HIFU focus. Even though the map uses broadband energy, a small portion of the harmonic energy passes through the comb filtering process and is present in the broadband map. The location of the focus in the harmonic and broadband maps occurs at the same location as the centre of heating in MRI images, validating the image registration.

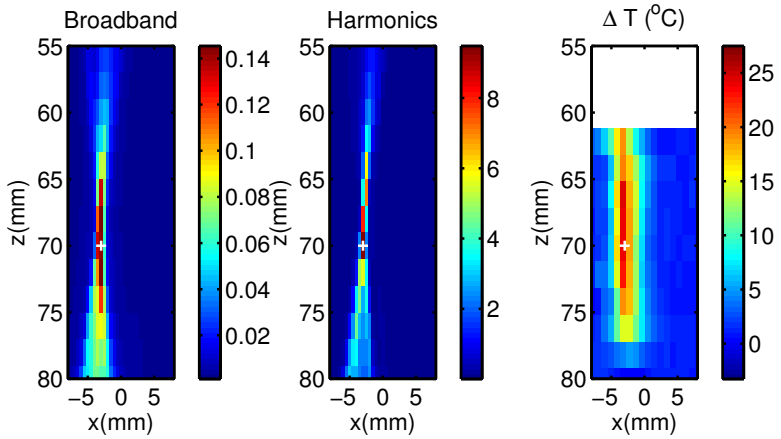

Figure 4.13: This figure shows (a) a broadband passive map (b) a harmonic map and (c) simultaneously acquired MR thermometry temperature image, at a peak negative focal pressure of 2.75MPa in the co-ordinate frames found by registering the images in figure 4.12. At at low pressure magnitudes below the cavitation threshold no cavitation is present and the only energy in the maps is a small portion of the harmonics signal that leaks through into the broadband map at the location of the focus. When seen side by side the position of the focus in the passive map is the same as the location of maximum heating in the MR thermometry.

4.3.3.1 Cavitation in PAM and MR Images

As shown in figures 4.14 and 4.15 short, non-thermal pulses at pressures below and above the cavitation threshold were investigated to determine whether cavitation that was visible on passive maps is visible in MR images. Above the cavitation threshold there is a large increase in the broadband signal in passive maps. Although cavitation produced a clearly visible difference in passive maps at 6MPa peak negative focal pressure, short exposures at the same pressure in gel phantoms with cavitation nuclei added produced no change in MR images. This is to be expected, as the probable size and number of bubbles appearing in these conditions will cause a tiny change in the proportion of liquid present in a single voxel. Much larger amounts of cavitation have been visualised with MRI but this is with much higher pressures and much larger clouds of bubbles, where it is possible to see the movement of water due to the action of the bubbles (Allen et al., 2015).

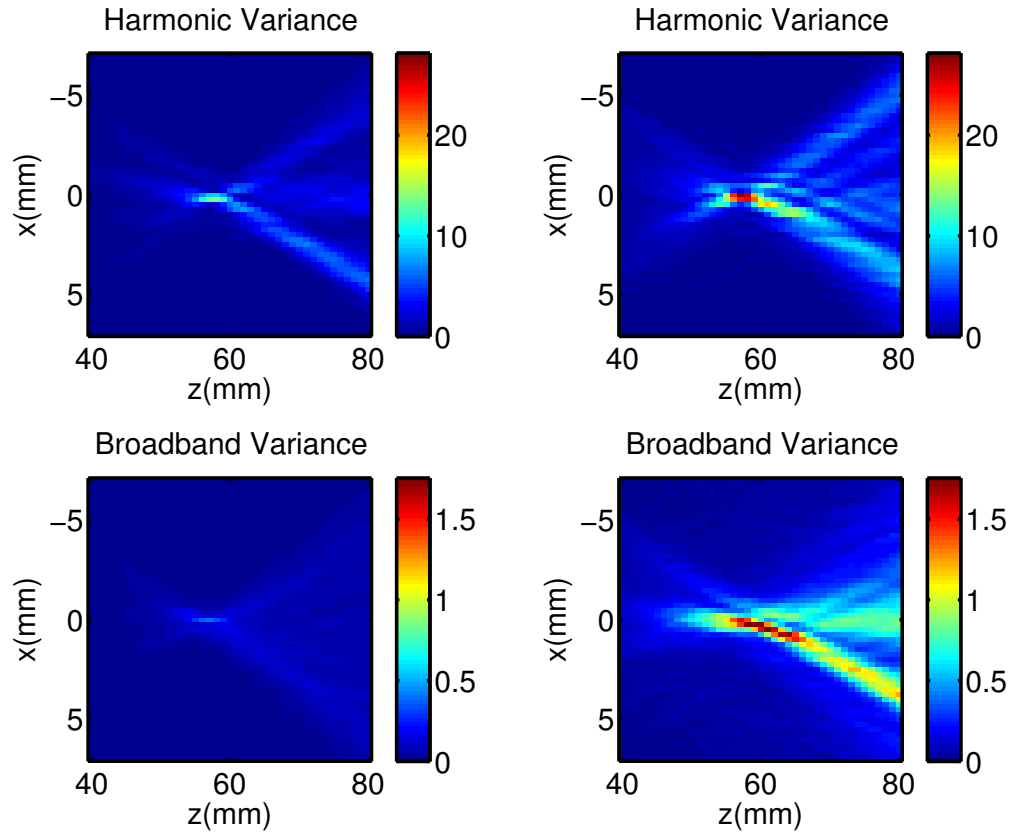

(a) (b)

Figure 4.14: This figure shows passive maps of harmonic and broadband variance for short, non-thermal HIFU pulses (a) below and (b) above the cavitation threshold at peak negative focal pressures of 2.75 and 6MPa respectively and a frequency of 1MHz. As the pressure crosses the cavitation threshold there is a modest increase in the harmonic component of the map, and a large increase in the broadband signal, typical of cavitation.

4.3.3.2 Heating

4.3.3.3 Cavitation-Enhanced Heating

In the absence of significant broadband noise on passive maps the heating/cooling curve measured by MR thermometry increases smoothly and it is shown in section 5.3.1 that these curves match thermal simulations of HIFU heating. When cavitation is present there can be a simultaneous 'spike' in the MR temperature data that coincides temporally with cavitation in passive acoustic maps. An example of this

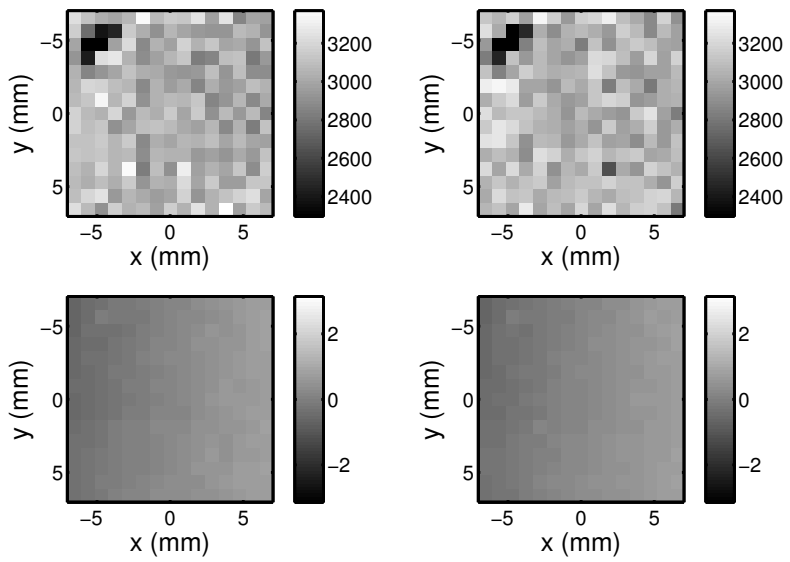

Figure 4.15: This figure shows (top) magnitude and (bottom) phase images taken with an EPI sequence for short non-thermal HIFU pulses (left) below and (right) above the cavitation threshold at peak negative focal pressures of 2.75 and 6MPa respectively and a frequency of 1MHz. As the pressure crosses the cavitation threshold there is no significant change in either the magnitude or phase of the MRI images.

is shown in figure 4.17.

The spatial extent of cavitation-enhanced heating in MR thermometry data is obtained by subtracting the expected primary HIFU heating from the total heating measured in MRI. This is explained fully in chapter 5. The location of enhanced temperature rise and the location of broadband noise in passive maps is shown in figure 4.18. In this figure the PAM data has been processed using both algorithms mentioned in section 4.1.2, time-exposure acoustics and robust-capon beamforming.

4.4 Discussion

Many of the issues concerned with combining PAM and MR thermometry have been addressed in this chapter. There is minimal interference between the two sys-

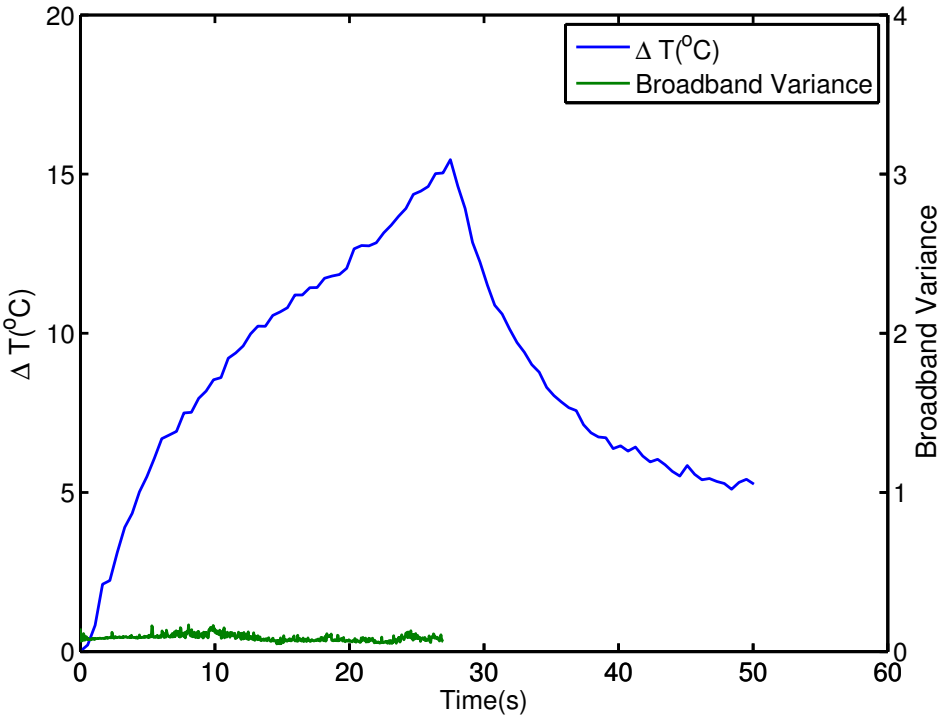

Figure 4.16: This figure shows the maximum temperature over time measured by MR thermometry, and the simultaneous passive mapping data, showing the maximum broadband variance in each PAM frame over time. This exposure was performed at 1MHz with PNFP 2.75MPa, and there is no significant broadband noise measured by PAM, suggesting that there is no inertial cavitation. This is further confirmed by the smoothness of the temperature curve.

tems, and the method of registering the two systems has been confirmed by the co-location of the focus on PAM maps and the centre of heating in MR thermometry images.

In the example shown in figures 4.17 and 4.18 the presence of broadband noise in passive maps correlates well temporally with sharp spikes in heating. When processed with time-exposure acoustics the broadband noise in the maps correlates well in the x direction with the position of enhanced heating, but in the z direction the registration is poor, as the mapped trace contains a large 'tail' spreading in the direction away from the transducer.

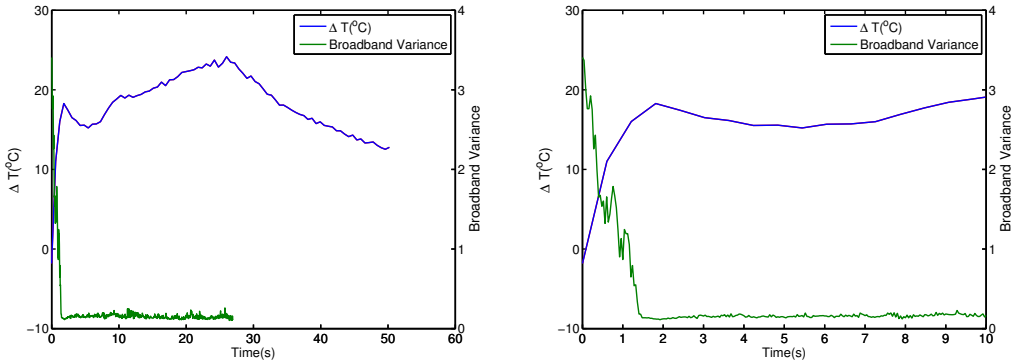

(a) (b)

Figure 4.17: This figure shows the maximum temperature over time measured by MR thermometry, and the simultaneous passive mapping data, showing the maximum broadband variance in each PAM frame over time. (a) shows the whole experiments and (b) shows a close-up of the first 10 seconds. This exposure was performed at 1MHz with PNFP 6MPa, and a 21% duty cycle, and there is significant broadband noise measured by PAM suggesting cavitation. There is a noticeable increase in temperature that coincides with the broadband noise.

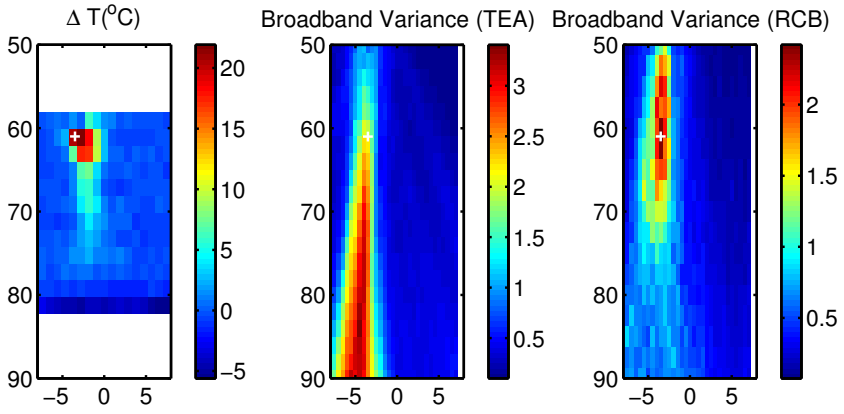

Figure 4.18: Passive maps of broadband variance processed with the Time Exposure Acoustics algorithm (middle) and the Robust Capon Beamformer (right) are shown along with the region of cavitation-enhanced heating (left) estimated by subtracting the expected primary HIFU heating from MR thermometry. The RCB algorithm is able to reduce the 'tail' artefact that appears in the passive maps in the axial direction away from the imaging transducer, towards the HIFU transducer, and the region of cavitation coincides with the centre of enhanced heating.

The robust capon beamformer (RCB) algorithm (Coviello, Faragher, and Cousios, 2010) is able to overcome this. An example is shown in figure 4.18 where the tail has been reduced by around 80%. This makes it much easier to determine how good the registration between MR and PAM images is, and to better determine the spatial extent of the cavitating region. In figure 4.18 there is much better correlation in the z direction between the map created with RCB than with time-exposure acoustics.

This work shows that cavitation on PAM images can appear as a simultaneous enhanced temperature rise on co-registered MR thermometry images. In the next chapter the full set of experiments where cavitation was observed is analysed to further investigate the relationship between cavitation and temperature rise, and the ability of PAM-derived heating sources to estimate cavitation-enhanced heating.

4.5 Conclusions

The experiments in this chapter confirm that simultaneous cavitation mapping and MR thermometry is feasible and by doing so it is possible to monitor multiple aspects of HIFU therapy. It has been shown that in the absence of cavitation, the focus of the HIFU is visible on the passive map. At higher duty pressures the location and duration of cavitation could be detected with the passive mapping but was not detected in MR images. At higher pressures and duty cycles where cavitation was observed it was also possible to observe enhanced heating at the same location in MR thermometry images. In the next chapter every exposure where cavitation was observed is examined in order to investigate the potential for passive maps to predict heating.

CHAPTER 5

MONITORING CAVITATION-ENHANCED HEATING WITH MR THERMOMETRY AND PASSIVE ACOUSTIC MAPPING

5.1 INTRODUCTION

In the previous chapter it was shown that passive mapping and MR thermometry could be performed simultaneously, and that broadband noise in maps correlated spatially and temporally with the location of enhanced heating. In this chapter, we show how the degree of enhanced heating is calculated from MRI thermometry, and estimate cavitation-enhanced temperature rises from acoustic maps by converting a cavitation dose into a heating source.

The motivation is to assess the potential for passive maps to complement , or even replace, MR thermometry to monitor thermal ablation. The basis for this is the work by Jensen, Cleveland, and Coussios (2013) which used acoustic maps and thermal modelling to estimate temperature rises and compared them to those measured

using a thermocouple. By replacing thermocouple measurements with MR temperature maps, the comparison becomes more clinically relevant, and overcomes some of the limitations inherent in using a thermocouple. These include uncertainties about thermocouple artefacts, not just viscous heating artefacts (Morris et al., 2008), but also the thermocouple itself as a nucleus for cavitation. The measurements also become very sensitive to the relative positions of the bubble, thermocouple, and HIFU transducer. MR thermometry does not suffer from these drawbacks, but does come with its own problems, mostly due to its low spatial and temporal resolution. More broadly, while a single point thermocouple measurement of temperature may be correct at that point, nothing is known about the temperature around it. MR thermometry data means the method can be validated over the whole range of the passive map.

In this chapter the method for calculating PAM derived temperature estimates is outlined, before showing the results for nine experiments where cavitation-enhanced heating was observed.

5.2 METHODS

To assess the suitability of passive mapping estimations of heating first the cavitation-enhanced heating is estimated from MR thermometry. This is done by subtracting the expected primary HIFU heating of the incident ultrasound from the total temperature rise. The cavitation heating input is then also estimated from passive maps and used to calculate a temperature rise. The calculated temperature rise is then spatially averaged in order to match the MR output, and the temperatures and thermal doses are compared.

5.2.1 Solving the Bio-Heat Equation

Calculating the temperature rises in tissue requires solving the Pennes bioheat equation (Pennes, 1948). In chapter 1 this was given with two heating terms- a metabolic heating term and an acoustic heating term. As the present work uses non-perfused ex vivo tissue, there is no perfusion term, there is no metabolic heating term, and the acoustic heating term is split into two parts. The Pennes bioheat equation becomes:

$$\rho c_p \frac{\partial T}{\partial t} = K\nabla^2 T + q_{HIFU} + q_{cav} \tag{5.1}$$

where q_{HIFU} is heating from incident HIFU, and q_{cav} the cavitation heating, which is due to the reabsorption of sound scattered by the bubble (Holt and Roy, 2001; Coussios and Roy, 2008), c_p is the specific heat capacity of tissue and K is the thermal conductivity. The thermal properties of tissue used were thermal conductivity, K = 0.7 W (mK)$^{-1}$, density ρ =1050 kg/m^3, specific heat capacity c_p = 3300 J/kg/K. These were based on those used by Jensen, Cleveland, and Coussios (2013) with a slight modification to conductivity to match the cooling curves observed in cavitation-free heating exposures. This value for thermal conductivity is still within 10% of the value measured by Bhattacharya and Mahajan (2003).

This equation needs to be solved twice. Once with q_{HIFU} to subtract the expected heating from MR thermometry measurements, and again after acoustic maps have been converted into a term for q_{cav}.

For calculating q_{HIFU} and q_{cav} the following values were used for the acoustic properties. Speed of sound c_0 = 1592m/s, which was the value measured in chapter 2 and also the value used by Jensen, Cleveland, and Coussios (2013) and B/A was 7.1. the attenuation was taken to follow a power law of $\alpha = \alpha_1 \left(f_{MHz}\right)^{\eta}$ where f_{MHz} is the

frequency in MHz. α_1 was 4.1Np/m at 1MHz (Clarke, Bush, and Ter Haar, 2003) where the fraction due to absorption was $\alpha_{abs} = 0.56\alpha_1$ to give $\alpha_{abs} = 2.3$ (Clarke, Bush, and Ter Haar, 2003) where the frequency dependence of total attenuation and absorption was the same (Goss, Frizzell, and Dunn, 1979).

5.2.1.1 Alternating Direction Implicit Solver

The method used to solve the heating equation was the alternating-direction implicit (ADI) method. This method is unconditionally stable (Ames, 1992), and is easy to implement in multiple dimensions. The method is a reformulation of the finite difference equations that make up the heat equation so that the algebraic equations become a set of linear equations possessing a tridiagonal matrix. These equations are solved one coordinate dimension at a time, so that the solver 'sweeps' through one dimension at a time in a single iteration(Ames, 1992).

The HIFU fields are calculated using cylindrically symmetric versions of the heat diffusion equation. The two finite difference equations that are solved in the two steps of the ADI method are therefore

$$\frac{T_{ij}^{n+1/2} - T_{ij}^{n}}{\Delta t/2} = \frac{K}{\rho c_p}\left(\delta_r^2 T_{ij}^{(n+1/2)} + \delta_z^2 T_{ij}^{n}\right) + \frac{1}{\rho c_p} q_{ij}^{n} \tag{5.2}$$

$$\frac{T_{ij}^{n+1} - T_{ij}^{n+1/2}}{\Delta t/2} = \frac{K}{\rho c_p}\left(\delta_r^2 T_{ij}^{(n+1/2)} + \delta_z^2 T_{ij}^{n+1}\right) + \frac{1}{\rho c_p} q_{ij}^{n} \tag{5.3}$$

where δ_z^2 is the finite difference approximation of a second derivative e.g. $\delta_z^2 u_{i,j}^n = (u_{i+1,j}^n - 2u_{i,j}^n + u_{i-1,j}^n)/(\Delta x^2)$ and δ_r^2 is the finite difference approximation of a second derivative in radial co-ordinates $\delta_r^2 \frac{r_{i+1}\left(\frac{u_{i+1,j}^n - u_{i,j}^n}{\Delta r}\right) - r_i\left(\frac{u_{i+1,j}^n - u_{i,j}^n}{\Delta r}\right)}{r_i \Delta r}$.

These methods were validated by comparing their solutions against analytic solutions. Two analytical solutions are used- one for cooling and one for heating (Morris et al., 2008; Bacon and Shaw, 1993). Cooling was analysed first, as it allowed conduction alone to be verified, then the heating rate, which depends on a the relationship between the rate of heat addition (q) and the rate of conduction.

In 2-D the cooling function for an initial Gaussian temperature distribution $T_0(r) = T_{max} e^{\frac{-r}{\beta}^2}$ where T_{max} is the initial maximum temperature and β the spread.

$$T = \frac{T_{max}}{4\kappa t/\beta + 1} e^{\frac{-r^2}{4\kappa t + \beta}} \tag{5.4}$$

where, κ is thermal diffusivity $\frac{K}{\rho c_p}$. Figure 5.1 shows the radially symmetric ADI simulation agreeing with analytical solutions for cooling, confirming that the ADI method is working correctly. The simulated temperature is within 0.5% of the analytic solution.

The temperature rise for a Gaussian cylinder with intensity I_0 and radius r_0 is

$$T = \frac{\alpha I_0 r_0^2}{2K} ln\left(1 + 4\kappa t/r_0^2\right) \tag{5.5}$$

Figure 5.2 shows agreement for heating, confirming that the ADI method is working correctly. Again, the simulated temperature is within 0.5% of the analytic solution.

For simulating the cavitation-enhanced heating the BHTE is solved in a 2-D Cartesian co-ordinate system, as the PAM system employed here only provides a 2D map of the cavitation field and hence q_{cav}. The finite difference equations employed for cavitation heating are therefore

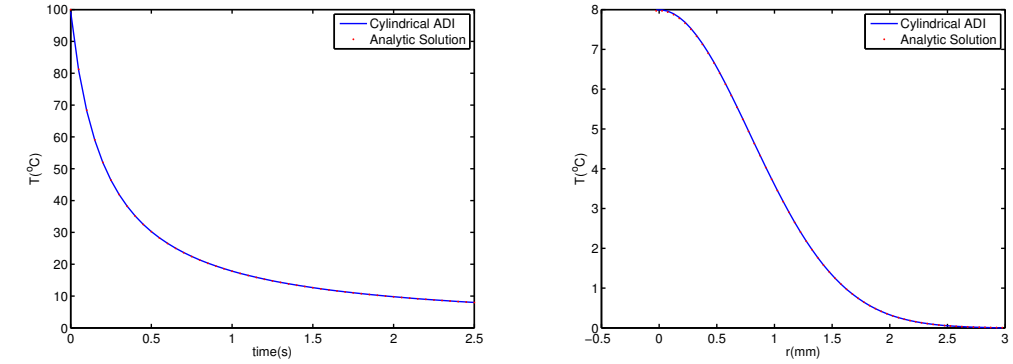

(a) (b)

Figure 5.1: A 2-D Gaussian temperature distribution is used as the initial temperature in the 2-D heating simulation and left to cool as in equation 5.4 T_{max} is 100°C and $\beta = 1 \times 10^{-8}$ The grid extends to 2mm in the z direction and 3mm in the radial direction and the grid size is 0.04mm in z and 0.05mm in r, and the timestep is 0.05s. The cooling curve over time (a) and the shape of the final temperature distribution (b) are compared with the analytical solution in equation 5.4 to verify that the simulation is working correctly.

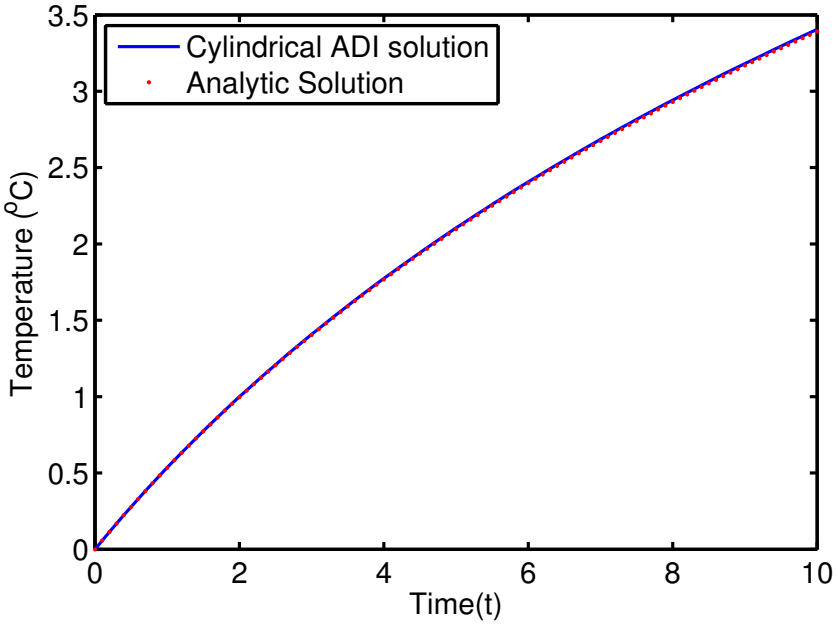

Figure 5.2: A radially symmetric Gaussian heating source varying in the r direction is used as the heating input to an initially uniform temperature field and modelled using the cylindrical ADI solver. The heating curve at the centre of the Gaussian is compared to the analytical solution in equation 5.5 to check that the simulation calculates heating correctly.

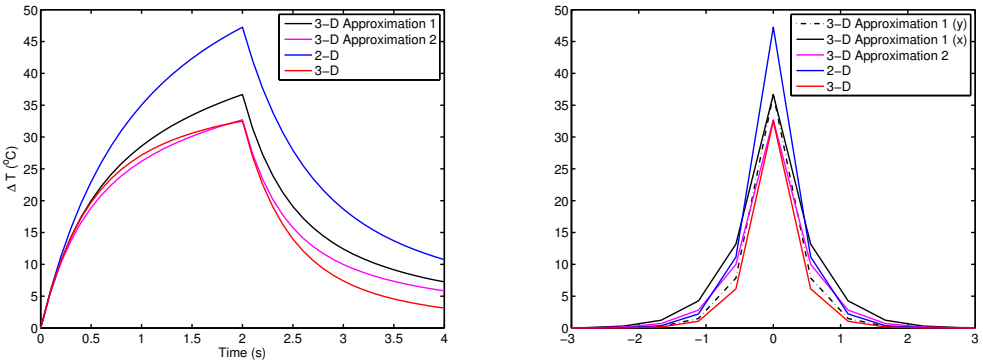

(a) (b)

Figure 5.3: This figure shows heating/cooling curves for a single pixel giving off heat of 20W/cm^3 to simulate a single bubble cavitating for two seconds. The resulting heating cooling curves are shown for 3-D, 2-D, and two different 2-D simulations with increased conductivity in the x and z directions by factors of k_x and k_z to account for extra conduction in the third dimension. In '3-D approximation 1' $k_x = k_z = 1.7$, and in '3-D approximation 2' $k_x = 2, k_z = 1$, as in Jensen, Cleveland, and Coussios (2013). In the simulations in this chapter '3-D approximation 1' was used.

$$\frac{T_{ij}^{n+1/2} - T_{ij}^{n}}{\Delta t/2} = \frac{K}{\rho c_p}\left(k_x \delta_x^2 T_{ij}^{(n+1/2)} + \delta_z^2 T_{ij}^{n}\right) + \frac{1}{\rho c_p} q_{ij}^{n} \tag{5.6}$$

$$\frac{T_{ij}^{n+1} - T_{ij}^{n+1/2}}{\Delta t/2} = \frac{K}{\rho c_p}\left(k_x \delta_x^2 T_{ij}^{(n+1/2)} + \delta_z^2 T_{ij}^{n+1}\right) + \frac{1}{\rho c_p} q_{ij}^{n} \tag{5.7}$$

where T_{ij}^{n} is the temperature at grid position $x(i), y(j)$ at time $t(n)$. k_x and k_y are added conductivity in the x and z directions to account for the lack of conduction in the y axis as described by Jensen, Cleveland, and Coussios (2013). In Jensen, Cleveland, and Coussios (2013) $k_x = 2$ and $k_z = 1$, in this study $k_x = k_z = 1.7$. This was chosen as matches the heating/cooling curve for a single point in 3-D for a heating source one pixel large, as shown in figure 5.3.

5.2.1.2 Sensitivity to Voxel Size and Timestep

Figure 5.4 shows the effect of changing the voxel size on a thermal simulation of a single point heating source with constant power per unit area. This represents the heating for a single bubble where the heat dissipated is all dissipated within one voxel. As the voxel size decreases the maximum temperature reached in the simulation increases as expected, as shown in figure 5.4 (a). However, when averaged over an area the same size as the resolution of the MRI- 2×1mm, as shown in figure 5.4 (b), the result is independent of voxel size in the simulation for voxels below 0.5×0.5mm. This is an important result as it shows that the resolution of heating sources generated from the PAM back-propagation shown in section 5.2.3 of 0.5×0.5mm is sufficiently small to model spatially averaged MR thermometry temperatures, although this low resolution means that the sources provide a lower bound for the actual temperature close to the bubble surface. Figure 5.5 shows the same heating/cooling curves while this time changing the temporal resolution. This becomes a problem at time-steps above 0.4s, which is comfortably above the temporal resolution of PAM which is 25 frames per second.

5.2.2 HIFU Heating

In order to calculate the heating due to HIFU the pressure field from the transducer used for the MRI experiments was measured with a calibrated needle hydrophone. These low pressure measurements were used to determine the nonlinear field at higher pressures using the method described in chapter 3 for the MR compatible HIFU transducer. This transducer has f_0 1.1MHz, the focal length is 98mm and the aperture radius is 32mm. The nonlinear field was then used as the input to the heating equation using the following formula

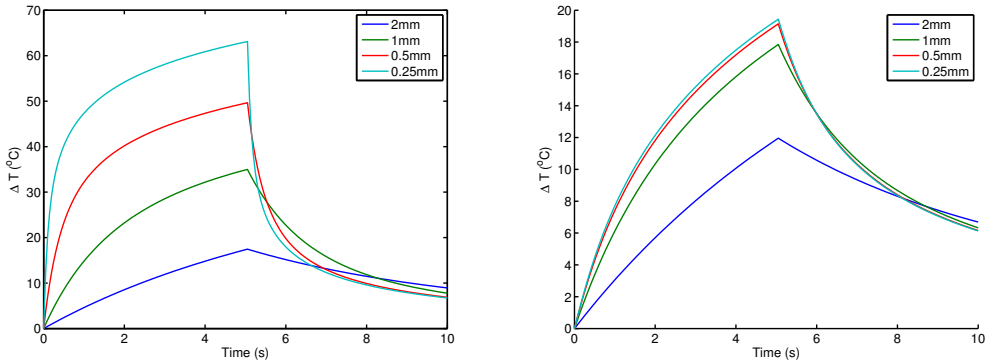

(a) (b)

Figure 5.4: A single point source of constant power lasting 5s is used as an input to the heating simulation. The resulting heating/cooling curves are shown for a range of voxel sizes. The maximum temperature measured over time is shown (a) before and (b) after spatial averaging is applied over an area the same size as an MRI voxel. The maximum temperature rise is measured in (a), and as expected, as the size of the source gets smaller the maximum temperature rise increases. The effect of spatially averaging over an MRI voxel shows that once the voxel size reaches 0.5×0.5mm, the averaged temperature rise over a 2×1mm MR thermometry voxel remains unchanged.

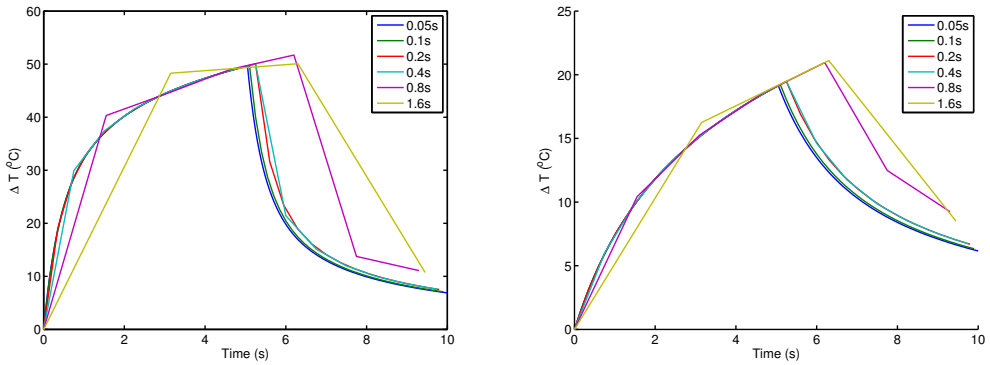

(a) (b)

Figure 5.5: A single point source of constant power lasting 5s is used as an input to the heating simulation. The resulting heating/cooling curves are shown for a range of time-steps. The maximum temperature measured over time is shown (a) before and (b) after spatial averaging is applied over an area the same size as an MRI voxel. For timesteps below 0.4s the heating and cooling curves for a point source at a voxel size of 0.5 × 0.5mm is captured accurately.

$$Q = 2\sum_{n=0}^{\infty} \alpha_n |p(r,z)_n|^2 / 2c_0\rho_0 \tag{5.8}$$

where $p(r,z)_n$ is the magnitude of the nth harmonic and α_n is the absorption at that frequency.

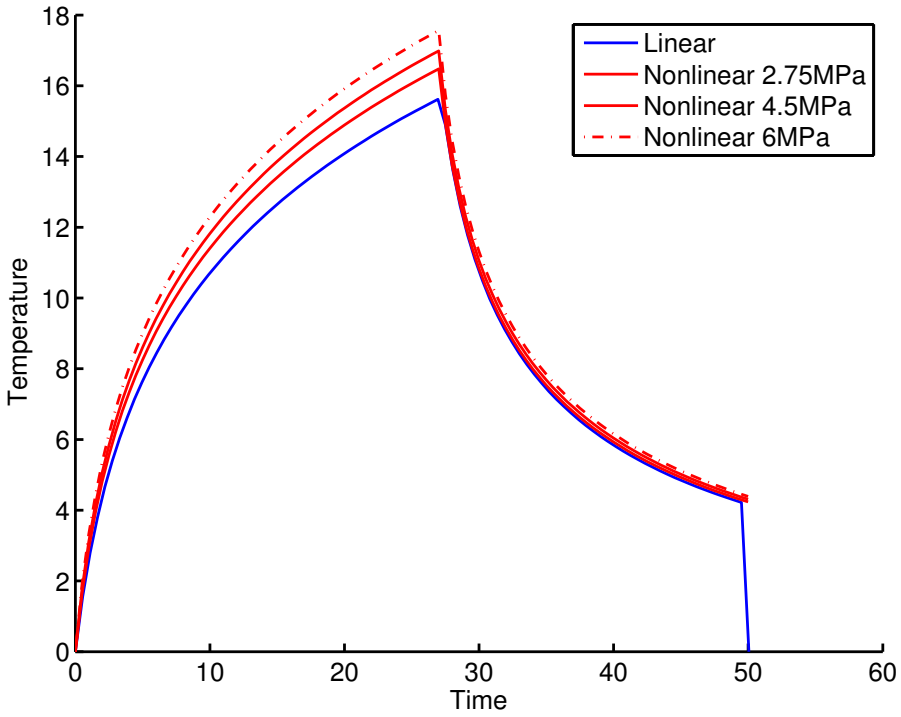

Figure 5.6: Linear and nonlinear heating simulations for the MR-compatible HIFU transducer at the pressures and duty cycles used in the lesioning experiments. f_0 is 1.1MHz, the focal length is 98mm and the aperture radius is 32mm.Three input voltages were used giving peak negative focal pressures of 2.75, 4.5 and 6MPa respectively, and the duty cycles were varied so that $p^2 \times DC$ remains constant.The duty cycle is varied so that the linear power delivered, and linear heating, is the same for every exposure. Nonlinear effects cause increased heating at the focus.

In the combined PAM/MRI experiments the aim of the investigation was to assess the contribution of cavitation to heating independently of other variables. This was achieved by increasing the pressure to initiate cavitation but reducing the duty cycle to keep the time averaged energy input constant. Three input voltages of 275,

450 and 600mV peak-to-peak were used giving peak negative focal pressures of 2.75, 4.5 and 6MPa respectively, and the duty cycles were varied so that $p^2 \times DC$ remained constant, which leads to constant time-averaged power delivered at the focus. This assumes that the output pressure varies linearly with voltage, which hydrophone measurements suggest is a fair assumption over the voltage range considered here. In linear acoustics this would lead to the same heating profile across experiments, but as explained in chapter 2 nonlinear effects mean that this is not quite true.

Figure 5.6 shows the heating profiles for the experiments, as well as the heating profile simulated with linear acoustics. The nonlinear effect leads to enhanced heating at the focus, and higher heating at the focus with increased pressure. These 3-D heating profiles are removed from the MRI thermometry to give an MRI-derived estimate of cavitation-enhanced heating, and added to the PAM derived estimate of cavitation heating to give a PAM and simulation derived estimate of total heating. An example of the initial subtraction process to estimate cavitation-enhanced heating is shown in figure 5.7.

5.2.3 Modelling Cavitation-Enhanced Heating

The method for turning acoustic signals into heating sources is based on the method described by Jensen, Cleveland, and Coussios (2013). There are six steps involved that are outlined here before being described in more detail.

1. cavitation threshold determined from broadband variance in frames analysed with time-exposure acoustics, frames with cavitation present selected
2. frames containing cavitation re-processed using calibrated robust-capon beamforming
3. sources localised

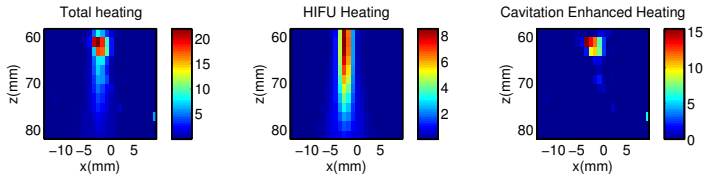

(a)

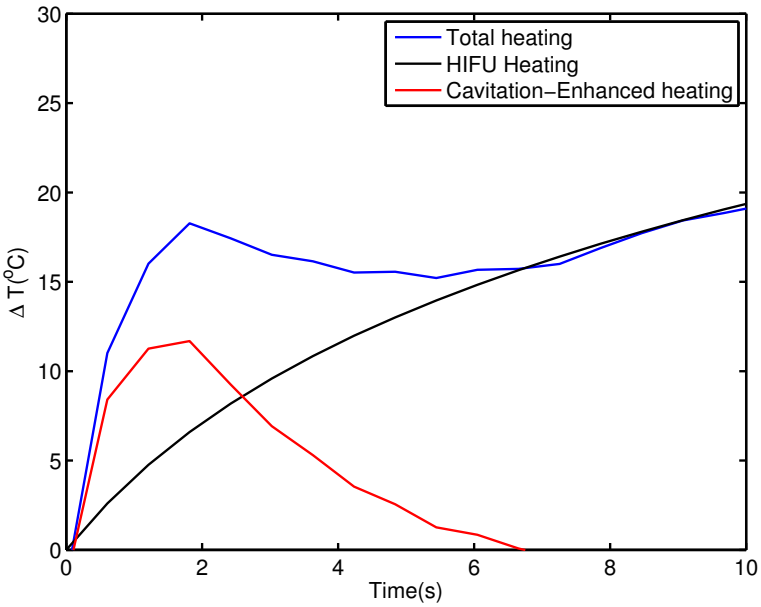

(b)

Figure 5.7: This figure shows total heating measured by MRI, simulated HIFU heating and estimated cavitation-enhanced heating. The cavitation-enhanced heating is estimated by subtracting the simulated HIFU heating from the total heating. The spatial extent of heating in (a) taken at 2s and the heating curves in (b) are taken at $x = -2$, $z = 61$.

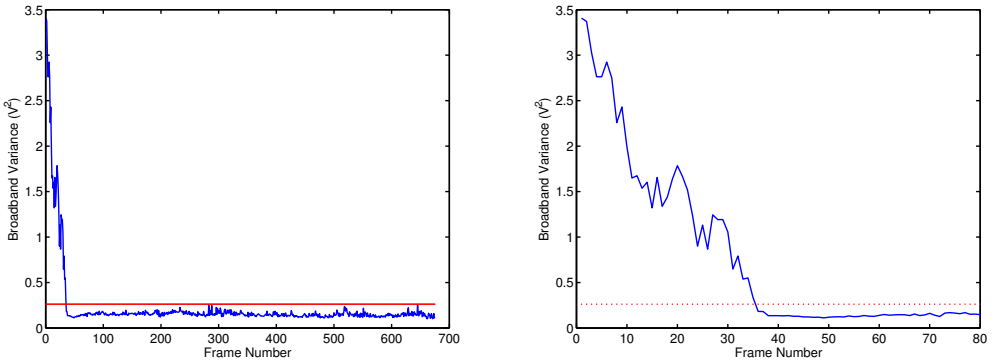

(a) (b)

Figure 5.8: (a) This figure shows the maximum broadband signal over time for a HIFU experiment where cavitation occurs, and the cavitation threshold based on the variance of the final 50 frames. (b) shows the first 80 frames of (a)

4. for each source identified, the source strength is estimated accounting for attenuation in tissue

5. energy loss due to absorption converted into heat input q_{cav}

6. heat input turned into temperature rise using bio-heat transfer equation

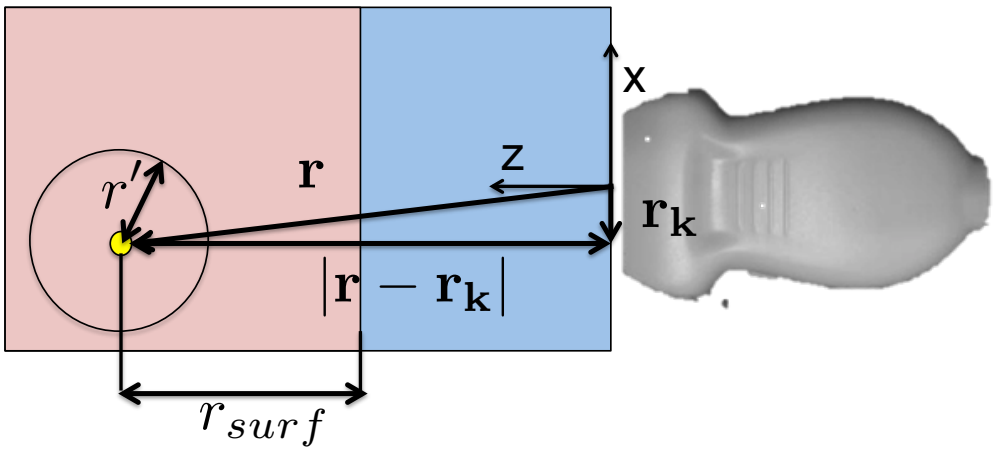

Figure 5.9: Co-ordinate system for calculating cavitation-enhanced heating. A bubble positioned at position $\mathbf{r}$ is recorded on an element of the diagnostic ultrasound array at position $\mathbf{r_k}$. The distance between the sensing element and the bubble is $|\mathbf{r} - \mathbf{r_k}|$ and the distance between the bubble and the tissue surface is r_{surf}. r' is the radial distance from the bubble.

5.2.3.1 Cavitation Thresholding

Although it was shown in section 4.4 that maps processed with time exposure acoustics have artefacts that do not capture the location of cavitation, the maximum value of broadband variance in a map processed this way can still be used to identify frames where cavitation is present. This is useful, as processing with TEA is much faster than RCB. For these experiments, all of the data was processed into maps of broadband variance using TEA, then these maps were used to identify frames where cavitation was present.

In order to identify frames with cavitation present a threshold for broadband noise each was derived for each separate experiment, by examining the maximum broadband variance within each frame. This was done using the method described by Hockham, Coussios, and Arora (2010) by taking the mean and the variance of maximum values of a set of frames with no cavitation present, and identifying any frame where the maximum broadband value was 5 standard deviations above the mean as a frame with significant cavitation present. In the methods described by Hockham, Coussios, and Arora (2010) the cavitation-free frames were frames where only noise was recorded. In this experiment, as the incident ultrasound is visible on passive maps, the 'cavitation free' frames were taken to be the final 50 frames of each experiment, as in all of the observed experiments, by this point all the cavitation has died away. The maximum broadband variance and the noise threshold for one experiment is shown in figure 5.8.

5.2.3.2 Robust Capon Beamforming

For each exposure where cavitation is identified the frame is reprocessed using the robust Capon beamformer method as described in section 4.1.3. The only difference in the method is that the calibration shown in figure 5.10 is applied to the volt-

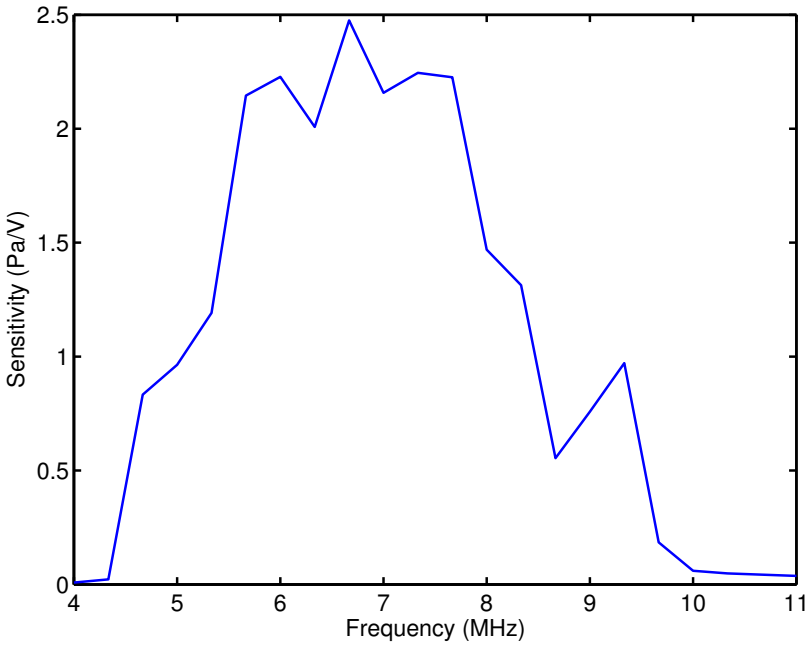

Figure 5.10: The sensitivity of the Zonare array used to convert the rf traces from voltage into pressure in the frequency domain.

ages in the frequency domain as opposed to the nominal sensitivity of 1 used for the time-exposure acoustics processing.

5.2.3.3 Source Localisation

After this stage sources within each PAM frame are identified using the closed contour method described by (Jensen, Cleveland, and Coussios, 2013). An iso-intensity contour map using 20 evenly spaced contour levels from 0 to the maximum value of broadband variance in the frame is created from the PAM image. A source will have several closed contour curves encircling it, a threshold of three or more closed contours surrounding a peak is used to identify possible sources in the maps. An example of the process taking an RCB image, creating a corresponding contour map, and isolating sources is shown in figure 5.11.

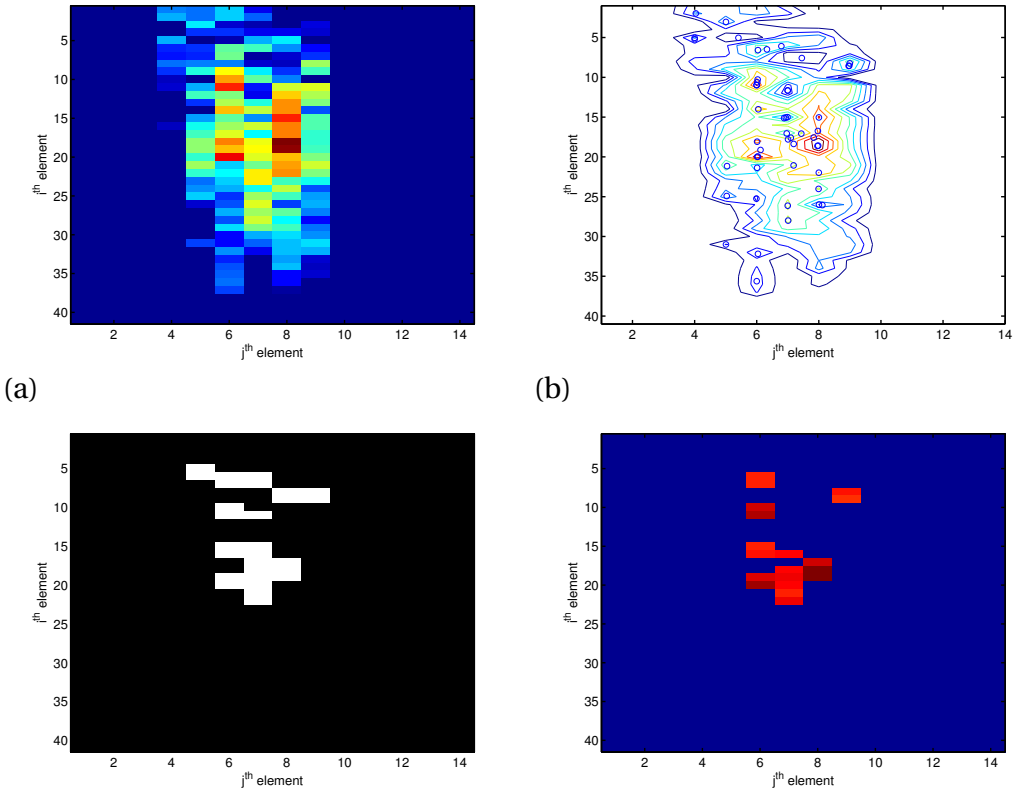

Figure 5.11: This figure shows the process of identifying individual cavitation sources from a PAM image. (a) shows the passive map processed with RCB for a PAM frame identified as containing cavitation. (b) shows the closed contour plot. Pixels enclosed by 3 or more close contours are shown in (c). These pixels are counted as individual sources, and the final image containing only sources is shown in (d)

5.2.3.4 Attenuation

The sources are now identified and localised. For each source identified in the frame, its strength is recalculated, this time with attenuation taken into account. To do this it is assumed that attenuation only happens in the tissue. The intensity at the tissue surface is calculated, before being back-propagated into the tissue as described in the following section.

Using the co-ordinate system in figure 5.9, a source at location **r** has acoustic intensity

$$I = \frac{W(\mathbf{r})}{4\pi r'^2} \tag{5.9}$$

where r' is the radial distance from the bubble at position $\mathbf{r}$. The intensity at the tissue surface is

$$I_{surf} = \frac{W}{4\pi r_{surf}^2} \tag{5.10}$$

where r_{surf} is the distance from the position of the source to the tissue surface, in a straight line from the source position to the origin at the middle of the transducer.

The intensity inside the tissue at position r' from the bubble is given by the following equation for intensity at the tissue surface, and back-propagated to a bubble of 1 micron radius by using an ODE solver for the equation's derivative, using the intensity at the tissue surface as the initial value.

$$I(r') = \left(\frac{r_{surf}}{r'}\right)^2 \frac{1}{4\pi r_{surf}^2} \frac{1}{4\pi\rho c} \frac{1}{N_{DFT}} \sum_{m}^{N_{DFT}} Q_m'^2 e^{-2\alpha_m(r'-r_{surf})} \tag{5.11}$$

$$\frac{dI}{dr'} = -2I\left(\frac{1}{r'} + \frac{\sum_{m}^{N_{DFT}} \alpha_m Q_m'^2 e^{-2\alpha_m(r'-r_{surf})}}{\sum_{m}^{N} Q_m'^2 e^{-2\alpha_m(r'-r_{surf})}}\right) \tag{5.12}$$

5.2.3.5 Cavitation-enhanced heating sources

There are two components in this derivative, one term that accounts for spherical spreading, and one that accounts for attenuation losses. The attenuation is made up of two terms- scattering and absorption. It is absorption (α^{abs}) that contributes to heating, so the final heating, therefore the intensity that provides the heating term q_{cav} in the heating equation is

$$q_{cav}(r') = I(r') \left(\frac{\sum_{m}^{N} 2\alpha_m^{abs} Q_m'^2 e^{-2\alpha_m (r' - r_{surf})}}{\sum_{m}^{N} Q_m'^2 e^{-2\alpha_m (r' - r_{surf})}} \right) \tag{5.13}$$

This function decays very quickly with increasing r', on the order of a few bubble radii (microns), due to the very fast decay of the high frequency components of the broadband bubble signal, and the radial dependence of $I(r')$. This is a fast enough decay that the heating is all contained within a single element in a heating simulation where an element size is tens if not hundreds of microns. Therefore to find the heating input to use in a simulation where the length and width of each pixel is Δ, we find the total heat input per unit volume by integrating the heat input over a sphere of the same volume, i.e $\frac{4}{3}\pi R_\Delta^3 = \Delta^3$.

$$q_{sim} = \int_0^{R_\Delta} \frac{q_{cav}(r') 4\pi r'^2}{\frac{4}{3}\pi R_\Delta^3} dr' \tag{5.14}$$

An example PAM-derived heating frame is shown in figure 5.12

5.2.3.6 Simulating Temperature Rise

Individual PAM-derived heating frames are used as heating inputs. Although each PAM frame uses samples that are 138µs long, cavitation is assumed to remain stationary in between frames. This is a reasonable assumption as cavitation events often persist from one frame to another. The heating simulation progresses at a time-step of 0.05s, similar to the PAM time-step of 0.04s. The simulation finds the closest corresponding PAM frame at every point, and if it is a frame that contains cavitation, uses the processed frame as the heating input.

This heating simulation is run at a length scale of 0.5mm, which is smaller than the MR thermometry voxel size of 1mm × 2mm. The simulations are therefore spa-

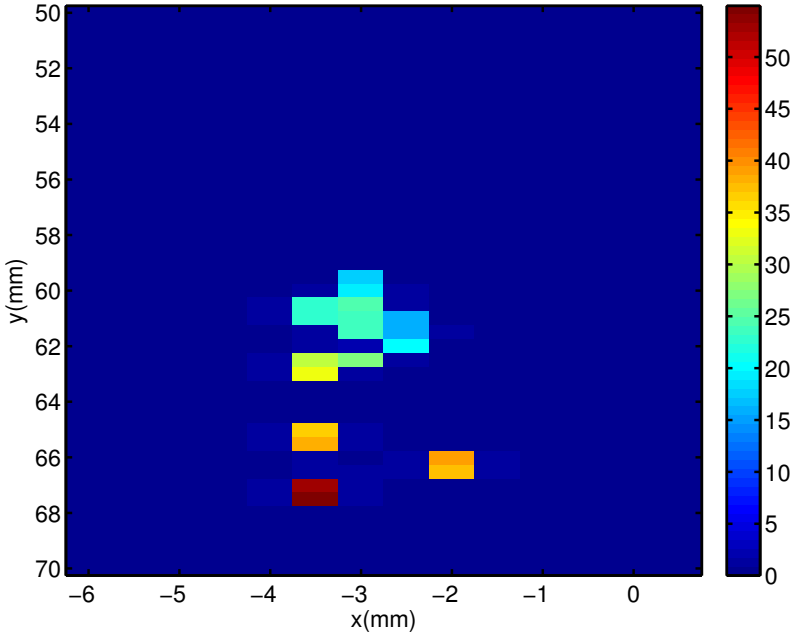

Figure 5.12: The heating input map in W/cm ^{3} derived from the sources identified in figure 5.11, after each source has had attenuation taken into account.

tially averaged to match the MR thermometry. This is done by averaging the 2-D temperature matrix over1×2mm sections.

5.3 Results

5.3.1 Heating in the absence of Cavitation

In the absence of cavitation nuclei and at low pressures there is no broadband noise and no cavitation-enhanced heating. This allows the accuracy of the thermal simulation to be verified. Figure 5.13 shows measured and simulated temperature fields in ex-vivo ox liver without cavitation nuclei added at 1MHz, with constant duty cycle at 2.75MPa peak negative pressure. Figure 5.13 (a) shows the maximum temperature over time. Figure 5.13 (b) shows the spatial extent of the heating in x,z co-ordinates. The top left section of 5.13 (b) shows the spatial extent of the heating measured by

MR thermometry at the end of the HIFU exposure (before cooling begins). The top right and bottom left sections show the simulated HIFU heating, before and after spatial averaging has been applied. The bottom right section shows the residual heating error between the simulation and the measurement. There is good spatial and temporal agreement between the simulated and the measured temperature rise, shown here at -2.75MPa, with the correct heating and cooling curves

5.3.2 Cavitation-Enhanced Heating

With cavitation nuclei added, cavitation leads to enhanced heating. The exposure shown in figure 5.14 was conducted at 6MPa peak negative focal pressure in ex vivo liver with cavitation nuclei added. There is a spike of broadband noise that coincides in time with a spike in the temperature that is visible once the expected HIFU heating has been subtracted. It was shown in figure 4.18 that passive maps processed with Robust Capon beamforming also give good spatial agreement. In this section a single exposure is examined in detail before the other results are considered.

5.3.2.1 Heating Sources from Passive Mapping

Figure 5.15 shows the average broadband variance and the average heat input q_{cav} for frames containing cavitation in the exposure shown in figure 5.14.

The temperature at the focus is shown as a function of time in figure 5.16 (a). After spatial averaging the temperature of the simulation matches the heating/cooling curve of the MR thermometry at the location of the bubble to within 1°C during the heating phase. Figure 5.16 (b) shows the spatial extent of cavitation-enhanced heating at the end of the cavitation activity alongside the cavitation-enhanced heating estimated from MR thermometry.

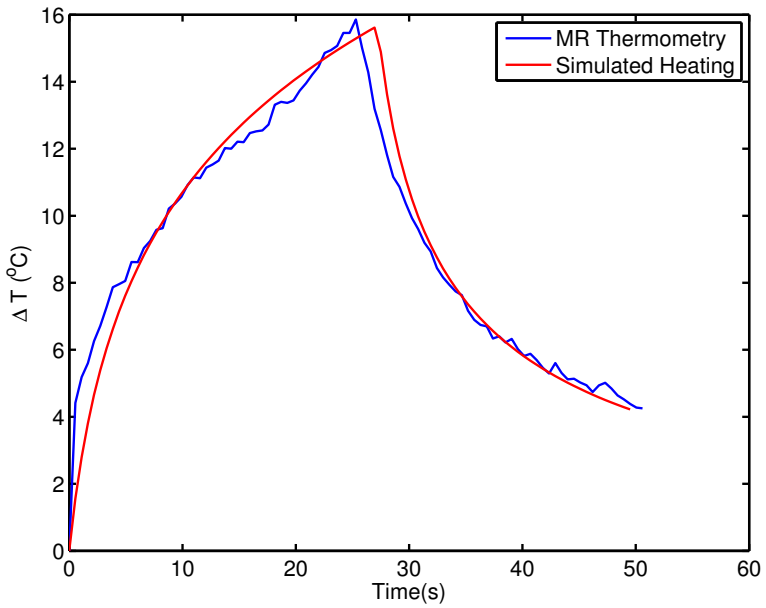

(a)

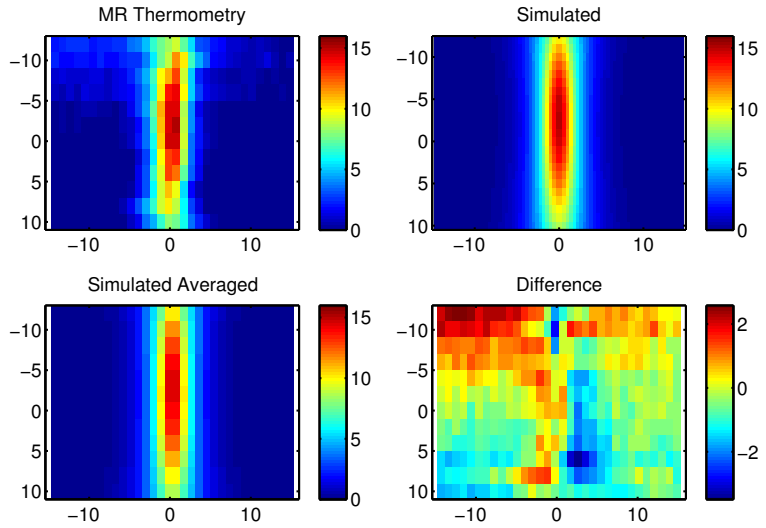

(b)

Figure 5.13: The temperature rise and subsequent cooling from a HIFU exposure without cavitation. It shows temperature measured with MR thermometry compared with a simulation. (a) measured and simulated heating and cooling curves and (b) the spatial extent of the temperature rise at the end of the HIFU exposure (27s). The top left of (b), the MR thermometry heating frame at the end of the HIFU exposure. The top right and bottom left sections of (b), the simulated HIFU heating, before and after spatial averaging. The bottom right section of (b), the residual error between simulation and measurement. This is for a peak negative pressure of 2.75MPa at 1.1MHz at 100% duty cycle.

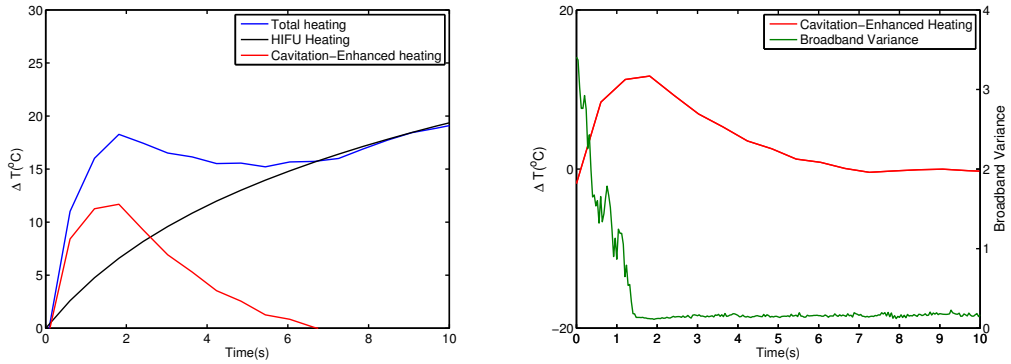

(a) (b)

Figure 5.14: (a) Heating and (b) cavitation-enhanced heating and broadband energy over time for an exposure at -6MPa PNFP with cavitation nuclei added. There is a large jump in temperature at the start of the exposure that correlates in time with the presence of broadband emissions.

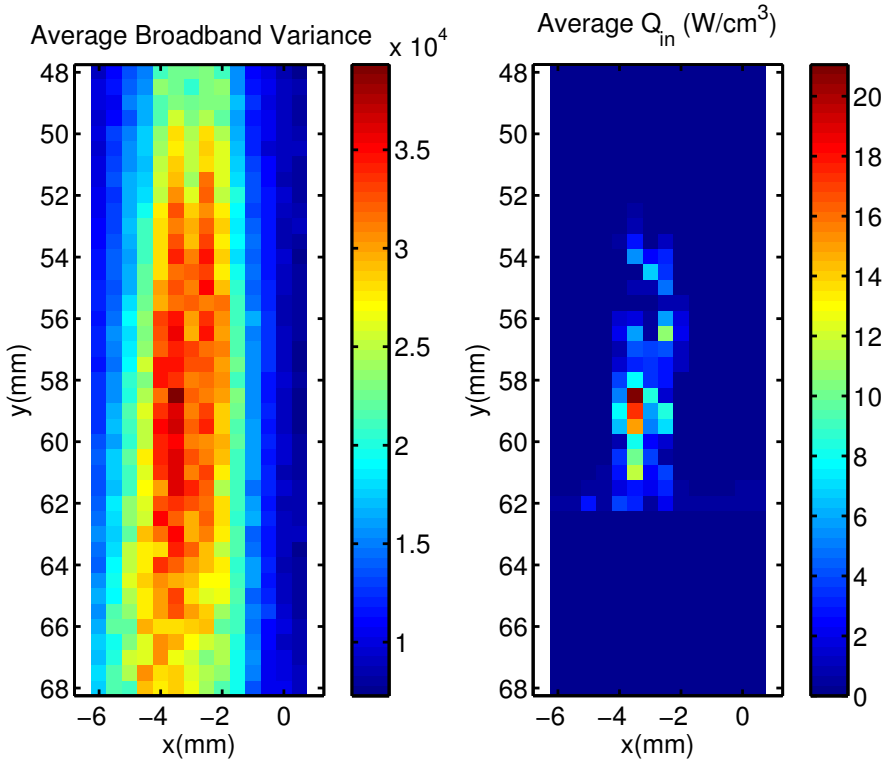

Figure 5.15: The average broadband variance and heat input in PAM frames containing cavitation, processed over the cavitating region. Left: the average values of the passive maps processed with the Robust Capon beamformer. Right: the average cavitation heating input q_{cav}, derived from passive maps.

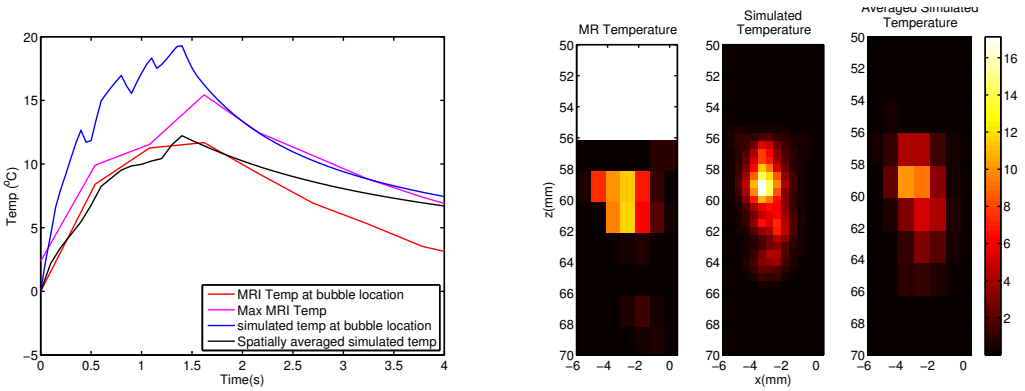

(a) (b)

Figure 5.16: (a) Measured cavitation-enhanced heating compared with heating sources calculated from the back propagated passive mapping signal. Once the cavitation-enhanced heating has been spatially averaged, there is good agreement. (b) Measured cavitation-enhanced heating compared with heating sources calculated from the back propagated passive mapping signal. This image was taken just after the cavitation activity had finished, before the cooling period started, which occurs at 2s in (a).

5.3.2.2 Point Source

As a comparison with the full passive map to heating source conversion a simpler method was investigated. This method uses a cavitation heating source that is one voxel large, and that has a magnitude that is scaled proportionally to the maximum value of broadband energy in one acoustic frame multiplied by a constant scaling factor. The position of the source is determined by the centroid of the passive map. This is analogous to the methods suggested by Farny, Holt, and Roy (2010), Arvanitis and McDannold (2011), and Kyriakou et al. (2011) where they show a linear relationship between enhanced temperature rise and broadband noise. The heating curves are shown in figure 5.17 and the spatial extent of the cavitation-enhanced heating is shown in figure 5.18. In figure 5.17 the temperature rise after spatial averaging is able to match the maximum temperature rise against time to within 2°C. At the end of the cavitation the cooling is much more abrupt in the simulation than in the measurement. In figure 5.18 the left hand figure shows the cavitation-enhanced heating

estimated from MR thermometry, the right hand figure shows the spatially averaged simulated temperature rise. After spatial averaging the area of the simulated temperature rise is around two voxels large, but in the MR thermometry the area at a similar temperature is 7 voxels large. The simulated area of heating is smaller than that shown by MR thermometry.

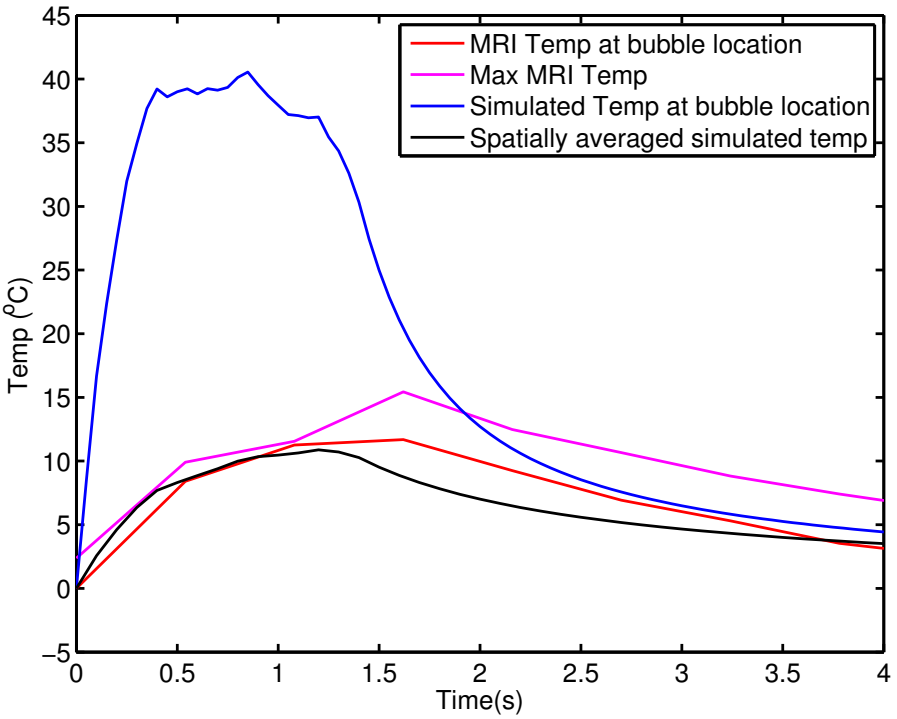

Figure 5.17: MR-thermometry estimated cavitation-enhanced heating compared with PAM-derived simulated heating over time. A point source with intensity scaled relative to the magnitude of the PAM signal is used as the heating input. With the correct scaling the spatially averaged temperature matches the measured heating.

Comparing the two methods, in the heating curves in figures 5.16 and 5.17 the degree of cavitation-enhanced heating is captured to within 2°C in both methods, with errors of up to 5°C during the cooling phase. Comparing the spatial extent of heating in 5.16 and 5.18 there is a much better spatial match between the MR estimates and PAM estimates of enhanced temperature rise using the full PAM-derived

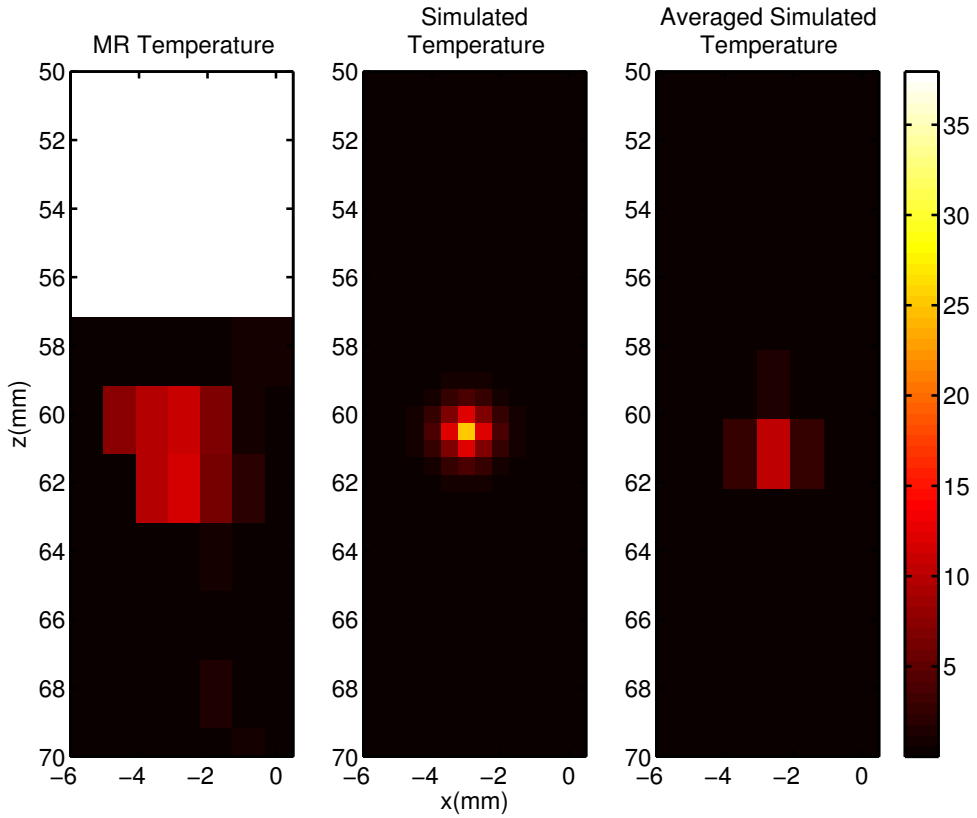

Figure 5.18: Cavitation-enhanced heating estimated by MR thermometry compared with simulated heating derived from passive mapping. A point source with intensity scaled relative to the magnitude of the PAM signal is used as the heating input. With the correct scaling the spatially averaged temperature has a similar shape to the measured temperature.

method than with the single voxel source by looking at the width and the depth of the heated area.

5.3.2.3 Total Heating and Thermal Dose

The predicted cavitation-enhanced temperature rise is added to the HIFU heating to obtain the total temperature rise. Thermal ablation associated with heating was simulated by converting the total temperature rise to cumulative equivalent minutes at 43°C using the standard formula (Sapareto and Dewey, 1984)

$$CEM_{43} = \int_0^t R^{43-T(t')} dt' \tag{5.15}$$

Where $R = 0.5$ for $T > 43$ °C and R=0.25 for $T <= 43$ °C. Here 240 equivalent minutes is taken as the dose required to thermally ablate tissue.

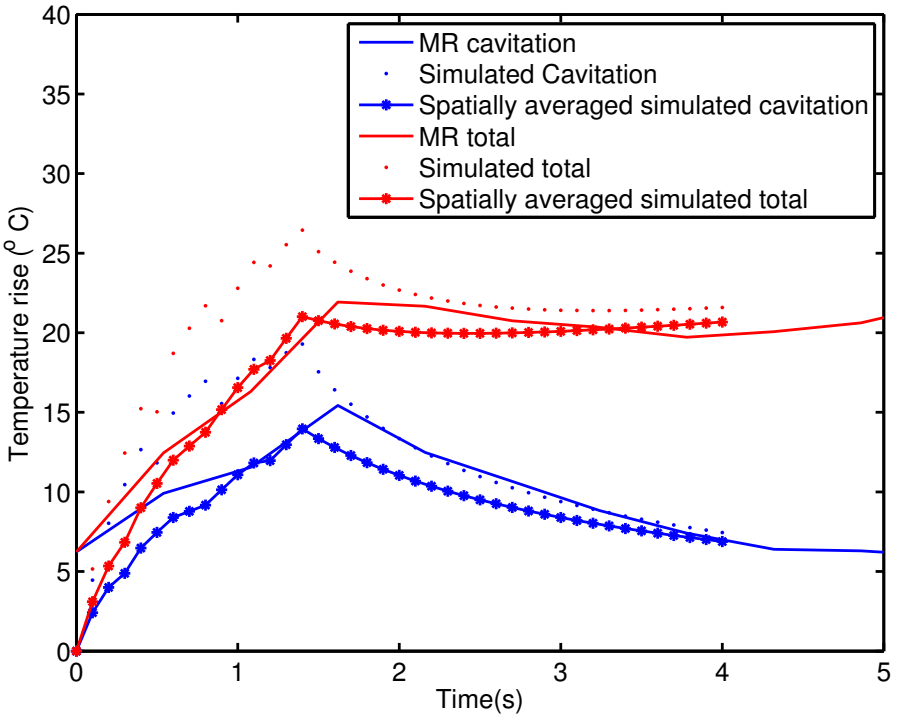

Figure 5.19: MR heating compared with heating derived from heating simulations. The blue heating curves show cavitation-enhanced heating while the red curves show the combination of cavitation-enhanced heating and HIFU heating. The solid red line shows the MR thermometry measurement, the solid blue line shows the MR thermometry derived estimate of cavitation-enhanced heating. For the simulations the dotted and solid-dotted lines show the results of the heating simulation before and after spatial averaging. There is good agreement between the two methods once the simulated signal has been spatially averaged.

Figure 5.19 shows the heating and curves for cavitation-enhanced heating estimated from MR thermometry and predicted using PAM. It also shows the heating curves for the total heating measured by MRI, and the predicted total heating from simulations where the PAM estimate of cavitation-enhanced heating is added

to a simulation of HIFU heating. For the simulated temperature rises two heating curves are shown- one for the result of the heating simulation run at a spatial scale of 0.5mm, one for the simulation after it has been spatially averaged to the same scale as the MR thermometry. After spatial averaging there is good agreement between the simulated heating and the MR thermometry measurements.

Figure 5.20 (a) spatial comparisons of measured and simulated temperature rises for cavitation-enhanced heating alone, and total heating. Top row shows cavitation-enhanced heating, bottom row total heating. First column shows simulated temperature images, the middle column shows spatially averaged simulations and the third column shows MR thermometry temperature images. These are taken at a time corresponding to 2s on Figure 5.19. (b) The thermal dose calculated for the thermal simulation, the spatially averaged simulation, and the MR thermometry measurements after the cavitation has subsided, with the dark red areas showing voxels where 240 equivalent minutes have been exceeded.

In order to assess the degree of similarity between the two methods for estimating temperature, Figure 5.21 (a) shows the maximum error between any two corresponding voxels in the spatially averaged and MR thermometry temperature images over time. Although the difference between the maximum temperature in the two methods is within 30% for more than 90% of the time, the maximum error between corresponding pixels is within 70% 90% of the time. The maximum error between the corresponding pixels is very large, almost as large as the temperature rise itself, even though the match between maximum temperatures is good. This shows the danger of comparing the simulation to single-point thermocouple readings. Figure 5.21 (b) shows the growth in predicted lesion size over time for the two methods. At the end of the simulation the lesion sizes predicted by the two methods differ by 3.5mm^2.

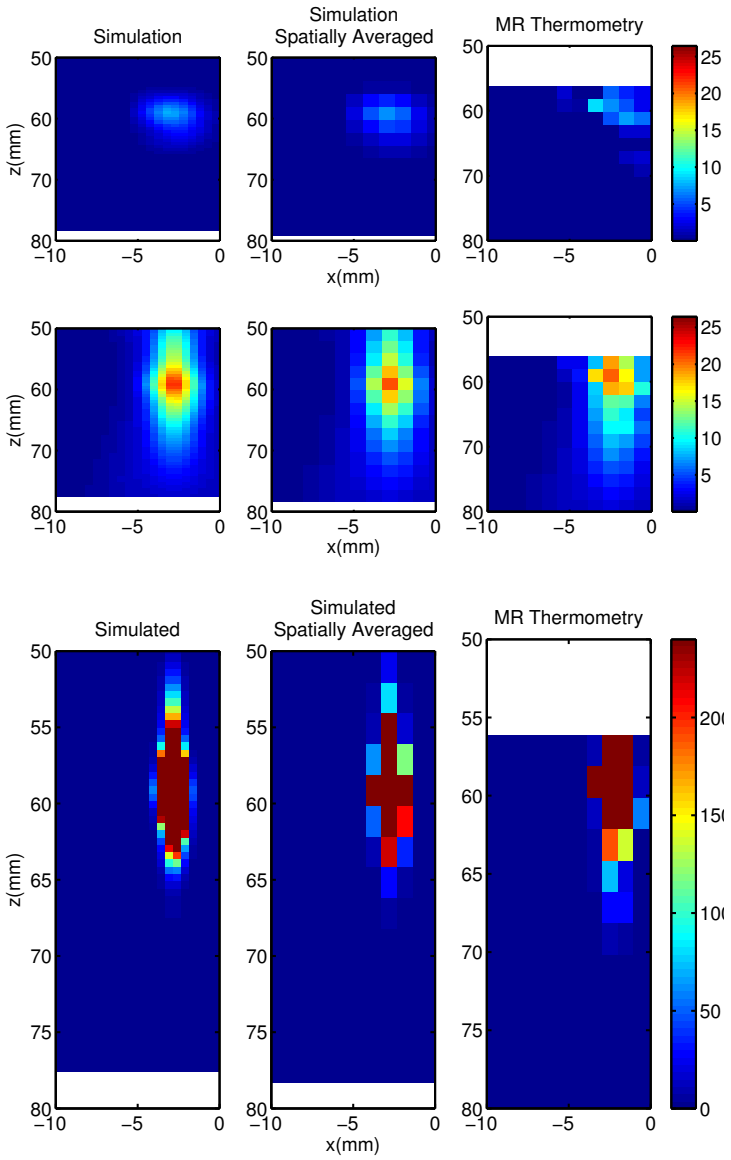

Figure 5.20: (a) shows temporal and spatial comparisons of measured and simulated temperature rises for cavitation-enhanced heating alone, and total heating. The top row shows cavitation-enhanced heating, the bottom row shows total heating. The first column shows simulated temperature images, the middle column shows spatially averaged simulations and the third column shows MR thermometry temperature images. These imaged are taken at a time corresponding to 2s on Figure 5.19. (b) shows the thermal dose calculated for the thermal simulation, the spatially averaged simulation, and the MR thermometry measurements after the cavitation has subsided, with the dark red areas showing voxels where 240 equivalent minutes have been exceeded.

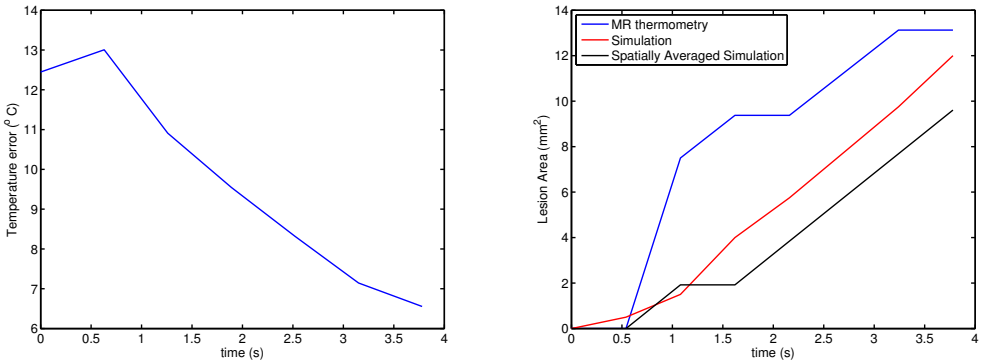

(a) (b)

Figure 5.21: (a) The maximum error between PAM and MR derived heating during the cavitation activity and cooling (b) Estimated lesion size from PAM and MR derived cumulative equivalent minutes at the end of cavitation activity.

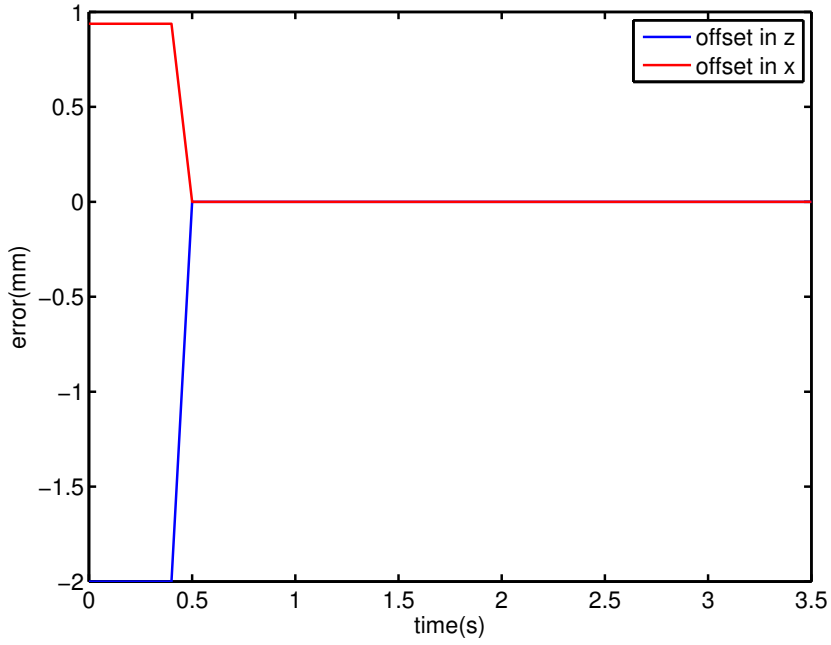

Figure 5.22: The figure shows the difference in mm between the location of the maximum measured and estimated temperatures during the exposure.

Figure 5.22 shows the distance between the location of the hottest pixels in the measured and simulated temperature maps. This is a way of assessing how accurately the PAM-derived simulation of temperature captures the location of the heating. The maximum difference is 1mm in the x direction and 2mm in the z direction which corresponds to an offset of 1 voxel in each direction for the first 0.4s, after that there is no difference in the location of the hottest voxel.

The method gives a reasonable estimate of cavitation-enhanced temperature that matches the degree and location of the cavitation-enhanced temperature rise estimated by MR thermometry, as well as matching the spatial extent of the predicted lesion size. Having been shown to work once, the method is now applied to a larger number of experiments.

5.3.2.4 Other Exposures

Thirteen experiments were conducted in ex-vivo liver with cavitation nuclei added with simultaneous passive acoustic mapping and MR thermometry. Of these 7 experiments were conducted at 4.5MPa PNFP and 6 at 6MPa PNFP. Significant cavitation was observed in 5 of the 7 experiments at 4.5MPa and 4 of the 6 experiments at 6MPa. In total there were 9 exposures where significant cavitation was recorded. Of these, including the example shown in section 5.3.2.1, there were 3 experiments at 6MPa and 1 experiment at 4.5MPa where passive maps were able to capture the temperature rise to a reasonable degree. There was 1 experiment at 4.5MPa and 1 at 6 where the method succeeded to an extent and 3 experiments at 4.5MPa where the method did not capture the behaviour of the measured temperature.

Figure 5.23 shows comparative heating curves and spatial images of temperature for the three other successful experiments. In all of these experiments, the heating sources from passive maps were able to match the temperature rise to a reasonable

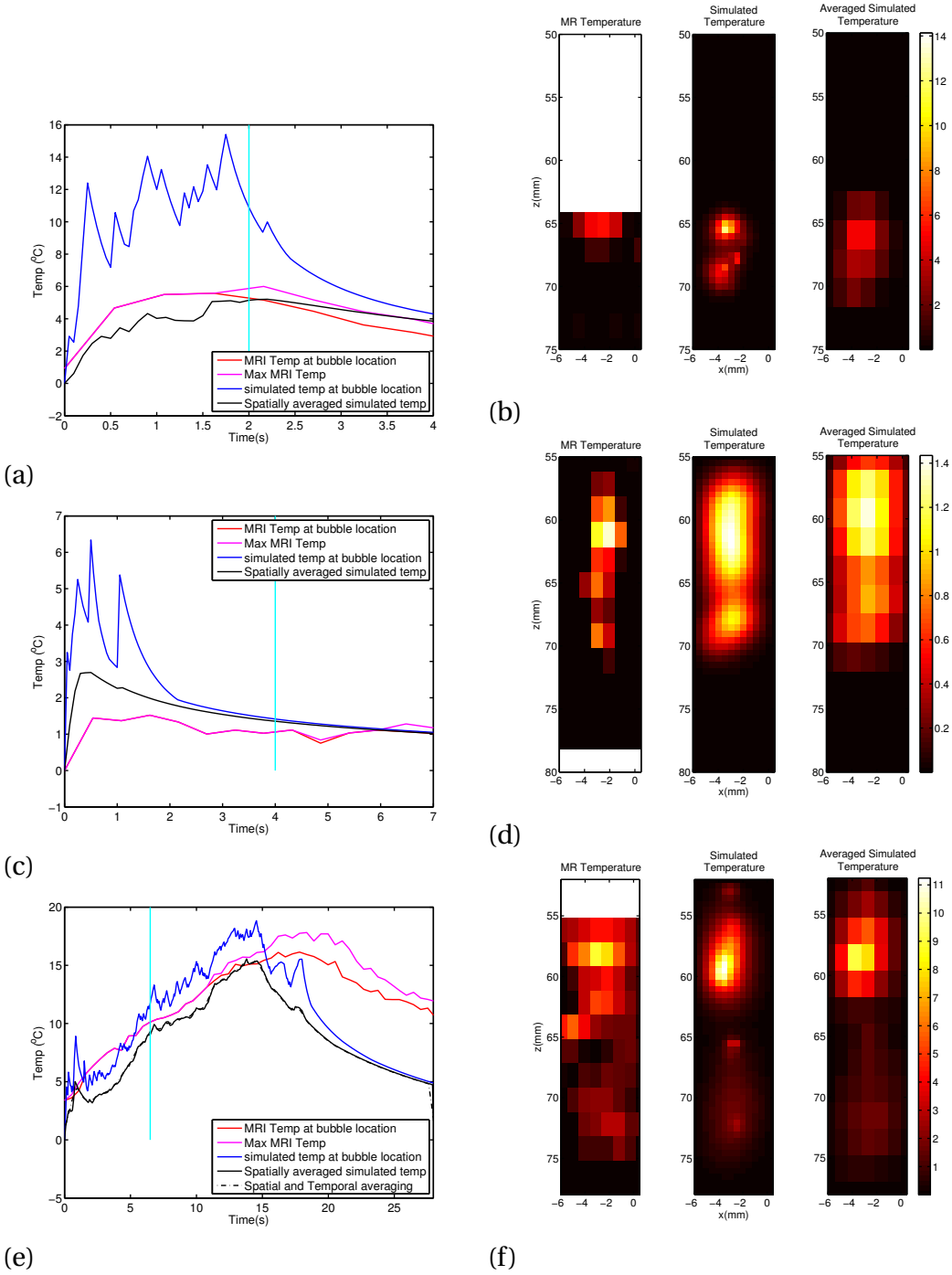

Figure 5.23: Successful PAM derived estimates of temperature rise. In these exposures and the data shown in figure 5.16 the estimated temperature rises match the simulated temperature rises to a reasonable degree.

degree and also the spatial extent.

In figures 5.24, 5.25, 5.26 the total heating, the estimated thermal dose, the distance between the hottest voxels in the two methods, and the growth of the estimated lesion area over the duration of the cavitation, is shown for each individual case.

The exposure in figure 5.23 (a,b) is shown in more detail in figure 5.24. The largest temperature error between the maximum temperatures in the two methods is 2.7°C and 90% of the temperature measurements by the two methods are within 33% of each other. In this exposure the degree of cavitation-enhanced heating is relatively small. The predicted thermal dose predicts no damage for either the MR measurements or the spatially averaged PAM simulations at the end of the cavitation, but there is a small predicted lesion in the PAM simulation before averaging is applied.

The exposure in figure 5.23 (c,d) is shown in more detail in figure 5.25. The largest temperature error between the maximum temperatures in the two methods is 1.8°C and 87% of the temperature measurements by the two methods are within 25% of each other. Again, the predicted thermal dose predicts no damage for either the MR measurements or the spatially averaged PAM simulations at the end of the cavitation, but there is a small predicted lesion 0.6mm^2 in the PAM simulation before averaging is applied.

The exposure in figure 5.23 (e,f) is shown in more detail in figure 5.26. The largest temperature error between the maximum temperatures in the two methods is 7.3°C and 94% of the temperature measurements by the two methods are within 30% of each other. the lesion predictions for both methods predict similarly sized lesions at the end of the cavitation, 112.5mm^2 for the PAM simulation, 111.4mm^2 for the

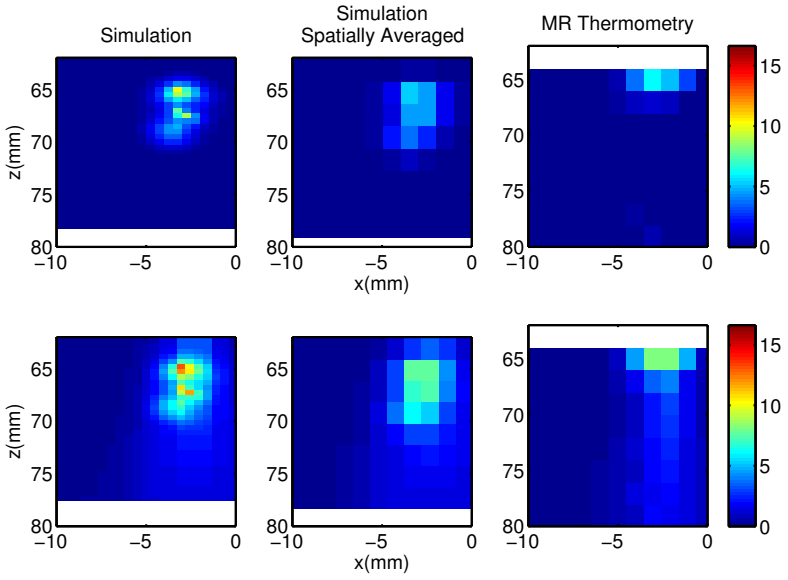

(a)

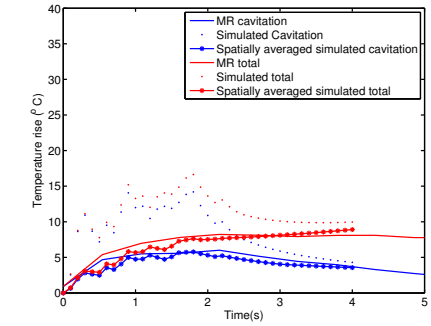

(b)

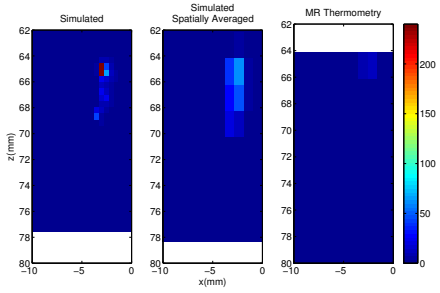

(c)

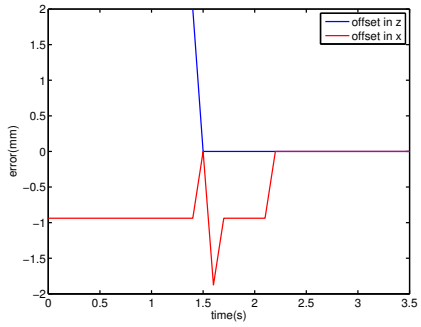

(d)

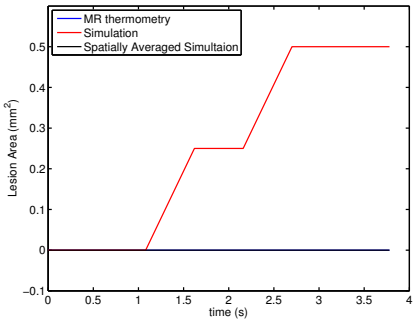

(e)

Figure 5.24: (a) Cavitation-enhanced heating and the total heating at 2s, (b) Measured and predicted focal temperatures (c) Estimated thermal dose for the two methods, (d) the distance between the location of the maximum temperature in the two methods and (e) Estimated lesion area for the duration of the cavitation.

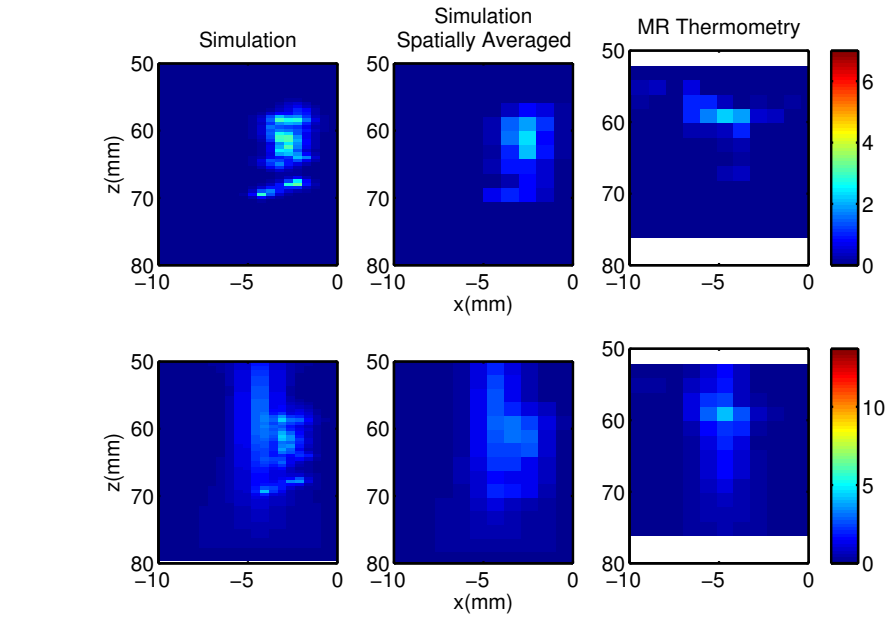

(a)

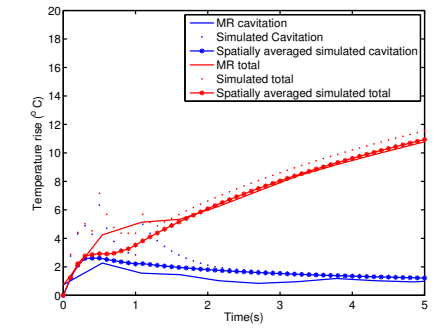

(b)

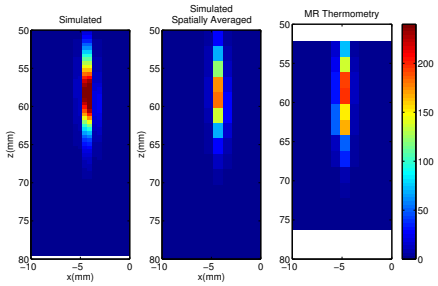

(c)

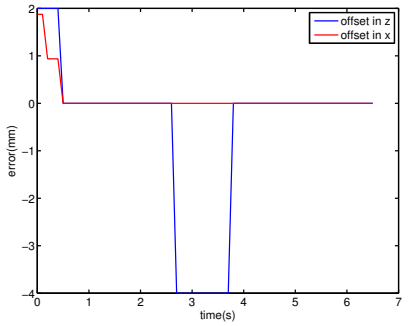

(d)

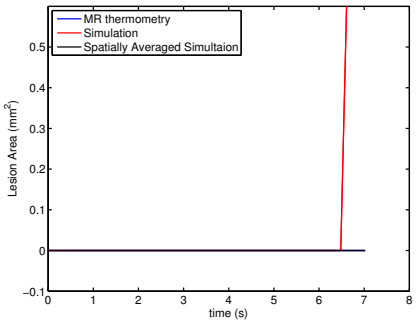

(e)

Figure 5.25: This figure shows (a) the cavitation-enhanced heating and the total heating at 2s, (b) measured and predicted focal temperatures (c) the estimated thermal dose for the two methods, (d) the distance between the location of the maximum temperature in the two methods and (e) the estimated lesion area for the duration of the cavitation.

spatially averaged simulation, and 97.5mm^2 for the MR derived lesion.

In order to assess the spatial accuracy of the simulations the position of the hottest pixel was tracked for each method. These are shown in figures 5.22,5.24(d),5.25(d) and 5.26(d). The offset is mostly 0, with occasional errors up to the a distance of 4mm, or 2 pixels in the z direction. In figure 5.26 (d) the error is much larger- over 12mm. The cause of this discrepancy is shown in figure 5.27 where there are two areas of cavitation activity that create a similar temperature rise. Although the PAM-derived heating estimate captures both of these to within a few degrees, and at the correct positions, the temperatures are so similar that the wrong cavitating area is temporarily the hottest pixel.

The experiment shown in Figure 5.26 is also a special case in that thermally relevant cavitation continues for the complete 27s exposure. This means that cavitation has a significant effect on estimates of final lesion size, and that these estimates can be compared to a ge3d MR image of the lesion. Figure 5.28 shows the measured and estimated temperatures converted into thermal doses and compares them with a thresholded image of the tissue post treatment. While the lesion image appears much smaller on the ge3d MR image than in either prediction it does at least show two distinct sections. These appear at similar positions to the two areas of cavitation activity in passive maps, that appear slightly more distinctly in the PAM-derived thermal dose than in the MR-thermometry-derived dose.

Figure 5.29 shows two experiments where the PAM-derived prediction does not match the MR estimate of cavitation-enhanced heating. The experiment in figure5.29 (a),(b) was conducted at 6 MPa PNFP. In this experiment, there appears to be multiple areas of extra heating in the MR thermometry in the region between 57 and 64mm in the z direction. In figure 5.29 (c),(d), conducted at 4.5 MPa PNFP, the temperature rise is modelled well up to 13s, then the MR thermometry temperature

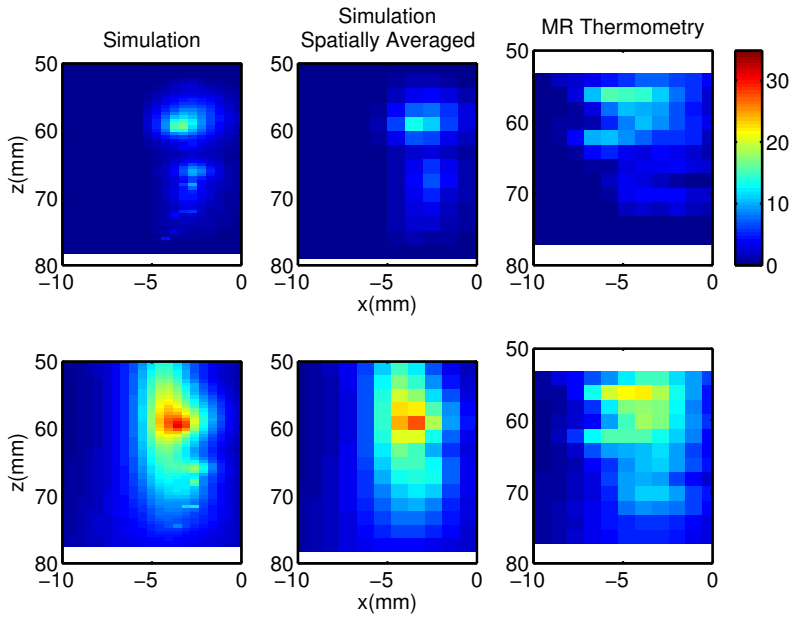

(a)

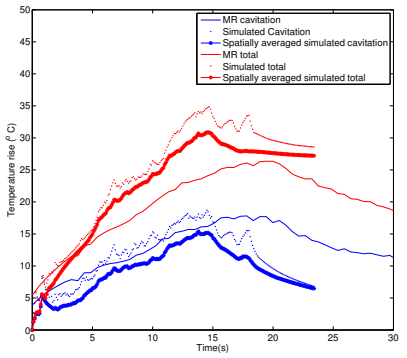

(b)

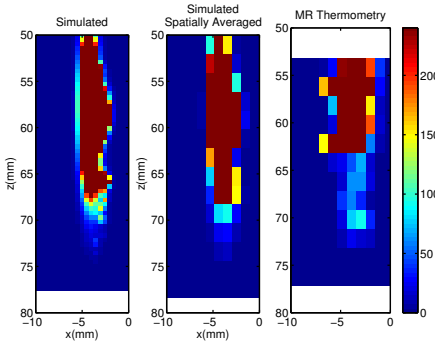

(c)

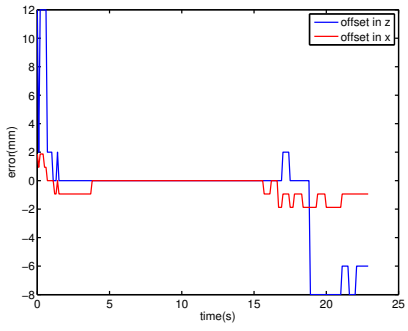

(d)

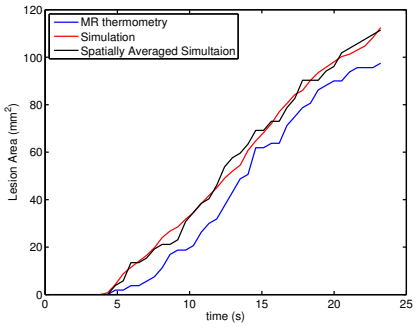

(e)

Figure 5.26: (a) the cavitation-enhanced heating and the total heating at 14s, (b) measured and predicted focal temperatures (c) the estimated thermal dose for the two methods, (d) the distance between the location of the maximum temperature in the two methods and (e) the estimated lesion area for the duration of the cavitation.

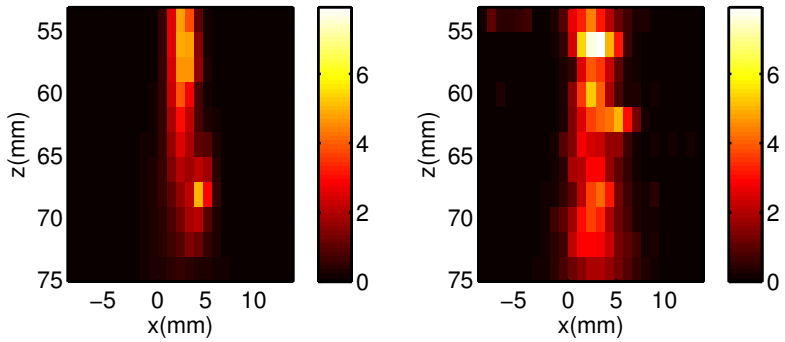

Figure 5.27: (a) estimated temperature and (b) MR thermometry for two frames at 1.1s in the experiment shown in figure 5.26. The reason for the large discrepancy in the position of the hottest pixel in figure 5.26 (d) is that there are two regions of cavitation-enhanced heating at similar temperatures in the simulation, even though each cavitating region is at the correct position.

overtakes the PAM temperature prediction.

In figure 5.29 the reasons for these discrepancies appear to be due to the MR thermometry. For the experiment in figure 5.29 (a),(b) there is an inhomogeneity in the magnitude image of the tissue, possibly a blood vessel or bile duct, that is giving off a very small signal compared to the rest of the tissue. This is shown clearly in figure 5.30, where the magnitude image of the tissue in figure 5.29 (a),(b) is compared with the magnitude image from the tissue in the experiment shown in figure 5.25 at the same location. Small magnitudes make the phase measurements more susceptible to noise, and can lead to spurious temperature rises. The position of the inhomogeneities in figure 5.30 coincide with the position of the apparent temperature increases absent in PAM estimates in figure 5.29 (a), (b).

In the second experiment (figure 5.29 (c) and (d)) one pixel in the image becomes apparently much hotter than the others surrounding it after 13s. The high temperature gradient suggests that this single pixel is an anomaly, caused either by poor signal to noise ratio (signal to noise ratio decreases as the temperature increases) or by faulty phase unwrapping. Once this pixel is removed, the maximum heating

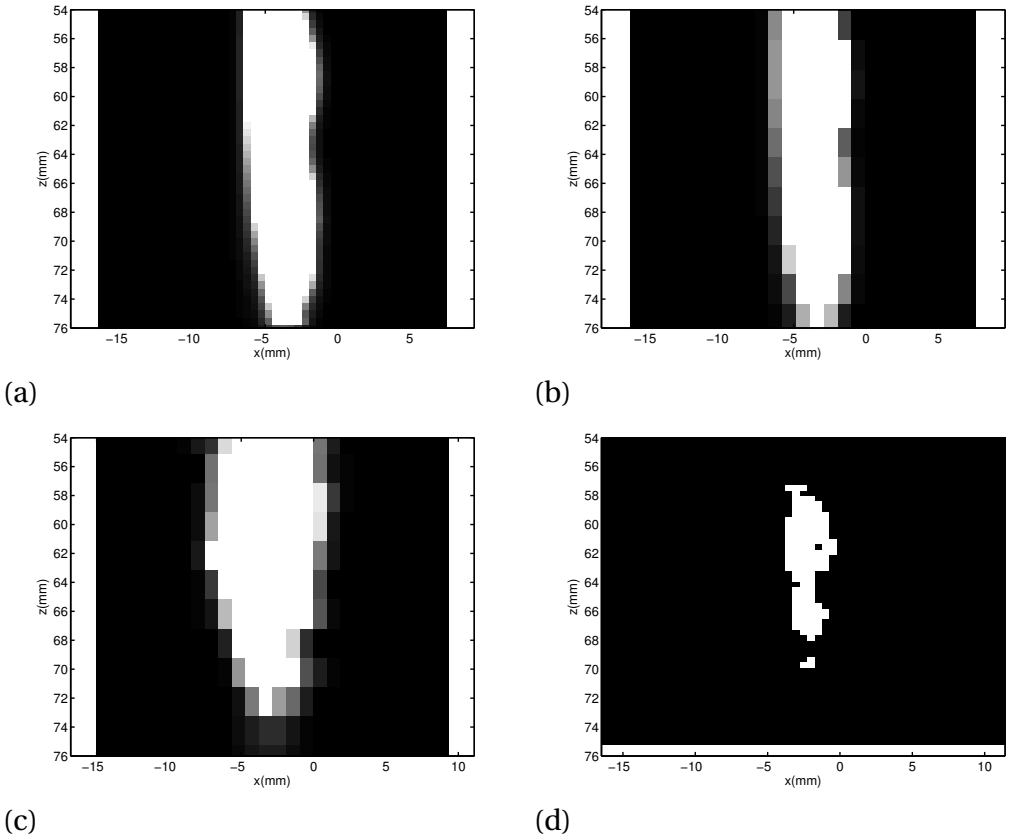

Figure 5.28: Thermal dose derived estimates of lesion size for (a) PAM-derived thermal simulation, (b) PAM-derived spatially averaged thermal simulation, (c) MR thermometry and (d) MR ge3d images of a lesion. Although the CEM prediction is larger than the lesion appears in the MR image in (d), the PAM simulation appears to capture the morphology of the lesion being split into two large sections, probably caused by cavitation, linked by a 'background' lesion caused by the incident HIFU.

curve is much improved as shown in figure 5.31.

In the final three experiments shown in figure 5.32, all performed at 4.5MPa PNFP, the PAM estimation also failed to match the MR estimate of cavitation-enhanced heating. In all three of these cases the PAM estimation initially significantly overestimates the temperature rise. In figure 5.32 (a),(b) an initial spike in the PAM estimate of temperature does not appear in the passive map, and the subsequent area of enhanced heating is not as large in the z direction in the PAM estimation as in the MR thermometry estimate. In figure 5.32 (c),(d) the PAM estimate

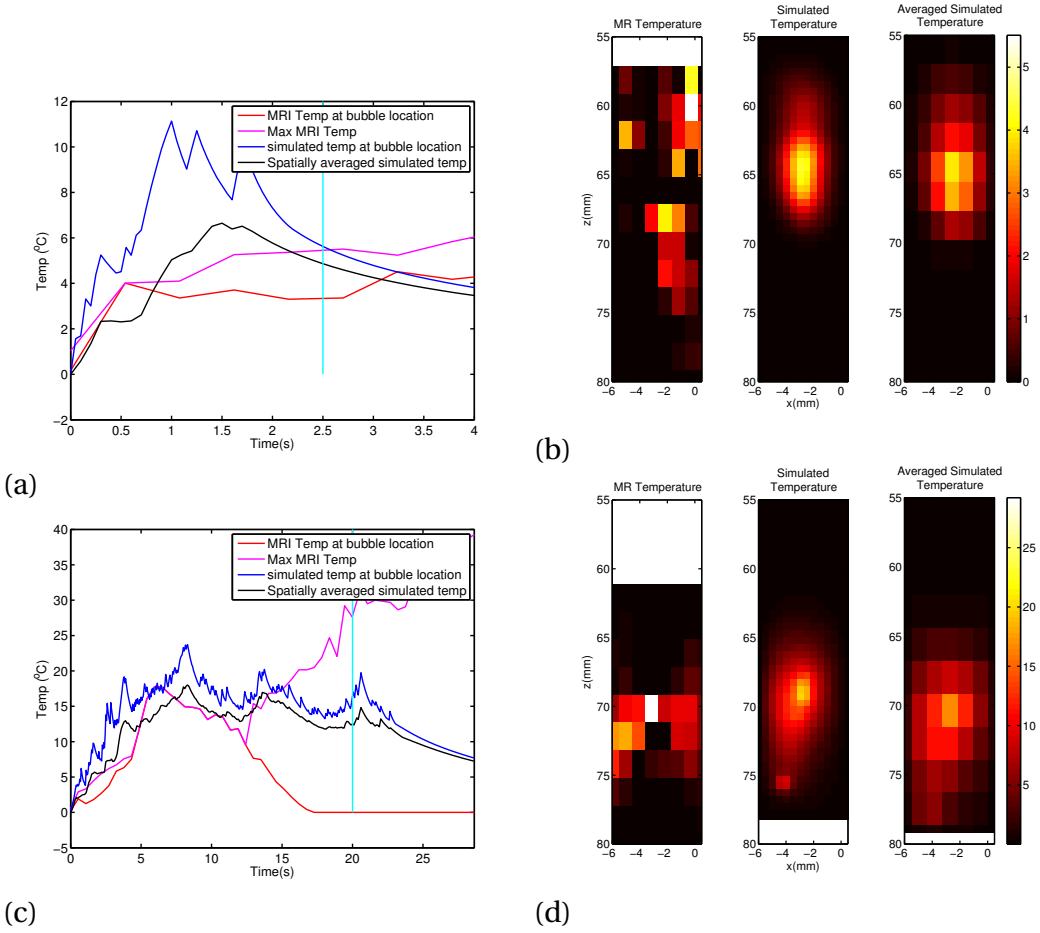

Figure 5.29: Two experiments with partially successful PAM-derived estimates of temperature rise. the experiment in (a),(b) was conducted at 6 and (c),(d) was conducted at 4.5MPa PNFP. (a),(c) show temperature over time for MR estimates of cavitation-enhanced heating for the duration of the cavitation, and (b) and (d) show the spatial extent of the heating, taken at the time indicated by the cyan vertical lines in the (a) and (c) respectively. In these exposures, the method is able to match the degree of temperature rise to an extent, but the enhanced temperature rise does not occur in the correct location.

overestimates the enhanced MR estimated temperature rise until another outlier voxel appears to increase the temperature significantly after 16s. In figure 5.32 (e),(f) while the PAM estimate of enhanced heating occurs at the correct location in the tissue, and captures two separate bouts of cavitation-enhanced heating during the exposure, it initially overestimates then underestimates the degree of heating compared with the MRI measurement. Possible reasons for these three unsuccessful

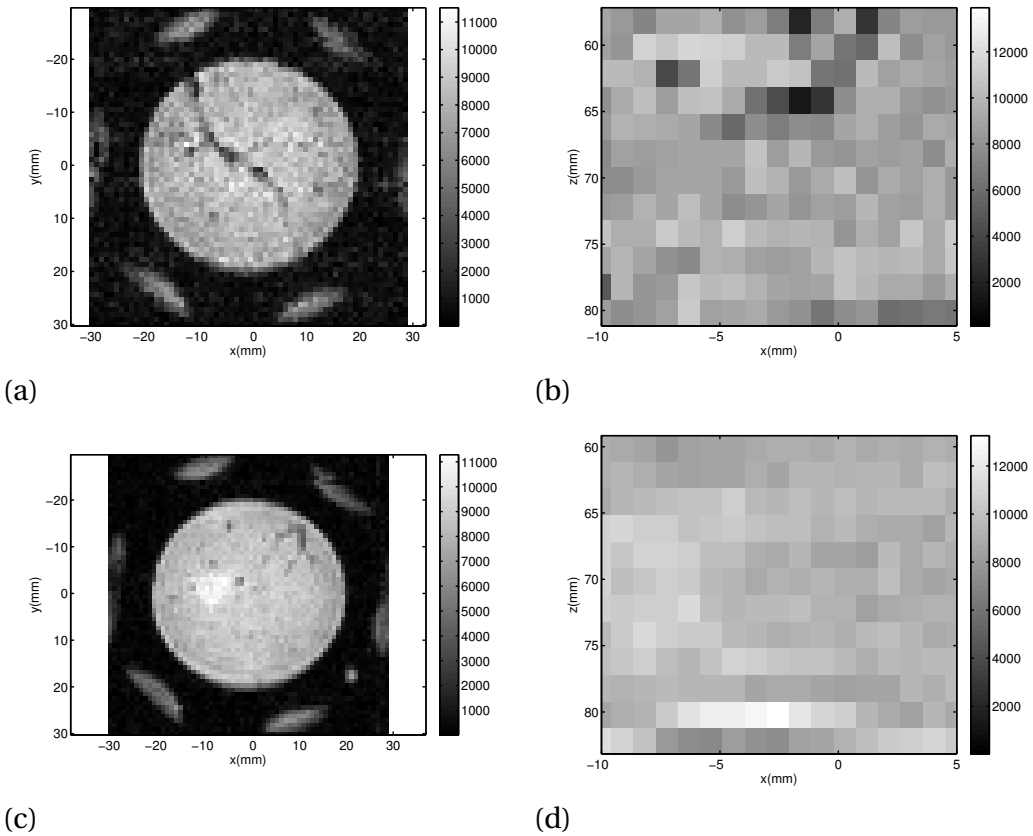

Figure 5.30: (a),(b)EPI magnitude images showing the presence of an inhomogeneity in the tissue in 5.29 (a),(b). These are compared with images of the tissue taken in the same location from the experiment in 5.25 shown in (c,d). The presence of the inhomogeneity is shown very clearly in the x, y plot in (a). Although the plot of the same location in (c) shows some inhomogeneities, the lack of signal is not as extreme, and they do not occur at the focus. (b) and (d) show x, z plots. The inhomogeneity is still visible in (b), and occurs at the same location as the apparent temperature rises in the MR thermometry.

experiments are discussed in section 5.4.

5.4 Discussion

Overall, the PAM-based temperature estimation method provided reasonable estimates of temperature and predicted lesion size four times out of nine. The four successful exposures in section 5.3.2.1 show that the method is capable of matching the

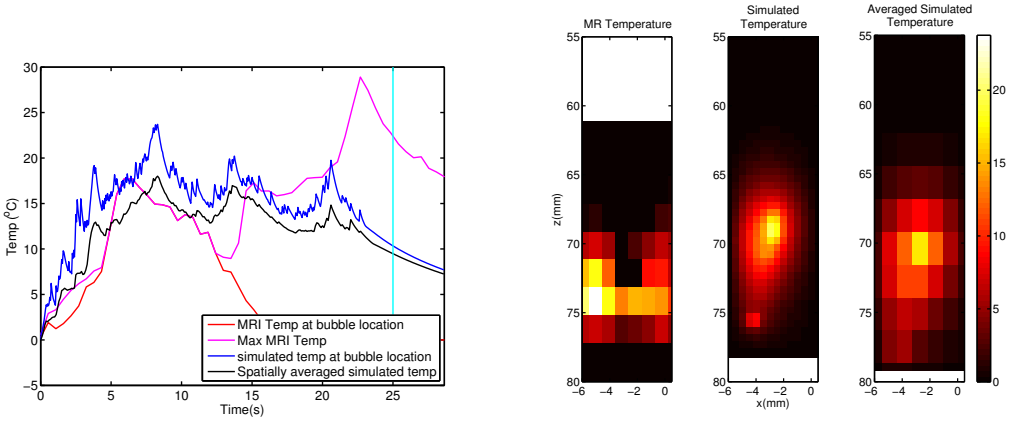

(a) (b)

Figure 5.31: The same data as in figure 5.29 (c) and (d) except with the hottest pixel in the MR thermometry image removed, giving much better agreement between the two methods.

temperature rise and spatial extent of heating. The maximum temperature rise in both methods agrees well, the shape of the heating and cooling curves is similar, and the centre of heating in both images is in the same location. The shape of the enhanced heating is also similar, this can be seen especially in figure 5.23 (f). Here two separate regions of cavitation-enhanced heating are seen in both the maps and the MR thermometry images, with locations and relative temperature rises both captured well by the PAM-derived method. The shape of the predicted lesions is also similar, and particularly in figure 5.26 the growth of the lesions is captured well.

One of the most obvious differences in all of the simulations, is that the maximum temperature is much higher before spatial averaging is taken into account. As seen in figure 5.24 a lesion has begun to form in the simulation, but in the dose calculated from the spatially averaged simulation no lesion has begun to form. In ablation a false negative result will lead to overtreatment. In cases where thermal damage is to be avoided, and MR thermometry is used for monitoring, if cavitation is possible, localised high temperature rises due to cavitation may be missed without simultaneous cavitation monitoring.

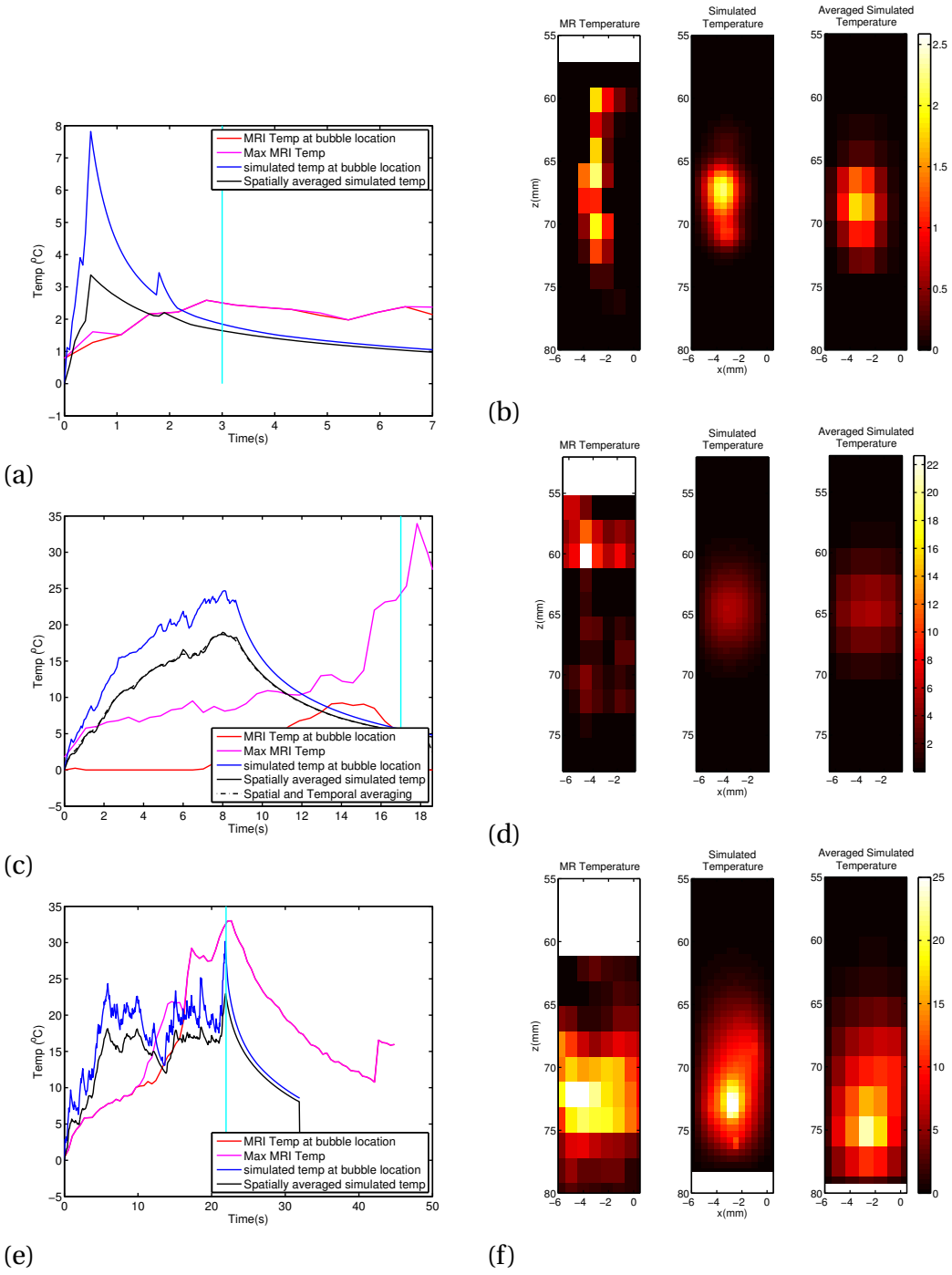

Figure 5.32: Unsuccessful PAM-derived estimates of temperature rise, all conducted at 4.5MPa PNFP. In (a),(b), there is a spike in the PAM heating estimates that is not present in the MR thermometry images. In (c),(d) the enhanced heating is in the wrong location and overestimates the initial cavitation-enhanced temperature rise. In (e),(f) the method initially overestimates, then underestimates the degree of enhanced heating.

However, even for the four successful cases there were errors on the order of 70% of the cavitation-enhanced temperature rise between corresponding pixels. Before discussing the three unsuccessful experiments, the reasons for the large errors are considered. There are a number of causes behind these large errors, discussed below.

Regarding the temporal resolution of the MR thermometry, the effective frame rate is the repetition time, TR. For these experiments TR=0.54s, and during this time all 12 z slices are updated one z slice at a time. This means that the temperature in each slice is updated once every 0.54s, but is averaged over 0.045s. There is therefore slight temporal averaging, but also the problem of which point in the simulation corresponds to which exact point in the MR thermometry. In these experiments there is no mechanism synchronisation between the PAM and the MR thermometry, this was estimated by matching the start and end of the HIFU exposures. The result of this is potential errors such as the one in figure 5.23 (c), also shown in figure 5.25. Here, a very short burst of cavitation can increase the temperature, and then cool, in between two MRI samples.

The spatial resolution of the passive mapping also deteriorates as distance from the imaging transducer increases. This has the effect of turning a point source into a larger region in maps. When dealing with a cloud of cavitating bubbles this can make it difficult for the closed contour algorithm to find distinct peaks, instead finding the peak of the 'smudge' of points. This puts the heating at the wrong location, and can lead to large pixel-to-pixel errors between the two methods. In the present experiment the distances are limited by the dimensions of the MR scanner. In a different scanner using a larger imaging transducer or being able to place the imaging transducer closer to the Zonare would mitigate this problem.

Out of the five less successful cases, the two shown in figure 5.29 both have issues

with MR thermometry that makes MR thermometry derived estimates of enhanced temperature rise less reliable, either due to inhomogeneities in the tissue giving off an unusually low magnitude signal (a,b) or a single pixel with an unrealistically high apparent temperature (c,d).

However, in the three unsuccessful cases shown in figure 5.32 there were no obvious inhomogeneities in the magnitude images and only in the final 2 seconds of the exposure in 5.32(c,d) was there one pixel apparently much hotter than the others. Apart from this the MRI estimates appear to be reasonable, so why might the PAM estimates have failed to model the temperature rise?

In figure 5.32 (a,b) there was a sharp, short-lived temperature rise in the PAM heating simulation that does not appear in the MR thermometry estimate. Although short-lived, it is not so short lived that it could have been completely missed by the MR thermometry undersampling. In 5.32 (c,d) until the final two seconds the MR temperature estimates remain reasonable. Here again, the PA< simulations overestimate the MR estimate of temperature rise. In 5.32 (e,f) the PAM simulation appeared to overestimate then underestimate the temperature rise in two separate bouts of cavitation-enhanced heating.

However, in general in all three experiments the passive mapping is overestimating the heating considerably. This is very dangerous in terms of ablation monitoring as it would lead to undertreatment. These overestimates occur when the cavitation is occurring deeper into the tissue. The tissue-water boundary occurs at 50mm, and in these experiments the cavitation is occurring at 65-70mm rather than 55-60mm. This doubles or triples the distance over which attenuation must be accounted for. This will amplify any errors in attenuation, either the attenuation coefficient or the frequency dependence of attenuation.

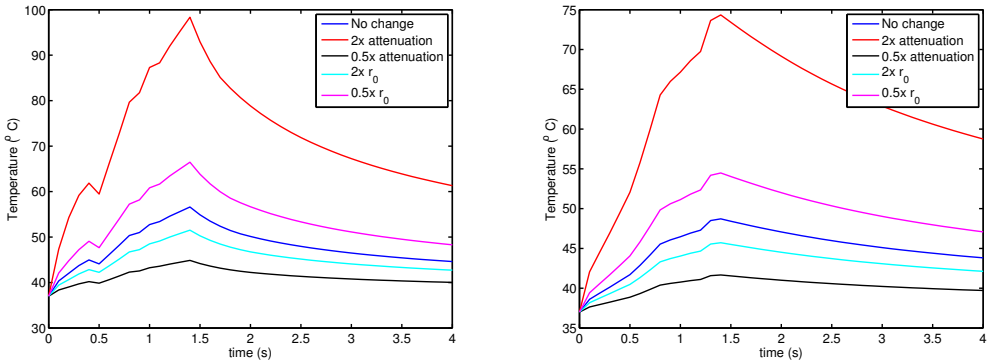

(a) (b)

Figure 5.33: The effect of changing attenuation and bubble size on the heating simulation results (a) before and (b) after spatial averaging. The dark blue line shows the heating curve for the unchanged values, the other curves show the effects of doubling and halving the attenuation/absorption coefficient and the bubble radius.

This relates to one of the fundamental drawbacks of any scheme that tries to back-propagate an acoustic field in an attenuating medium, and then use the acoustic field to estimate heating, which is a high degree of sensitivity to acoustic and thermal properties of tissue, particularly the exponential gain associated with inverting attenuation. As seen in chapter 2 there is large variability in acoustic properties between different samples and within the same sample. The results are also susceptible to the estimate of bubble size, the calibration of the imaging transducer, and the thermal properties of tissue. However, for real patients these properties are difficult to measure in advance, the values for acoustic properties were kept as 'reference' properties, without being adjusted for each individual experiment.

Figure 5.33 shows how the predicted temperature varies when either the attenuation or bubble radius changes by a factor of two. The predicted temperature rise varies by more than 50 °C. Although this effect is slightly smaller after spatial averaging is taken into account, the change in temperature rise is still 35°C.

Even a small variation in either attenuation or bubble size has a large effect on

the results, and changes in these values could improve the match between MR and PAM-derived estimates. In figure 5.33 (e,f) the PAM method initially underestimates then overestimates the temperature rise. This could be due to the changing acoustic properties, although these changes are more pronounced after tissue has cooled, and there is no noticeable increase in the rate of heating in cavitation-free exposure where lesions are caused. In this case, where there are two clear separate bouts of cavitation, this might mean that different bubble sizes in each cavitation even caused the overestimation then subsequent underestimation.

5.5 CONCLUSIONS

In this chapter a method for estimating cavitation-enhanced heating from passive maps has been described, and applied to experiments monitored with simultaneous PAM and MRI. The method is able to produce estimates of the spatial extent of total heating and cavitation-enhanced heating that can agree spatially and temporally with MR-thermometry measurements. When added to thermal simulations of primary HIFU heating the estimates agree with MR-predicted lesion sizes. However, the method fails to reliably match the degree of measured heating. While some of these cases are due to inconsistencies in MR thermometry readings, the method as a whole is very dependent on accurate knowledge of tissue properties, especially attenuation.

CHAPTER 6

CONCLUSIONS AND FUTURE WORK

High intensity focused ultrasound is a promising noninvasive therapy that has many applications, from enhancing drug delivery, to thermal ablation. For thermal ablation, uptake of HIFU has been held back by the need for effective and affordable real-time monitoring of treatment, and accurate treatment planning. In both of these cases, nonlinear acoustic phenomena have a role to play, for example through nonlinear propagation at high intensities or through cavitation-enhanced heating. The aim of this thesis has been to investigate both of these phenomena in order to improve HIFU treatment monitoring and modelling.

6.1 NONLINEAR ACOUSTIC PROPERTIES

In chapter 2 changes in the nonlinear parameter B/A, speed of sound and attenuation of bovine liver during a heating/cooling cycle that mirrored a HIFU ablation treatment were reported. Very few previous measurements existed for measuring B/A of ex vivo tissue over this range of temperatures, and only one measured the

temperatures on cooling as well as heating, enabling the separate effects of temperature rise and denaturation to be taken into account. The existing studies suggested that a large change in B/A occurred, that would have a large effect on treatment monitoring and even the potential for treatment monitoring based on backscattered nonlinear emissions from tissue.

To investigate these properties a new development on the finite amplitude method was used to measure the nonlinear acoustic properties of ex vivo bovine liver. Using the very near field of a large single element transducer as a plane wave source and a smaller calibrated broadband transducer as a receiver, the method was able to match existing measurements of B/A for water and ex-vivo bovine liver at 37°C. In addition, attenuation measurements were taken at the same location as the B/A measurements without any movement of the apparatus, meaning that local variation in attenuation did not affect B/A measurements.

Over the heating/cooling cycle the method captured the expected changes in speed of sound and attenuation- a slight increase in sound speed with temperature and no large change with denaturation, a slight initial decrease in attenuation with temperature before a large increase (approx 100%) with denaturation. These measurements are in good agreement with the existing literature.

For B/A the method measured an increase with temperature before denaturation that is within existing literature estimates for temperature. For denatured tissue no significant change in B/A was observed. This suggests that monitoring HIFU using changes in the nonlinear coefficient of tissue is not feasible, and from a treatment planning and modelling point of view suggests that (a) changes in attenuation are the most important acoustic property to capture correctly after denaturation and (b) that temperature is more important the state of denaturation of the tissue for modelling B/A during a HIFU ablation treatment, in the same way as for mod-

elling speed of sound.

6.2 Comparing Nonlinear Models

In most HIFU treatments high intensity focused fields generate significant nonlinearity that plays a large role in the treatment outcomes, especially heating. In this chapter two modelling techniques were compared: the KZK equation and the commercial PZFlex modelling software. Both of these methods were compared with hydrophone measurements of nonlinear focused fields at a range of frequencies and pressures.

The results show that in general, PZFlex underestimated the harmonics generated by the HIFU transducers. There was much better agreement between the hydrophone measurements and the KZK simulations for the fundamental frequency and the second and third harmonics. Additionally, the higher harmonics in the KZK simulation centred around the geometric focus and became narrower as the harmonics number increased. This was in contrast to the higher harmonics in the PZFlex simulation which did not necessarily peak at the focus and at higher harmonics followed the shape of the field at the fundamental frequency. The discrepancy between the two methods increased with source pressure and frequency, with frequency having the largest effect. For high intensity fields at frequencies above 1MHz, PZFlex was not found to be a good model for nonlinear propagation.

6.3 Combining PAM and MR Thermometry

In chapter 4 a system capable of simultaneously performing MR thermometry and passive acoustic mapping for monitoring HIFU treatments of ex-vivo tissue was developed. The combination of MR thermometry and passive acoustic mapping is

particularly useful as the two methods are able to provide complementary information for non-thermal exposures where cavitation is present. It was shown that the two methods are compatible, and that the interference between the two methods can be compensated for.

In the absence of cavitation the focus of the HIFU transducer was visible on passive maps by looking at the harmonics of the HIFU. Harmonics generated due to nonlinear propagation occurred strongest at the focus and map to this location. The focus of the transducer in the maps coincided with the centre of heating in the MRI thermometry images confirming the validity of the registration. In this orientation the focus was visible due to the incident ultrasound, but the same technique could be applied with confocally aligned transducers. This provides a completely non-thermal way of visualising the location of the focus on MR images.

For short, non-thermal exposures above the cavitation threshold there was visible cavitation on passive maps but no change in MR images. This is because cavitating bubbles only change the water fraction of the insonated tissue by a tiny amount, and so do not appear on MR images, yet give a very strong acoustic response. For non-thermal HIFU applications such as cavitation-enhanced drug delivery this is very important, as here only PAM can give information about the process driving the drug delivery, while MR can give complementary information, for example about the location of the drug itself if it is MR labelled.

For thermal exposures above the cavitation threshold there was broadband noise in passive acoustic maps that correlated spatially with clear spikes in heating in the MR thermometry. The broadband noise showed the location and strength of inertially cavitating bubbles which lead to cavitation-enhanced heating visible in MR thermometry. Although there was only reasonable spatial agreement between MR thermometry images and passive maps processed with time exposure acous-

tics, there was very good agreement when the maps are reprocessed using the Robust Capon beamformer algorithm. Maps processed with time exposure acoustics suffered from a pronounced artefact beyond the focus of the imaging transducer. The Robust Capon beamformer uses optimal beamforming techniques to reduce this by assigning optimised weights to the individual traces. In addition to improving the registration between passive maps and MR images, this provides a powerful tool for analysing the relationship between inertial cavitation acoustic signals and enhanced heating.

6.4 Monitoring Cavitation-Enhanced Heating with MR Thermometry and Passive Acoustic Mapping

From the recorded PAM data a back-propagation was devised to estimate the heat input to a thermal simulation from a cavitation dose. It was shown that it was possible to produce temperature estimates that matched the temperature rise measured using MR thermometry particularly once spatial averaging was taken into account. From the thermal dose, estimates of lesion size were also shown to be in reasonable agreement with the dose calculated from MR measurements, although the maximum error between any two corresponding pixels in the estimates was quite large, and the estimation method was not successful in every case. It was found that the predictions using this method were very sensitive to changes in acoustic properties of tissue, especially attenuation. Recall from chapter 2 that these properties vary from tissue to tissue, and within tissue samples. This makes the accuracy of the temperature estimates dependent on the accuracy of the knowledge of all the tissue properties. One way of improving the method might be from applying low intensity

pulses to achieve mild heating beneath the threshold for damage that could be used to calibrate the system, either using MR thermometry if available or using other techniques such as thermal imaging.

6.5 Future Work

There is scope to expand on the work of this thesis. Regarding the measurements of tissue properties one important question to be answered is whether the properties of lesions created with ultrasound are different from the properties of tissue thermally denatured using a water bath. Initially, a lesion large enough so that the entire tissue in between the source and measurement transducer should be created by multiple HIFU exposures, and this tissue then measured at a range of temperatures. To measure B/A throughout the creation of the lesion would require a system capable of applying ablation levels of ultrasound to the section of tissue in between the source and measurement transducers. This should include a method of monitoring the temperature of the ultrasound in real time to determine the thermal dose and predict the size of the lesion.

Additionally, while measurements of healthy tissue is important, there is also a need for measurements of cancerous tissue and tumours, although this depends on the availability of tissue samples that are much harder to obtain than samples from abattoirs. Another important distinction is the difference in properties of in vivo as opposed to ex vivo tissues. In ex vivo tissue blood has been replaced by PBS, and the tissue has been de-gassed. The difference in the dissolved gas concentration of the two tissue types increases the probability of cavitation in in vivo tissue, and may have an effect on other acoustic properties.

Including the temperature-dependent acoustic properties into the thermal sim-

ulations for estimating temperature rise should enhance the accuracy of the PAM-derived estimates, by decreasing the attenuation and increasing the B/A of heated tissue and increasing the attenuation of treated tissue.

Regarding the modelling and simulation methods it would be useful to test a larger range of potential methods for modelling nonlinear ultrasound fields. It would also be possible to add a larger range of criteria to judge them against, in order to determine which code would be more suitable for modelling different applications. For example, although PZFlex was unreliable at modelling nonlinear fields at 3.3MHz, in comparison with the KZK simulations, it does not rely on the paraxial approximation and is therefore suitable for modelling a larger range of source geometries. Other codes may be more accurate in the near field, or in the far field, for example, the Westervelt equation is a second order wave equation that captures attenuation, diffraction and nonlinear effects, without making the paraxial approximation (Hamilton, L., and Blackstock, 1998b). In the measurements of tissue properties conducted in the previous chapter it was shown that tissue is inhomogeneous and has properties that vary from location to location. An improvement to any code that calculates nonlinear fields in tissue would be easy functionality to assess the impact tissue inhomogeneities might have on the field.

The largest scope for further work is the development of the combined MR thermometry/passive mapping system. There are many limitations on what is achievable due to the specific constraints of the small-bore MR scanner in this work. A larger bore scanner would enable the use of a more standard PAM setup, where the imaging transducer is embedded within the therapeutic transducer. This would suppress the interference from the incident HIFU, and allow for harmonic bubble oscillations to be taken into consideration as well as those emitting broadband noise. Ignoring the harmonics in the signal could lead to missing a potential

source of cavitation-enhanced heating. Different spectral content in bubble oscillations leads to different therapeutic effects and treatment outcomes, with broadband emissions more commonly associated with heating, and harmonic emissions associated with enhancing cell permeability. In therapeutic applications other than heating, harmonic emissions can be more important to capture than broadband emissions.

A larger scanner would also allow the development of experiments that modelled a wider range of therapies, such as flow phantoms. These are capable of modelling drug delivery treatments, an example of non-thermal treatments where cavitation plays a key role in the treatment, but does not contribute significant heating. Adding MR contrast agents to the drugs would allow simultaneous tracking of the drugs from MR images, and information about the process driving drug delivery, from passive maps. This would be a very important area for combined cavitation and MR monitoring, as well as experiments involved in disrupting the blood-brain barrier. In these experiments rather than providing the same information, as they do in cavitation-enhanced thermal ablation, the complementary information provided by the two methods about the cavitation driving the treatment and the location of the drug is unable to be obtained any other way.

Another improvement is to match the 3-D MR images with 3-D passive maps. Producing 3-D passive maps requires a 2-D array, and an expanded beamforming algorithm, and this has been achieved (Collin et al., 2013). Combining 3-D passive mapping would eliminate the uncertainties caused by out of plane cavitation events, and would be able to provide an estimate of lesion volume rather than of lesion area.

BIBLIOGRAPHY

Adams, M. T. et al. (2014). "Thermal dose dependent optical property changes of ex vivo chicken breast tissues between 500 and 1100 nm". In: *Physics in medicine and biology* 59.13, p. 3249.

Allen, S. P. et al. (2015). "Controlling cavitation-based image contrast in focused ultrasound histotripsy surgery". In: *Magnetic Resonance in Medicine* 73.1, pp. 204–213.

Ames, W. F. (1992). "Numerical Methods for Partial Differential Equations". In: Academic Press. Chap. 5, pp. 351–354.

Anand, A. (2004). "Monitoring formation of high intensity focused ultrasound (HIFU) induced lesions using backscattered ultrasound". In: *Acoustics Research Letters Online* 5.3, p. 88.

Arthur, R. et al. (2005). "Non-invasive estimation of hyperthermia temperatures with ultrasound". In: *International journal of hyperthermia* 21.6, pp. 589–600.

Arvanitis, C. D., M. S. Livingstone, and N. McDannold (2013). "Combined ultrasound and MR imaging to guide focused ultrasound therapies in the brain". en. In: *Physics in Medicine and Biology* 58.14, p. 4749.

Arvanitis, C. D. and N. McDannold (2011). "Simultaneous temperature and cavitation activity mapping". In: pp. 128–131.

Azuma, T. et al. (2005). "Radiation force imaging for detection of irreversible changescaused by high intensity fo-

cused ultrasound therapy". In: 2, pp. 1245 –1248.

Bacon, D. R. and A. Shaw (1993). "Experimental validation of predicted temperature rises in tissue-mimicking materials". In: *Physics in medicine and biology* 38.11, p. 1647.

Bailey, M. R. et al. (2001). "Use of overpressure to assess the role of bubbles in focused ultrasound lesion shape< i> in vitro</i>". In: *Ultrasound in medicine & biology* 27.5, pp. 695–708.

Bailey, M. et al. (2003). "Physical mechanisms of the therapeutic effect of ultrasound (a review)". In: *Acoustical Physics* 49.4, pp. 369–388.

Bamber, J. et al. (1999). "Ultrasound elasticity imaging: definition and technology". In: *European radiology* 9.3, S327.

Bazan-Peregrino, M. et al. (2013). "Cavitation-enhanced delivery of a replicating oncolytic adenovirus to tumors using focused ultrasound". In: *Journal of Controlled Release* 169.1, pp. 40–47.

Bever, J. de et al. (2014). "Adaptive model-predictive controller for magnetic resonance guided focused ultrasound therapy". In: *International Journal of Hyperthermia* 30.7, pp. 456–470.

Beyer, R, M Hamilton, and D Blackstock (1998a). "Nonlinear Acoustics". In: Academic Press. Chap. 2, pp. 26–27.

Beyer, R, M Hamilton, and T Blackstock (1998b). "Nonlinear Acoustics". In: Academic Press. Chap. 2, p. 34.

Bhatnagar, S., H. Schiffter, and C.-C. Coussios (2014). "Exploitation of Acoustic Cavitation-Induced Microstreaming to Enhance Molecular Transport". In: *Journal of pharmaceutical sciences* 103.6, pp. 1903–1912.

Bhattacharya, A and R. Mahajan (2003). "Temperature dependence of thermal conductivity of biological tissues". In: *Physiological measurement* 24.3, p. 769.

Blackstock, D. T. (1998). "Nonlinear Acoustics". In: Academic Press. Chap. 4, pp. 71–72.

Breen, M. S. et al. (2007). "MRI-guided thermal ablation therapy: Model and parameter estimates to predict cell death from MR thermometry images". In: *Annals of biomedical engineering* 35.8, pp. 1391–1403.

Brown, R. W. et al. (2014). "Magnetic resonance imaging: physical principles and sequence design". In: John Wiley & Sons. Chap. 10, pp. 184–193.

Burov, A and G Andreevskaya (1956). "The effect of ultra-acoustic oscillation of high intensity on malignant tumors in animals and man". In: *Dokl Akad Nauk SSSR*. Vol. 106, pp. 445–8.

Bush, N. et al. (1993). "Acoustic properties of lesions generated with an ultrasound therapy system". In: *Ultrasound in Medicine & Biology* 19.9, pp. 789–801. (Visited on 06/01/2012).

Canney, M. S. et al. (2008). "Acoustic characterization of high intensity focused ultrasound fields: A combined measurement and modeling approach". In: *The Journal of the Acoustical Society of America* 124.4, pp. 2406–2420. (Visited on 06/04/2014).

Canney, M. S. et al. (2010). "Shock-induced heating and millisecond boiling in gels and tissue due to high intensity focused ultrasound". In: *Ultrasound in medicine & biology* 36.2, pp. 250–267.

Carlisle, R. et al. (2013). "Enhanced Tumor Uptake and Penetration of Virotherapy Using Polymer Stealthing and Focused Ultrasound". In: *Journal of the National Cancer Institute*. eprint: http://jnci.oxfordjournals.org/content/early/2013/10/25/jnci.djt305.full.pdf+html.

Carstensen, E. et al. (1981). "Finite amplitude effects on the thresholds for lesion production in tissues by unfocused ultrasound". In: *The Journal of the Acoustical Society of America* 70.2, pp. 302–309.

Chapelon, J. et al. (1999). "Treatment of localised prostate cancer with transrectal high intensity focused ultra-

sound". In: *European journal of ultrasound* 9.1, pp. 31–38.

Chavrier, F. (2006). "Determination of the nonlinear parameter by propagating and modeling finite amplitude plane waves". In: *Acoustical Society of America Journal* 119, p. 2639. (Visited on 06/05/2012).

Chen, L et al. (1993). "Histological changes in rat liver tumours treated with high-intensity focused ultrasound". eng. In: *Ultrasound in medicine & biology* 19.1, pp. 67–74.

Chen, L. et al. (1999). "Study of focused ultrasound tissue damage using MRI and histology". en. In: *Journal of Magnetic Resonance Imaging* 10.2, pp. 146–153. (Visited on 12/17/2013).

Choi, M. J. et al. (2011). "Changes in Ultrasonic Properties of Liver Tissue In Vitro During Heating-Cooling Cycle Concomitant with Thermal Coagulation". In: *Ultrasound in Medicine & Biology* 37.12, pp. 2000–2012. (Visited on 06/01/2012).

Clarke, R., N. Bush, and G. Ter Haar (2003). "The changes in acoustic attenuation due to in vitro heating". In: *Ultrasound in Medicine & Biology* 29.1, pp. 127–135. (Visited on 06/01/2012).

Cline, H. E. et al. (1992). "MR-guided focused ultrasound surgery". In: *Journal of computer assisted tomography* 16.6, pp. 956–965.

Collin, J. et al. (2013). "Real-time three-dimensional passive cavitation detection for clinical high intensity focussed ultrasound systems". In: 19.1, p. 075023.

Coussios, C. C. and R. A. Roy (2008). "Applications of Acoustics and Cavitation to Noninvasive Therapy and Drug Delivery". In: *Annual Review of Fluid Mechanics* 40.1, pp. 395–420. (Visited on 06/01/2012).

Coussios, C. C. et al. (2007). "Role of acoustic cavitation in the delivery and monitoring of cancer treatment by high-intensity focused ultrasound (HIFU)". In: *International Journal of Hyperthermia* 23.2, pp. 105–120.

Coviello, C. et al. (2013). "Passive acoustic mapping using optimal beam-

forming for real-time monitoring of ultrasound therapy". In: *Proceedings of Meetings on Acoustics*. Vol. 19. 1. Acoustical Society of America, p. 075024.

Coviello, C. M., S. R. Faragher, and C.-C. Coussios (2010). "Robust Capon beamforming for passive cavitation mapping during high-intensity focused ultrasound therapy." In: *The Journal of the Acoustical Society of America* 128.4, pp. 2280–2280.

Curiel, L. et al. (2005). "Elastography for the follow-up of high-intensity focused ultrasound prostate cancer treatment: Initial comparison with MRI". In: *Ultrasound in Medicine & Biology* 31.11, pp. 1461–1468. (Visited on 12/18/2013).

Curiel, L. and K. Hynynen (2011). "Localized harmonic motion imaging for focused ultrasound surgery targeting". In: *Ultrasound in medicine & biology* 37.8, pp. 1230–1239.

Curra, F. P. et al. (2000). "Numerical simulations of heating patterns and tissue temperature response due to high-intensity focused ultrasound". In: *Ultrasonics, Ferroelectrics and Frequency Control, IEEE Transactions on* 47.4, pp. 1077–1089.

Dalecki, D. et al. (1991). "Absorption of finite amplitude focused ultrasound". In: *The Journal of the Acoustical Society of America* 89.5, pp. 2435–2447.

Damianou, C. A., K. Hynynen, and X. Fan (1995). "Evaluation of accuracy of a theoretical model for predicting the necrosed tissue volume during focused ultrasound surgery". In: *Ultrasonics, Ferroelectrics and Frequency Control, IEEE Transactions on* 42.2, pp. 182–187.

Datta, S. et al. (2006). "Correlation of cavitation with ultrasound enhancement of thrombolysis". In: *Ultrasound in medicine & biology* 32.8, pp. 1257–1267.

De Poorter, J (1995a). "Noninvasive MRI thermometry with the proton resonance frequency method: study of susceptibility effects". eng. In: *Magnetic resonance in medicine: official journal of the Society of Magnetic Res-*

onance in Medicine / Society of Magnetic Resonance in Medicine 34.3, pp. 359–367.

De Poorter, J (1995b). "Noninvasive MRI thermometry with the proton resonance frequency method: Study of susceptibility effects". en. In: *Magnetic Resonance in Medicine* 34.3, pp. 359–367. (Visited on 04/09/2014).

Dewhirst, M. et al. (2003). "Basic principles of thermal dosimetry and thermal thresholds for tissue damage from hyperthermia". In: *International Journal of Hyperthermia* 19.3, pp. 267–294.

Dong, F. et al. (1999). "Nonlinearity parameter for tissue-mimicking materials". In: *Ultrasound in Medicine & Biology* 25.5, pp. 831–838. (Visited on 06/05/2012).

Draudt, A. B. (2012). "Evaluation of harmonic motion elastography and acousto-optic imaging for monitoring lesion formation by high intensity focused ultrasound". PhD thesis. Boston University.

Dromi, S. et al. (2007). "Pulsed-high intensity focused ultrasound and low temperature–sensitive liposomes for enhanced targeted drug delivery and antitumor effect". In: *Clinical Cancer Research* 13.9, pp. 2722–2727.

Duck, F. A. (2002). "Nonlinear acoustics in diagnostic ultrasound". In: *Ultrasound in Medicine & Biology* 28.1, pp. 1–18. (Visited on 06/01/2012).

Ebbini, E. S., J. C. Bischof, and J. E. Coad (2001). "Lesion formation and visualization using dual-mode ultrasound phased arrays". In: *Ultrasonics Symposium, 2001 IEEE*. Vol. 2. IEEE, pp. 1351–1354.

Elder, S. A. (1959). "Cavitation microstreaming". In: *The Journal of the Acoustical Society of America* 31.1, pp. 54–64.

Erikson, K. R., F. J. Fry, and J. P. Jones (1974). "Ultrasound in medicine-a review". In: *Sonics and Ultrasonics, IEEE Transactions on* 21.3, pp. 144–170.

Errabolu, R. L. et al. (1988). "Measurement of ultrasonic nonlinear param-

eter in excised fat tissues". In: *Ultrasound in Medicine & Biology* 14.2, pp. 137–146. (Visited on 06/04/2012).

Fahey, B. J. et al. (2004). "Acoustic radiation force impulse imaging of thermally-and chemically-induced lesions in soft tissues: preliminary ex vivo results". In: *Ultrasound in medicine & biology* 30.3, pp. 321–328.

Farny, C. H. and G. T. Clement (2008). "Thermal imaging with ultrasound reflex transmission methods". In: *Ultrasonics Symposium, 2008. IUS 2008. IEEE*. IEEE, pp. 2088–2091.

Farny, C. H., R. G. Holt, and R. A. Roy (2010). "The correlation between bubble-enhanced HIFU heating and cavitation power". In: *Biomedical Engineering, IEEE Transactions on* 57.1, pp. 175–184.

Feinberg, D. A. et al. (2010). "Hybrid ultrasound MRI for improved cardiac imaging and real-time respiration control". en. In: *Magnetic Resonance in Medicine* 63.2, pp. 290–296. (Visited on 01/28/2013).

Feng, Y., J. T. Oden, and M. N. Rylander (2008). "A two-state cell damage model under hyperthermic conditions: theory and in vitro experiments". In: *Journal of biomechanical engineering* 130.4, p. 041016.

Ferrara, K., R. Pollard, and M. Borden (2007). "Ultrasound microbubble contrast agents: fundamentals and application to gene and drug delivery". In: *Biomedical Engineering* 9.

Filonenko, E. and V. Khokhlova (2001). "Effect of acoustic nonlinearity on heating of biological tissue by high-intensity focused ultrasound". In: *Acoustical Physics* 47.4, pp. 468–475.

Frizzell, L. (1988). "Threshold dosages for damage to mammalian liver by high intensity focused ultrasound". In: *Ultrasonics, Ferroelectrics and Frequency Control, IEEE Transactions on* 35.5, pp. 578 –581.

Frizzell, L. et al. (1977). "Thresholds for Focal Ultrasonic Lesions in Rabbit Kidney, Liver, and Testicle". In: *Biomedical Engineering, IEEE Transactions on* BME-24.4, pp. 393–396.

Fry, F. J. (1958). "Precision high intensity focusing ultrasonic machines for surgery". In: *American Journal of Physical Medicine & Rehabilitation* 37.3, pp. 152–156.

Fry, F. and L. Johnson (1978). "Tumor irradiation with intense ultrasound". In: *Ultrasound in medicine & biology* 4.4, pp. 337–341.

Fry, F. et al. (1970). "Threshold ultrasonic dosages for structural changes in the mammalian brain". In: *the Journal of the Acoustical Society of America* 48.6B, pp. 1413–1417.

Fry, W. J. et al. (1954). "Production of Focal Destructive Lesions in the Central Nervous System With Ultrasound*". In: *Journal of neurosurgery* 11.5, pp. 471–478.

Gelet, A et al. (1995). "Treatment of prostate cancer with transrectal focused ultrasound: early clinical experience." In: *European urology* 29.2, pp. 174–183.

Gelet, A et al. (2001). "Transrectal high intensity focused ultrasound for the treatment of localized prostate cancer: factors influencing the outcome". In: *European urology* 40.2, pp. 124–129.

Ginsberg, J., M. F. Hamilton, and D. T. Blackstock (1998). "Computational Methods". In: *Nonlinear Acoustics*. New York: Academic. Chap. 11, p. 313.

Gong, X.-F. et al. (1989). "Determination of the acoustic nonlinearity parameter in biological media using FAIS and ITD methods". eng. In: *The Journal of the Acoustical Society of America* 86.1, pp. 1–5. (Visited on 06/04/2012).

Goss, S., L. Frizzell, and F. Dunn (1979). "Ultrasonic absorption and attenuation in mammalian tissues". In: *Ultrasound in Medicine & Biology* 5.2, pp. 181–186. (Visited on 06/01/2012).

Graham, S. J., M. J. Bronskill, and R. M. Henkelman (1998). "Time and temperature dependence of MR parameters during thermal coagulation of ex vivo rabbit muscle". In: *Magnetic resonance in medicine* 39.2, pp. 198–203.

Graham, S. et al. (1999a). "Analysis of changes in MR properties of tissues after heat treatment". en. In: *Magnetic Resonance in Medicine* 42.6, pp. 1061–1071. (Visited on 12/17/2013).

Graham, S. et al. (1999b). "Quantifying tissue damage due to focused ultrasound heating observed by MRI". In: *Magnetic resonance in medicine* 41.2, pp. 321–328.

Green, P. S. and M. Arditi (1985). "Ultrasonic reflex transmission imaging". In: *Ultrasonic imaging* 7.3, pp. 201–214.

Green, P. S., J. S. Ostrem, and T. K. Whitehurst (1991). "Combined reflection and transmission ultrasound imaging". In: *Ultrasound in medicine & biology* 17.3, pp. 283–289.

Grewe, M. G. et al. (1990). "Acoustic properties of particle/polymer composites for ultrasonic transducer backing applications". In: *Ultrasonics, Ferroelectrics, and Frequency Control, IEEE Transactions on* 37.6, pp. 506–514.

Grüll, H. and S. Langereis (2012). "Hyperthermia-triggered drug delivery from temperature-sensitive liposomes using MRI-guided high intensity focused ultrasound". In: *Journal of Controlled Release* 161.2, pp. 317–327.

Gyongy, M. and C.-C. Coussios (2010). "Passive Spatial Mapping of Inertial Cavitation During HIFU Exposure". In: *Biomedical Engineering, IEEE Transactions on* 57.1, pp. 48 –56.

Gyöngy, M. and C.-C. Coussios (2010). "Passive cavitation mapping for localization and tracking of bubble dynamics". In: *The Journal of the Acoustical Society of America* 128.4, EL175–EL180.

Haar, G. ter and C. Coussios (2007a). "High intensity focused ultrasound: past, present and future". In: *International Journal of Hyperthermia* 23.2, pp. 85–87.

— (2007b). "High intensity focused ultrasound: Physical principles and devices". In: *International Journal of*

Hyperthermia 23.2, pp. 89–104. (Visited on 06/01/2012).

Haar, G. ter, D. Sinnett, and I. Rivens (1989). "High intensity focused ultrasound-a surgical technique for the treatment of discrete liver tumours". In: *Physics in medicine and biology* 34.11, p. 1743.

Haller, J. et al. (2012). "A comparative evaluation of three hydrophones and a numerical model in high intensity focused ultrasound fields". In: *The Journal of the Acoustical Society of America* 131.2, pp. 1121–1130.

Hamilton, M. F., M. C. L., and D. T. Blackstock (1998a). "Model Equations". In: *Nonlinear Acoustics*. New York: Academic. Chap. 3, p. 56.

— (1998b). "Model Equations". In: *Nonlinear Acoustics*. New York: Academic. Chap. 3, pp. 54–60.

Harris, G. et al. (2007). "P4H-1 Finite Amplitude Method for Measurement of Nonlinearity Parameter B/A Using Plane-Wave Tone Bursts". In: *IEEE Ultrasonics Symposium, 2007*, pp. 2072–2074.

Hill, C. et al. (1994). "Lesion development in focused ultrasound surgery: a general model". In: *Ultrasound in medicine & biology* 20.3, pp. 259–269.

Hinshaw, W. S. and A. H. Lent (1983). "An introduction to NMR imaging: From the Bloch equation to the imaging equation". In: *Proceedings of the IEEE* 71.3, pp. 338–350.

Hockham, N., C. C. Coussios, and M. Arora (2010). "A real-time controller for sustaining thermally relevant acoustic cavitation during ultrasound therapy". In: *Ultrasonics, Ferroelectrics and Frequency Control, IEEE Transactions on* 57.12, pp. 2685–2694.

Holt, R. G. and R. A. Roy (2001). "Measurements of bubble-enhanced heating from focused, MHz-frequency ultrasound in a tissue-mimicking material". In: *Ultrasound in medicine & biology* 27.10, pp. 1399–1412.

Hou, G. Y. et al. (2011). "Performance assessment of HIFU lesion detection by harmonic motion imaging for focused ultrasound (HMIFU): A

3-D finite-element-based framework with experimental validation". In: *Ultrasound in medicine & biology* 37.12, pp. 2013–2027.

Hynynen, K (1987). "Demonstration of enhanced temperature elevation due to nonlinear propagation of focussed ultrasound in dog's thigh< i> in vivo</i>". In: *Ultrasound in medicine & biology* 13.2, pp. 85–91.

Hynynen, K et al. (1993). "Tissue thermometry during ultrasound exposure". In: *European urology* 23 Suppl 1, pp. 12–16. (Visited on 06/01/2012).

Hynynen, K. et al. (1994). "The usefulness of a contrast agent and gradient-recalled acquisition in a steady-state imaging sequence for magnetic resonance imaging-guided noninvasive ultrasound surgery". In: *Investigative radiology* 29.10, pp. 897–903.

Hynynen, K. et al. (2005). "Local and reversible blood–brain barrier disruption by noninvasive focused ultrasound at frequencies suitable for trans-skull sonications". In: *Neuroimage* 24.1, pp. 12–20.

Ishihara, Y. et al. (1995). "A precise and fast temperature mapping using water proton chemical shift". en. In: *Magnetic Resonance in Medicine* 34.6, pp. 814–823. (Visited on 12/17/2012).

Jensen, C. R. et al. (2012). "Spatiotemporal Monitoring of High-Intensity Focused Ultrasound Therapy with Passive Acoustic Mapping". en. In: *Radiology* 262.1, pp. 252–261. (Visited on 06/01/2012).

Jensen, C., R. Cleveland, and C. Coussios (2013). "Real-time temperature estimation and monitoring of HIFU ablation through a combined modeling and passive acoustic mapping approach". In: *Physics in medicine and biology* 58.17, p. 5833.

Jing, Y., D. Shen, and G. T. Clement (2011). "Verification of the Westervelt equation for focused transducers". In: *Ultrasonics, Ferroelectrics and Frequency Control, IEEE Transactions on* 58.5, pp. 1097–1101.

Jones, R. M., M. A. O'Reilly, and K. Hynynen (2013). "Transcranial passive

acoustic mapping with hemispherical sparse arrays using CT-based skull-specific aberration corrections: a simulation study". In: *Physics in medicine and biology* 58.14, p. 4981.

Kallel, F. et al. (1999). "The feasibility of elastographic visualization of HIFU-induced thermal lesions in soft tissues". In: *Ultrasound in medicine & biology* 25.4, pp. 641–647.

Kemmerer, J. P. and M. L. Oelze (2012). "Ultrasonic Assessment of Thermal Therapy in Rat Liver". In: *Ultrasound in Medicine & Biology* 38.12, pp. 2130–2137. (Visited on 12/06/2012).

Kennedy, J. E. (2005). "High-intensity focused ultrasound in the treatment of solid tumours". en. In: *Nature Reviews Cancer* 5.4, pp. 321–327. (Visited on 06/01/2012).

Khokhlova, V. A. et al. (2006). "Effects of nonlinear propagation, cavitation, and boiling in lesion formation by high intensity focused ultrasound in a gel phantom". In: *The Journal of the Acoustical Society of America* 119.3, p. 1834. (Visited on 06/06/2012).

King, R. et al. (2003). "Preliminary results using ultrasound transmission for image-guided thermal therapy". In: *Ultrasound in Medicine & Biology* 29.2, pp. 293–299. (Visited on 09/26/2012).

Klibanov, A. L. (2006). "Microbubble contrast agents: targeted ultrasound imaging and ultrasound-assisted drug-delivery applications". In: *Investigative radiology* 41.3, pp. 354–362.

Kreider, W. et al. (2011). "The dynamics of histotripsy bubbles". In: *10th International Symposium on Therapeutic Ultrasound (ISTU 2010)*. Vol. 1359. 1. AIP Publishing, pp. 427–430.

Kumon, R. E. et al. (2012). "High-Frequency Ultrasound M-Mode Imaging for Identifying Lesion and Bubble Activity During High-Intensity Focused Ultrasound Ablation". In: *Ultrasound in Medicine & Biology* 38.4, pp. 626–641. (Visited on 06/01/2012).

Kwan, J. et al. (in press). "Ultrasound-induced inertial cavitation from gas-stabilizing nanoparticles". In: *Phsical Review Letters*.

Kyriakou, Z. et al. (2011). "HIFU-induced cavitation and heating in ex vivo porcine subcutaneous fat". In: *Ultrasound in medicine & biology* 37.4, pp. 568–579.

Lavon, I. and J. Kost (2004). "Ultrasound and transdermal drug delivery". In: *Drug discovery today* 9.15, pp. 670–676.

Law, W., L. Frizzell, and F. Dunn (1985). "Determination of the nonlinearity parameter B/A of biological media". In: *Ultrasound in Medicine & Biology* 11.2, pp. 307–318.

Lee, Y.-S. and M. F. Hamilton (1995). "Time-domain modeling of pulsed finite-amplitude sound beams". In: *The Journal of the Acoustical Society of America* 97.2, pp. 906–917.

Leighton, T (1994). "The Acoustic Bubble". In: Academic Press. Chap. 2, p. 72.

Lingeman, J. E. et al. (1986). "Extracorporeal shock wave lithotripsy: the Methodist Hospital of Indiana experience." In: *The Journal of urology* 135.6, pp. 1134–1137.

Liu, X. et al. (2008). "Noninvasive Estimation of Temperature Elevations in Biological Tissues Using Acoustic Nonlinearity Parameter Imaging". In: *Ultrasound in Medicine & Biology* 34.3, pp. 414–424. (Visited on 09/26/2012).

Lizzi, F. L. et al. (1978). "Experimental, ultrasonically induced lesions in the retina, choroid, and sclera." In: *Investigative ophthalmology & visual science* 17.4, pp. 350–360.

Lu, Y. et al. (2004). "Relationship between the temperature and the acoustic nonlinearity parameter in biological tissues". In: *Chinese Science Bulletin* 49.22, pp. 2360–2363. (Visited on 09/26/2012).

Lucas, B. G. and T. G. Muir (1982). "The field of a focusing source". In: *The Journal of the Acoustical Society of America* 72.4, pp. 1289–1296.

Lynn, J. G. et al. (1942). "A New Method for the Generation and Use of Focused Ultrasound in Experimental Biology". In: *The Journal of General Physiology* 26.2, pp. 179–193.

Maleke, C. and E. E. Konofagou (2010). "In vivo feasibility of real-time monitoring of focused ultrasound surgery (FUS) using harmonic motion imaging (HMI)". In: *Biomedical Engineering, IEEE Transactions on* 57.1, pp. 7–11.

Marczak, W. (1997). "Water as a standard in the measurements of speed of sound in liquids". In: *The Journal of the Acoustical Society of America* 102.5, pp. 2776–2779. (Visited on 03/18/2013).

Maxwell, A. et al. (2012). "Disintegration of tissue using high intensity focused ultrasound: two approaches that utilize shock waves". In: *Acoustics Today* 8.4, pp. 24–37.

McDannold, N, N Vykhodtseva, and K Hynynen (2006). "Targeted disruption of the blood–brain barrier with focused ultrasound: association with cavitation activity". In: *Physics in medicine and biology* 51.4, p. 793.

McDannold, N. J. et al. (2000). "Usefulness of MR Imaging-Derived Thermometry and Dosimetry in Determining the Threshold for Tissue Damage Induced by Thermal Surgery in Rabbits 1". In: *Radiology* 216.2, pp. 517–523.

Meaney, P. M., M. D. Cahill, and G. R. ter Haar (2000). "The intensity dependence of lesion position shift during focused ultrasound surgery". In: *Ultrasound in medicine & biology* 26.3, pp. 441–450.

Medel, R. et al. (2009). "Sonothrombolysis: an emerging modality for the management of stroke". In: *Neurosurgery* 65.5, pp. 979–993.

Mitragotri, S., D. Blankschtein, and R. Langer (1995). "Ultrasound-mediated transdermal protein delivery". In: *Science* 269.5225, pp. 850–853.

Morris, H. et al. (2008). "Investigation of the viscous heating artefact arising from the use of thermocou-

ples in a focused ultrasound field". en. In: *Physics in Medicine and Biology* 53.17, p. 4759. (Visited on 07/29/2013).

Morris, P. et al. (2009). "A Fabry–Pérot fiber-optic ultrasonic hydrophone for the simultaneous measurement of temperature and acoustic pressure". In: *The Journal of the Acoustical Society of America* 125.6, pp. 3611–3622.

Mylonopoulou, E. et al. (2010). "Exploitation of cavitation-enhanced heating for release of doxorubicin from thermosensitve liposomes by therapeutic ultrasound." In: *The Journal of the Acoustical Society of America* 128.4, pp. 2418–2418.

Nandlall, S. D., E. Jackson, and C.-C. Coussios (2011). "Real-Time Passive Acoustic Monitoring of HIFU-Induced Tissue Damage". In: *Ultrasound in Medicine & Biology* 37.6, pp. 922–934. (Visited on 08/11/2012).

Nyborg, W. L. (1981). "Heat generation by ultrasound in a relaxing medium". In: *The Journal of the Acoustical Society of America* 70.2, p. 310. (Visited on 06/01/2012).

O'Neil, H. (1949). "Theory of Focusing Radiators". In: *The Journal of the Acoustical Society of America* 21.5, pp. 516–526. (Visited on 06/01/2012).

O'Neill, D. P. et al. (2011). "A Three-State Mathematical Model of Hyperthermic Cell Death". en. In: *Annals of Biomedical Engineering* 39.1, pp. 570–579. (Visited on 12/17/2013).

Ophir, J et al. (1991). "Elastography: a quantitative method for imaging the elasticity of biological tissues". In: *Ultrasonic imaging* 13.2, pp. 111–134.

Pennes, H. H. (1948). "Analysis of Tissue and Arterial Blood Temperatures in the Resting Human Forearm". en. In: *Journal of Applied Physiology* 1.2, pp. 93–122. (Visited on 06/01/2012).

Pierce, A. D. (1989a). "Acoustics: An Introduction to Its Physical Principles and Applications". In: Acoustical Society of America. Chap. 1, pp. 14–17.

— (1989b). "Acoustics: An Introduction to Its Physical Principles and Ap-

plications". In: Acoustical Society of America. Chap. 11, pp. 566–573.

Pinton, G. et al. (2011). "Effects of nonlinear ultrasound propagation on high intensity brain therapy". In: *Medical physics* 38.3, pp. 1207–1216.

Pishchalnikov, Y. A. et al. (2003). "Cavitation bubble cluster activity in the breakage of kidney stones by lithotripter shockwaves". In: *Journal of endourology* 17.7, pp. 435–446.

Quesson, B., J. A. de Zwart, and C. T. Moonen (2000). "Magnetic resonance temperature imaging for guidance of thermotherapy". In: *Journal of Magnetic Resonance Imaging* 12.4, pp. 525–533.

Rabkin, B. A., V. Zderic, and S. Vaezy (2005). "Hyperecho in ultrasound images of HIFU therapy: Involvement of cavitation". In: *Ultrasound in Medicine & Biology* 31.7, pp. 947–956. (Visited on 06/01/2012).

Rabkin, B. A. et al. (2006). "Biological and physical mechanisms of HIFU-induced hyperecho in ultrasound images". In: *Ultrasound in Medicine & Biology* 32.11, pp. 1721–1729. (Visited on 06/01/2012).

Rahimian, S. and J. Tavakkoli (2013). "Estimating dynamic changes of tissue attenuation coefficient during high-intensity focused ultrasound treatment". en. In: *Journal of Therapeutic Ultrasound* 1.1, p. 14. (Visited on 12/18/2013).

Ribault, M et al. (1998). "Differential attenuation imaging for the characterization of high intensity focused ultrasound lesions." en. In: *Ultrasonic imaging* 20.3, p. 160. (Visited on 06/01/2012).

Rieke, V. and K. Butts Pauly (2008). "MR thermometry". en. In: *Journal of Magnetic Resonance Imaging* 27.2, pp. 376–390. (Visited on 12/06/2012).

Righetti, R. et al. (1999). "Elastographic characterization of HIFU-induced lesions in canine livers". In: *Ultrasound in Medicine & Biology* 25.7, pp. 1099–1113. (Visited on 06/01/2012).

Rivens, I. et al. (2007). "Treatment monitoring and thermometry for therapeutic focused ultrasound". In:

International Journal of Hyperthermia 23.2, pp. 121–139. (Visited on 06/01/2012).

Roberts, W. W. et al. (2006). "Pulsed cavitational ultrasound: a noninvasive technology for controlled tissue ablation (histotripsy) in the rabbit kidney". In: *The Journal of urology* 175.2, pp. 734–738.

Robinson, T. and P. Lele (1972). "An Analysis of Lesion Development in the Brain and in Plastics by High-Intensity Focused Ultrasound at Low-Megahertz Frequencies". In: *The Journal of the Acoustical Society of America* 51.4B, pp. 1333–1351.

Rouvière, O. et al. (2001). "MRI appearance of prostate following transrectal HIFU ablation of localized cancer". In: *European urology* 40.3, pp. 265–274.

Rowland, I. et al. (1997). "MRI study of hepatic tumours following high intensity focused ultrasound surgery." In: *The British journal of radiology* 70.830, pp. 144–153.

Rudenko, O. (2010). "The 40th anniversary of the Khokhlov-Zabolotskaya equation". In: *Acoustical Physics* 56.4, pp. 457–466.

Sapareto, S. A. and W. C. Dewey (1984). "Thermal dose determination in cancer therapy". In: *International Journal of Radiation Oncology*Biology*Physics* 10.6, pp. 787–800. (Visited on 06/01/2012).

Sehgal, C. et al. (1986). "Measurement and use of acoustic nonlinearity and sound speed to estimate composition of excised livers". In: *Ultrasound in Medicine & Biology* 12.11, pp. 865–874. (Visited on 06/04/2012).

Seip, R. et al. (1996). "Noninvasive real-time multipoint temperature control for ultrasound phased array treatments". In: *Ultrasonics, Ferroelectrics and Frequency Control, IEEE Transactions on* 43.6, pp. 1063–1073.

Sekihara, K., S. Matsui, and H. Kohno (1985). "A new method of measuring static field distribution using modified Fourier NMR imaging". en. In: *Journal of Physics E: Scientific In-*

struments 18.3, p. 224. (Visited on 04/09/2014).

Shi, X. et al. (1999). "Detection of high-intensity focused ultrasound liver lesions using dynamic elastometry". In: *Ultrasonic imaging* 21.2, pp. 107–126.

Silverman, R. H. et al. (2006). "Improved visualization of high-intensity focused ultrasound lesions". In: *Ultrasound in Medicine & Biology* 32.11, pp. 1743–1751. (Visited on 06/01/2012).

Simon, C., P. VanBaren, and E. S. Ebbini (1998). "Two-dimensional temperature estimation using diagnostic ultrasound". In: *Ultrasonics, Ferroelectrics and Frequency Control, IEEE Transactions on* 45.4, pp. 1088–1099.

Skovoroda, A., S. Emelianov, and M o'Donnell (1995). "Tissue elasticity reconstruction based on ultrasonic displacement and strain images". In: *Ultrasonics, Ferroelectrics, and Frequency Control, IEEE Transactions on* 42.4, pp. 747–765.

Souchon, R. et al. (2003). "Visualisation of HIFU lesions using elastography of the human prostate< i> in vivo</i>: preliminary results". In: *Ultrasound in medicine & biology* 29.7, pp. 1007–1015.

Tang, A. M. et al. (2008). "Simultaneous ultrasound and MRI system for breast biopsy: compatibility assessment and demonstration in a dual modality phantom". In: *IEEE transactions on medical imaging* 27.2, pp. 247–254.

Techavipoo, U. et al. (2012). "Temperature dependence of ultrasonic propagation speed and attenuation in excised canine liver tissue measured using transmitted and reflected pulses". eng. In: *The Journal of the Acoustical Society of America* 115.6, pp. 2859–2865. (Visited on 06/01/2012).

Thittai, A. K., B. Galaz, and J. Ophir (2011). "Visualization of HIFU-Induced Lesion Boundaries by Axial-Shear Strain Elastography: A Feasibility Study". In: *Ultrasound in*

Medicine & Biology 37.3, pp. 426–433. (Visited on 09/25/2012).

Vaezy et al. (2001a). "Image-guided acoustic therapy." In: *Annual Review of Biomedical Engineering* 3, pp. 375–390.

Vaezy, S. et al. (2001b). "Real-time visualization of high-intensity focused ultrasound treatment using ultrasound imaging". In: *Ultrasound in Medicine & Biology* 27.1, pp. 33–42. (Visited on 06/01/2012).

Vallancien, G et al. (1990). "Focussed extracorporeal pyrotherapy: experimental results." In: *European urology* 20.3, pp. 211–219.

V.P., K. (1971). "Equations of nonlinear acoustics". In: *Sov. Phys. Acoust.* 16, pp. 467–470.

Wojcik, G. et al. (1995). "Nonlinear modeling of therapeutic ultrasound". In: *, 1995 IEEE Ultrasonics Symposium, 1995. Proceedings.* Vol. 2, 1617–1622 vol.2.

Wojcik, G et al. (1997). "Pseudospectral methods for large-scale bioacoustic models". In: *Ultrasonics Symposium, 1997. Proceedings., 1997 IEEE.* Vol. 2. IEEE, pp. 1501–1506.

Wojcik, G. et al. (1998). "A study of second harmonic generation by focused medical transducer pulses". In: *Ultrasonics Symposium, 1998. Proceedings., 1998 IEEE.* Vol. 2. IEEE, pp. 1583–1588.

Wojcik, G. et al. (1999). "Nonlinear pulse calculations and data in water and a tissue mimic". In: *Ultrasonics Symposium, 1999. Proceedings. 1999 IEEE.* Vol. 2. IEEE, pp. 1521–1526.

Wojcik, G. L. et al. (1993). "Electromechanical modeling using explicit time-domain finite elements". In: *Ultrasonics Symposium, 1993. Proceedings., IEEE 1993.* IEEE, pp. 1107–1112.

Wu, F. et al. (2003). "A randomised clinical trial of high-intensity focused ultrasound ablation for the treatment of patients with localised breast cancer". en. In: *British Journal of Cancer* 89.12, pp. 2227–2233. (Visited on 06/01/2012).

Wu, J. and G. Du (1990). "Temperature elevation generated by a focused Gaussian beam of ultrasound". In: *Ultrasound in medicine & biology* 16.5, pp. 489–498.

Wu, T. et al. (2001). "Assessment of thermal tissue ablation with MR elastography". en. In: *Magnetic Resonance in Medicine* 45.1, pp. 80–87. (Visited on 06/01/2012).

Xu, Z. et al. (2007). "Effects of acoustic parameters on bubble cloud dynamics in ultrasound tissue erosion (histotripsy)". In: *The Journal of the Acoustical Society of America* 122.1, pp. 229–236.

Zabolotskaya, E. and R. Khokhlov (1969). "Quasi-plane waves in the nonlinear acoustics of confined beams". In: *Sov. Phys. Acoust* 15.1, pp. 35–40.

Zderic, V. et al. (2004). "Attenuation of porcine tissues in vivo after high-intensity ultrasound treatment". In: *Ultrasound in Medicine & Biology* 30.1, pp. 61–66. (Visited on 06/01/2012).

Zhang, S. et al. (2009). "Dynamic changes of integrated backscatter, attenuation coefficient and bubble activities during high-intensity focused ultrasound (HIFU) treatment". In: *Ultrasound in medicine & biology* 35.11, pp. 1828–1844. (Visited on 10/04/2012).

Zhu, S. et al. (2002). "The role of stress waves and cavitation in stone comminution in shock wave lithotripsy". In: *Ultrasound in medicine & biology* 28.5, pp. 661–671.